Microscopic Model For Spin, Orbital And Charge Ordering In Transition Metal Compounds

Thesis Submitted for the Degree of

Doctor of Philosophy (Science)

in

Physics (Theoretical)

by

SHISHIR KUMAR PANDEY

Department of Physics

University of Calcutta

2017

Acknowledgements

I have spent nearly six years as a Ph.D. student at S. N. Bose Centre (SNB) and this journey could not have been so enjoyable without continuous guidance, support, help and mentorship from many individuals. Though words are not enough to express my gratitude to all those who have helped me in their own way, I would like to take this opportunity to express my sincere thanks to all of them specially to my critics. First and foremost, I would like to extend my heartiest gratitude to my supervisor Prof. Priya Mahadevan for her continuous mentoring, supervision and guidance throughout the period of my Ph.D. I have learn many things from her and her valuable suggestions and help lead to successful completion of my Ph.D. thesis. The knowledge and exposures which I have gained while working with her will surely help me to grow in my research career. Thank you also for all the snacks and chocolates you brought from all your visits which were no less than life supports for all of us in the group.

I really enjoyed working in our research group and for that, I would like to first thank my super seniors Bipul da, Ashis da, Abhinav bhaiya, Kapil bhaiya, Hirak da and my immediate seniors Saikat da and Ruma di for making me feel homely in the early days of my Ph.D. Special thanks for all those big treats I got from you people. I would also like to thank Basudeb (my partner in crime) with whom I share many pleasant and unpleasant memories during my stay in Kolkata. The current group members, Sagar, Poonam, Joydeep and Sumanti, must also be thanked for all their support. A special thanks to Poonam for her invaluable support in the last days of my Ph.D. I got many new ideas while presenting my works during the group-talks which have helped me to enrich my clarity and conceptualize the overall thought process towards the topics I have worked on.

Apart from our group, I have had privilege to be in the company of Jena da, Sandeep bhaiya, Sandeep da, Arka da and Rajiv da. I would also like to thank Dilip, Kartik, Dhani ji, Ransell, Sarowar da, Sudhanshu, Saurav, Ravindra, Ankan, Neeraj, Avinash, Balwant, Debabrata and Atul. Thanks to all of them for creating such joyful and homelike environment which was beyond any expectations. I would like to acknowledge the computing facilities, PMG, ATHENA, UNAST, CRAY and PHOTON which I have extensively used here at the S. N. Bose center. I would also like to thank Abhijit Ghosh da (computer center) for all his technical support.

Apart from SNB friends, I would also like to thank my ISM friends Biswajit, Siddharth and my school friend Gyan Prakash for their consistent support in all these years. I would also like to sincerely thank my graduation days friends Sanjeev and Manu bhaiya for withstanding me after all these times. I am very much thankful to Vikas bhaiya, Ram Lal bhaiya and Rajarshi bhaiya for all their support and advices at various stages of my research carrier.

Last but not the least I would like to convey my uttermost respect and gratitude to all my family members and a special thanks to my parents for being so patient with me. I must thank my sister and late grandfather for all their support in many different forms.

Shishir Kumar Pandey
Kolkata, India
September, 2017

List of Publications

1. **Route to high Néel temperatures in $4d$ and $5d$ transition metal oxides**,
S. Middey, Ashis Kumar Nandy, S. K. Pandey, Priya Mahadevan and D. D. Sarma,
Phys. Rev. B **86**, 104406 (2012).

2. **Driving force for martensitic transformation in $Ni_2Mn_{1+x}Sn_{1-x}$**,
Soumyadipta Pal, Sagar Sarkar, S. K. Pandey, Chhayabrita Maji and Priya Mahadevan,
Phys. Rev. B **94**, 115143 (2016).

3. **The driving force for charge ordering in rare earth nickelates**,
Basudeb Mandal, Sagar Sarkar, S. K. Pandey, Priya Mahadevan, Cesare Franchini, A. J. Millis and D. D. Sarma,
arxiv:1701.06819v1 .

4. **Layer dependent electronic structure changes in transition metal dichalcogenides –The role of geometric confinement**,
Ruma Das*, S. K. Pandey*, and Priya Mahadevan,
arxiv:1702.04535v1 .

5. **Doping an antiferromagnetic insulator: A route to an antiferromagnetic metallic phase**,
S. K. Pandey, Priya Mahadevan and D. D. Sarma,
Euro. Phys. Lett. **117**, 57003 (2017).

6. **Absence of insulator to metal transition at higher band fillings: A model Hamiltonian study**,
S. K. Pandey and Priya Mahadevan,,
Manuscript in preparation.

7. **Microscopic origin of room temperature magnetism in double perovskites**,
S. K. Pandey, A. K. Nandy, Poonam Kumari and Priya Mahadevan,
Manuscript in preparation.

8. **Cr doping in Rutile VO_2: A first principle study**,
A. Kumar*, S. K. Pandey*, S. Sarkar and Priya Mahadevan,
Manuscript in preparation.

Contents

List of Figures

List of Tables

Chapter 1

Inroduction

The mineral lodestone, a natural magnetic oxide of iron (magnetite Fe_3O_4) was known to Greeks which had the ability to attract iron [2] and was mentioned in Thales of Miletus (ca. 624–548 B.C.) [1]. Repulsive action of magnetism was also know to the Romans but it was only in the period A.D. 1000–1200 that its use in compass and navigation [3] was realized by Shen Kua (1030–1093), a Chinese mathematician and instrument maker, according to G. Sarton. As the time passed, people got more curious about magnetic materials and now these are being used in our day to day life.

Response to an applied magnetic field by these materials is the most fundamental property known as magnetism. There are two sources of magnetism. In the First one, magnetic field is produced by moving electric charges. The development of this theory started from the establishment of the inverse square law by Charles Augustin Coulomb in 1785 to the discovery that an electric current would affect a magnetic needle by Hans Christian Oersted (1820) followed by André Marie Ampère's study in 1825 proving mathematically and experimentally that a current in a circuit is equivalent to a "magnetic shell" of certain strength via the contributions from Simon Denis Poisson (1781–1840). It was then further improved by Wilhelm Weber in 1852 and followed by James Clerk Maxwell (1831–79) [4,5]. In the second one, magnetism emerges from the discovery of a fully quantum mechanical phenomenon, the electron spin, an idea proposed by George Uhlenbeck and Samuel Goudsmit in 1925 [6–9]. This was an effort to eliminate the drawbacks of Bohr-Sommerfeld quantum theory of elliptical orbits. They proposed that an electron must be

treated as a charged sphere spinning around its own axis, having an intrinsic angular momentum and so an intrinsic magnetic dipole moment. Over the years this quantum theory of magnetism was further developed by W. Heisenberg, J. H. Van Vleck, E. C. Stoner, H. Bethe, F. Blöch, J. C. Slater and others.

Pauli exclusion principle [9,10], which specifies that electrons, in the orbits of an atom which are specified by orbital, magnetic and spin quantum numbers , cannot occupy the same quantum state. This when combined with the Hund's rule [11] of filling of shells, result in unpaired electrons in an atom therefore causing a net magnetic moment. In complex materials [12–14] the magnetic phenomena are the consequences of various interactions present in that material. To discuss these in details we first start with the discussion on magnetism in atoms and ions in the next section, followed by discussion on the various aspects of magnetism in materials.

1.1 Origin of The Atomic Moment

From the Bohr's picture of stationary orbits, the magnetic moment of an electron of charge e^- moving around an atomic nucleus is due to, a) orbital motion of the electron with angular momentum $\mathbf{l}$ for which the magnetic moment is given by,

$$\mu_l = -\mu_B \mathbf{l} \tag{1.1}$$

b) intrinsic magnetic moment [15] of an electron associated with its spin $\mathbf{s}$ is given by,

$$\mu_s = -g\mu_B \mathbf{s} \tag{1.2}$$

where $\mu_B = \frac{eh}{4\pi mc}$ is known as Bohr magneton and g is called the Landé g-factor whose value is equal to 2. Here $\mathbf{s}$ can have the values $\pm$ 1/2. The scenario is different in case of many electrons present in an atom which interact with each other. Considering Pauli exclusion principle in such cases, the many electron wavefunction which is the product of the spatial and spin wavefunctions aquire the antisymmetric nature either in the spatial or in the spin part of the wavefunction. Physical ideas about taking such interaction between the electrons are the basic ideas behind the Hund's rules. First rule is total $\mathbf{S}$ should be maximum so that the Coulomb energy is minimum

because of the Pauli exclusion principle which prevents electrons with parallel spins being in the same place. After satisfying the first rule, in the second rule, the total **L** should be maximum for the valence electrons of a given atom. This is to minimize energy when the electrons with the orbital motion in the same direction can more effectively avoid each other hence reducing the Coulomb repulsion. These rules gives rise to the multiplet terms associated to the atoms or ions with more than one electron. In the third Hund's rule, the final value of **J**, the total angular momentum of the system is found using **J** = |**L** - **S**| when the cell is less than half filled and **J** = |**L** + **S**| when it is more than half filled. This rule is an attempt to reduce the spin-orbit interaction energy and is applicable only in specific conditions as of the case of rare earth ions. In many cases, for example in transition metal ions, dominance of the crystal field contribution break this third rule.

We should note here that these three Hund's rule predict the ground state of a given system but provide no information about the exited states and so one can only estimate the magnetic moment of an atom or ion considering the ground state provided by these set of rules. Diamagnetism and paramagnetism are the main manifestation of atomic magnetism.

1.1.1 Diamagnetism

All materials are diamagnetic upto some extent. Diamagnetism has the atomic origin of magnetic moments and usually occurs in the atom with a symmetrical electronic structure and no permanent magnetic moment *i.e.* no unpaired electron. In such substances, a magnetic field induces a magnetic moment which opposes the applied magnetic field. The diamagnetic susceptibility is negative and usually independent of temperature. The magnetization in this case (at T = 0 K) can be given as

$$M = -\frac{Ne^2B}{6m_eV}\sum_{i=1}^{Z}\langle r_i^2\rangle \tag{1.3}$$

where N is no. of ions with mass m_e and Z electrons in volume V with all filled shells. B is the applied magnetic field.

1.1.2 Paramagnetism

Atomic moments in a paramagnetic material also has the atomic origin and paramagnetism is in general has much stronger effects than diamagnetism. Paramagnetic materials have positive susceptibility such that the induced magnetic moment by an applied magnetic field align parallel with the field. In the atoms which do have unpaired electrons, in the absence of the applied magnetic field, the magnetic moments interacts very weakly and have random orientations. The applied magnetic field try to align them up and the magnetization in this case depends upon the strength of applied field. An increase of temperature will try to randomize the spins and so the magnetization has the B/T dependency. Within the quantum mechanical treatment, the magnetization is given by,

$$M = M_s \tanh\left(\frac{\mu_B B}{k_B T}\right) \tag{1.4}$$

Here M_s is the saturation magnetization and is defined as the maximum value of magnetization when all the magnetic moments are aligned. k_B and T are the Boltzmann constant and the temperature at which the magnetization M is measured.

1.2 Magnetism In Solids

Magnetism in solids are distinguished from the atomic magnetism by two important experimental features. First, in atoms, the total angular momentum (orbital and spin) produces the net magnetic moment while in solids it is found that only the spin part of total angular momentum is contributing to magnetic moments because of the quenching of orbital angular momentum, as in transition metals, by the crystal field produced by anions [16, 17]. Second, materials in which angular momentum is quenched, magnetic moments coming from the spin part should be 2, 3 and 4 μ_B for Ni, Co and Fe. In the bulk, the experimentally observed value are 0.616, 1.715 and 2.216 for Ni, Co and Fe respectively which is attributed to the itinerant nature of electrons in a solid. [18].

In solids, various arrangement of magnetic moments on the neighboring atoms lead to different types of magnetic ordering. This magnetic ordering mostly occur in the presence of external magnetic field and vanishes as soon as this external field is removed. If this magnetic ordering in the material retained even after removal of the external magnetic field, then they are called permanent magnets. Some examples like Fe, Co and Ni are previously mentioned. Magnetism, an inherently quantum mechanical effect, is the consequence of the interplay between the electron-electron Coulomb interaction (electron-electron correlation), hopping interaction between the electrons (exchange interaction) and Pauli exclusion principle. We will discuss each of these interactions and their effects on the magnetic behavior of materials in the coming sections.

1.2.1 Exchange Interaction

The importance of the exchange interactions in long range magnetic ordering can be understood with a simple example. In the case of magnetic dipolar interaction, we know that the dipole-dipole interaction energy between two magnetic dipoles μ_1 and μ_2 separated by $\mathbf{r}$ is given by,

$$E_{dip} = \frac{\mu_0}{4\pi r^3}\left[\boldsymbol{\mu_1}\cdot\boldsymbol{\mu_2} - \frac{3}{r^2}(\boldsymbol{\mu_1}\cdot\mathbf{r})(\boldsymbol{\mu_2}\cdot\mathbf{r})\right] \tag{1.5}$$

For each moments $\approx 1\ \mu_B$ with separation r ≈ 1 Å, E_{dip} is of the order of 10^{-23} J equivalent to 1 K in temperature. But the ordering temperature of 1023 K for materials like $SrTcO_3$ [19] provide us the clue about a different origin of the magnetic order other than magnetostatic dipolar interaction in such materials.

If we consider a simple two electron picture, exchange interaction expressed in terms of exchange integral (J) arises because of the energy difference between the singlet (E_S) and triplet state (E_T). Assuming the normalized spin parts of the wavefunction, the exchange integral for this two electron system can be written as,

$$J = \frac{E_S - E_T}{2} = \int \psi_a^*(\mathbf{r}_1)\psi_b^*(\mathbf{r}_2)\hat{H}\psi_a(\mathbf{r}_2)\psi_b(\mathbf{r}_1)d\mathbf{r}_1 d\mathbf{r}_2 \tag{1.6}$$

where $\mathbf{r}_1$ and $\mathbf{r}_2$ are the spacial coordinates of the two electrons. This exchange integral is positive when two electrons are on the same atom which stabilizes the triplet state and hence

antisymmetric spacial state, minimizing the Coulomb repulsion between them by placing them apart. If two electrons are on two different atoms, a bond formation allows them to hop around both atoms lowering their energy by saving the kinetic energy. Thus spatially symmetric bonding and specially antisymmetric antibonding molecular orbitals will be formed. Since antibonding orbitals are higher in energy, this favors singlet states and so exchange integral is likely to be negative in this case. The interatomic exchange interaction is main driving mechanism behind magnetism [20, 21]. The most important exchange mechanisms are described in the coming sections.

1.2.2 Direct Exchange

When the electrons on the magnetic atoms interact via an exchange interaction directly, *i.e.* without any intermediary atom, then it is known as direct exchange. This exchange interaction requires sufficient direct overlap between the magnetic orbitals taking part in it and so it is a short range coupling which decreases sharply with the separation between the magnetic atoms. Direct exchange can be well understood from the Fig 1.1. When the atoms are very close, the electrons spend most of their time in between the atoms due to the presence of inter atomic hopping. Since their spacial position is same at the same time, Pauli's exclusion principle force them to have opposite spins and so negative exchange causing energy cost of Coulomb repulsion U. Since gain from the hopping of electrons on the neighboring sites have the dominant contribution to the energetics, this type of antiparallel alignment of spin is favored by direct exchange.

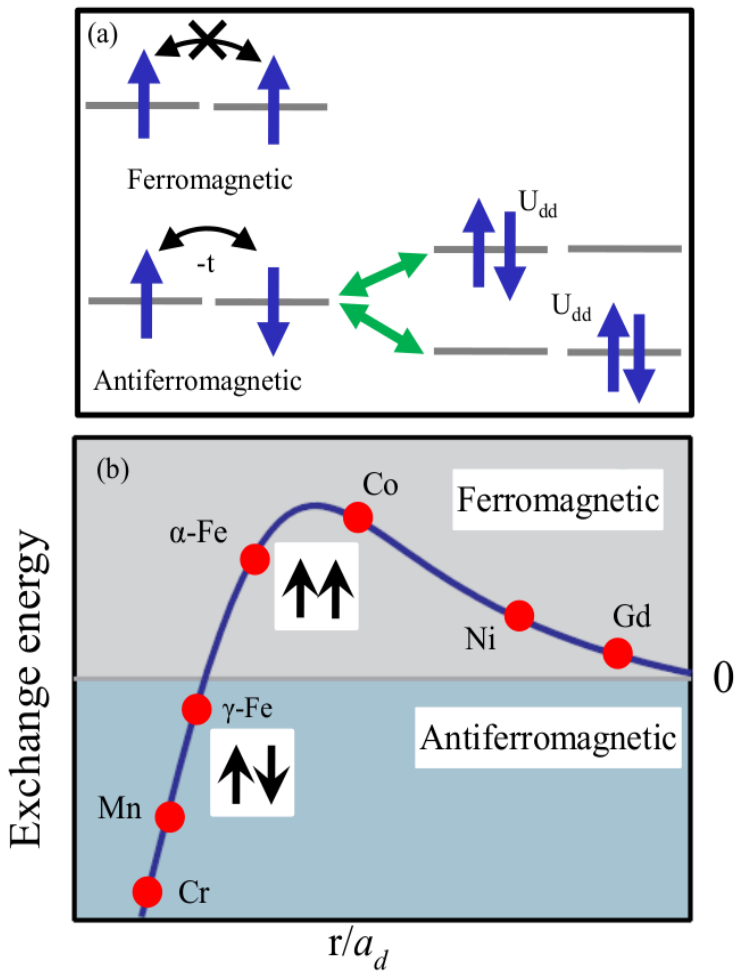

Figure 1.1: A simple picture of direct exchange, (a), favors the antiparallel alignment of the spins (lower) as it allows the electrons to hop to the neighboring site and costs an energy of U_{dd} . While, in the parallel alignment of the spins (upper) hopping is suppressed by the Pauli exclusion principle. The Bethe-Slater curve (taken from Ref. [22]) in (b) yields that elements above the horizontal axis are ferromagnetic, below that axis are antiferromagnetic

If the atoms are far apart, the gain from hopping t reduces significantly due to small orbital overlap ($U_{dd} > t$). In order to minimize the electron-electron repulsion, a parallel alignment of spins occurs and so a positive exchange. Balance between the Coulomb and kinetic energies (hopping interaction) decides the sign of direct exchange J. Since a real situation like in rare earths, $4f$ electrons are highly localized and tightly bound to the nucleus, the direct exchange is expected to be very weak. In $3d$ transition metals like Fe, Co and Ni where orbital extension is higher when compared to $4f$, it is still difficult to realize the role of direct exchange on

the magnetic behavior of these metals and there is a clear necessity of some indirect exchange mechanism to take account of both the localized and itinerant character of electrons.

1.2.3 Indirect Exchange : Superexchange

The previous idea of kinetic exchange [23] was extended by Anderson [24] to situations where the magnetic ions are separated by large non-magnetic anions and so direct hopping between the orbitals is highly unlikely. This is the case of a number of ionic solids like oxides and fluorides which have magnetic ground state. Anderson explained the large ordering temperatures of many such compounds with enhanced kinetic exchange also called superexchange, due to covalent mixing of cation and anion orbitals. As the anions as well as the cations are involved in superexchange, it is a second order process and is derived from second order perturbation theory. To understand the mechanism of superexchange, consider a simple case of two transition metal ions having magnetic moments due to single unpaired electron in d orbital separated by an oxygen ion having two p electrons in the valence shell (see Fig 1.2). As shown in Fig 1.2, antiferromagnetic coupling in the singlet state has two hopping processes which are possible in two different ways, hence delocalizing these electrons over the whole system, thus lowering the total energy of the system via kinetic energy gain. As discussed previously, this antiferromagnetic exchange constant is nothing but the energy difference between the singlet and triplet state and is given by,

$$J_{AFM} = \frac{4t_{pd}^4}{(U_{dd} + \Delta_{pd})^2} \left(\frac{1}{U_{dd}} + \frac{1}{U_{dd} + \Delta_{pd}} \right) \tag{1.7}$$

where U_{dd} is the Coulomb repulsion between two d electrons, t_{pd} is the hopping between electrons in d and p orbitals and $\Delta_{pd} = \epsilon_d - \epsilon_p$ is the charge transfer energy. The first term in above expression is due to the hopping process involving only a single doubly occupied d-orbital while the second term is due to hopping process involving two doubly occupied d-orbitals.

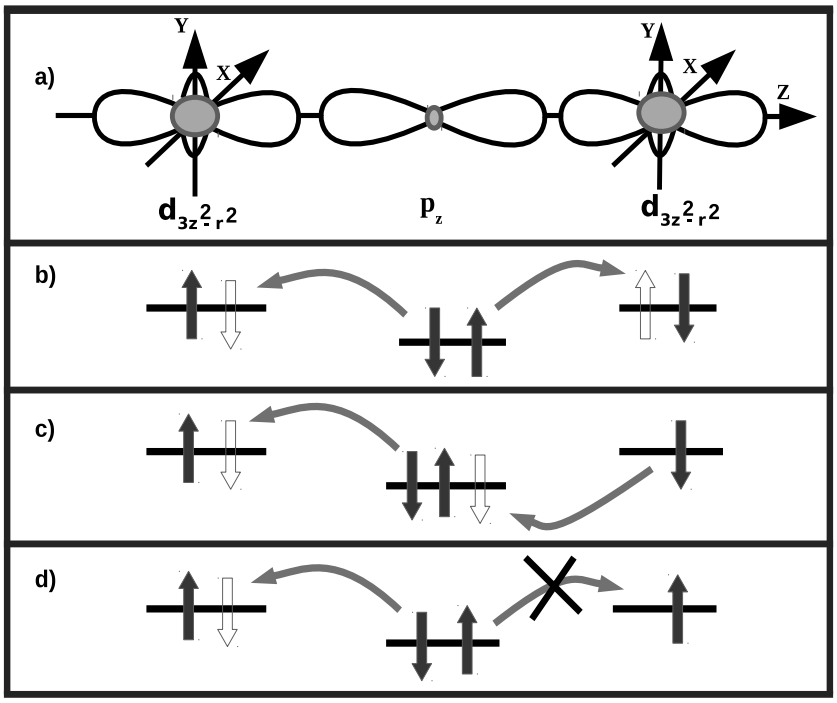

Figure 1.2: A simple picture of superexchange where the orbital on the central site is different from the orbitals on the sides. Typically, two d orbitals are coupled via an intermediate oxygen p orbital as in 2(a). For antiparallel alignment of the spins on two d orbitals, (b) and (c) describe the two ways that two consecutive hopping processes are possible, while in (d) for ferromagnetic case, the Pauli principle forbids the second hopping process.

The superexchange strongly depend upon the angle between the cation-anion-cation bond. In Fig. 1.2, we have considered the bond angle to be 180°. If this bond angle is 90°, a reverse superexchange mechanism gets operative favoring ferromagnetism when the orbitals on cations (say $d_{3x^2-r^2}$ and $d_{3y^2-r^2}$) connected via different orbitals on anion (say p_x and p_y) as shown in Fig 1.3a.

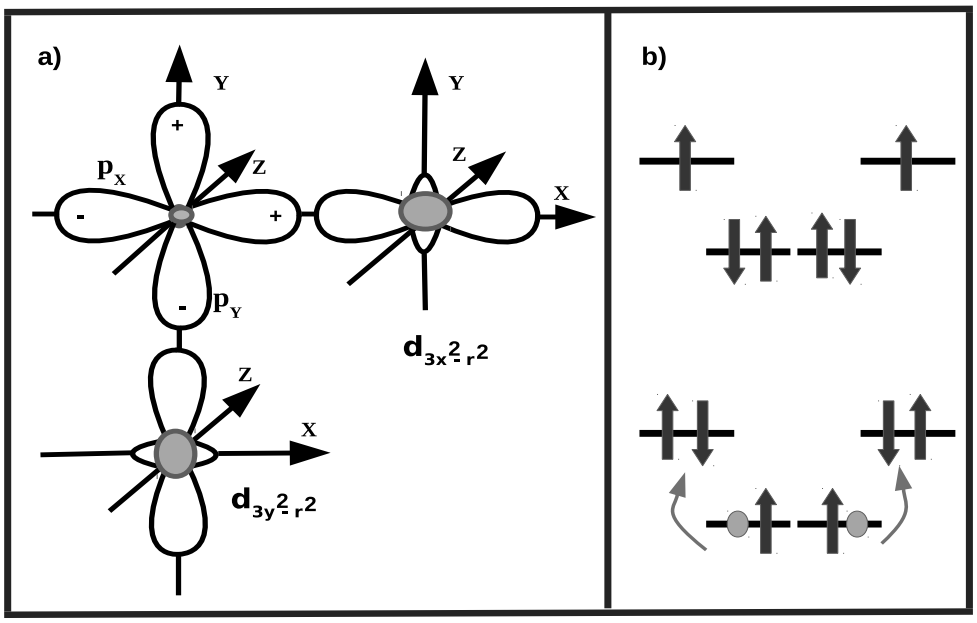

Figure 1.3: In a 90° arrangement of *d*-*p*-*d* group as in (a), one finds that the d orbitals are coupled to the orthogonal p orbitals and hence, it becomes impossible for an electron on one d orbital to reach the d orbital on the other site. Therefore, the ferromagnetic super-exchange in (b) is mediated via the Coulomb exchange on the connecting oxygen.

Because of the involvement of two p orbitals, hopping is non-linear in this case, and the symmetry restrictions allow only a one way hopping resulting in weak ferromagnetic coupling between the cations. This process is shown shown schematically in Fig 1.3b. Because of the two hole on the anion orbitals shown in Fig 1.3b, formation of triplet state on oxygen will lower the energy by $2J_p$. So, superexchange is mediated via the Coulomb exchange on the connecting cation and is ferromagnetic in nature. The exchange constant in this case is given by,

$$J_{FM} = \frac{4t_{pd}^4}{(U_{dd} + \Delta_{pd})^2} \left(\frac{2J_p}{4(U_{dd} + \Delta_{pd})^2 - J_p^2} \right) \tag{1.8}$$

It is significantly weaker than the antiferromagnetic superexchange. This is the situation with the e_g orbitals involved in the exchange interaction. However, situation might vary with involvement of the t_{2g} orbitals in exchange. In this case, if the t_{2g} orbitals are pointing towards each other between the oxygens atoms, the $d - d$ direct hopping interactions play crucial role in making

antiferromagnetic superexchange operative between the d electrons. This is however might be the case for the lighter transition metals as in the case of heavier ones, the $d-p-d$ hopping again becomes more relevant. In a situation where both the hopping pathways (direct $d-d$ and through oxygens) are available, the total exchange will depend upon the signs of t_{dd} and t_{dp}. Similar sign of both the hopping will enhance the total exchange while opposite sign of these two will partially cancel out, hence reducing the total exchange interaction in the system.

Structural distortions in real materials cause a deviation of cation-anion-cation bond angle and in many case these angles are neither 90° nor 180°. This results in competition between the antiferromagnetic and ferromagnetic superexchange in such materials. The superexchange interactions are usually explained in terms of a set of semi-empirical rules, called Goodenough-Kanamori-Anderson rules [11, 25, 26] which are briefly given as,

1) When orbitals on both the cations are either half-filled or empty then the superexchange will lead to antiferromagnetism shown in Fig 1.4a and 1.4b respectively.

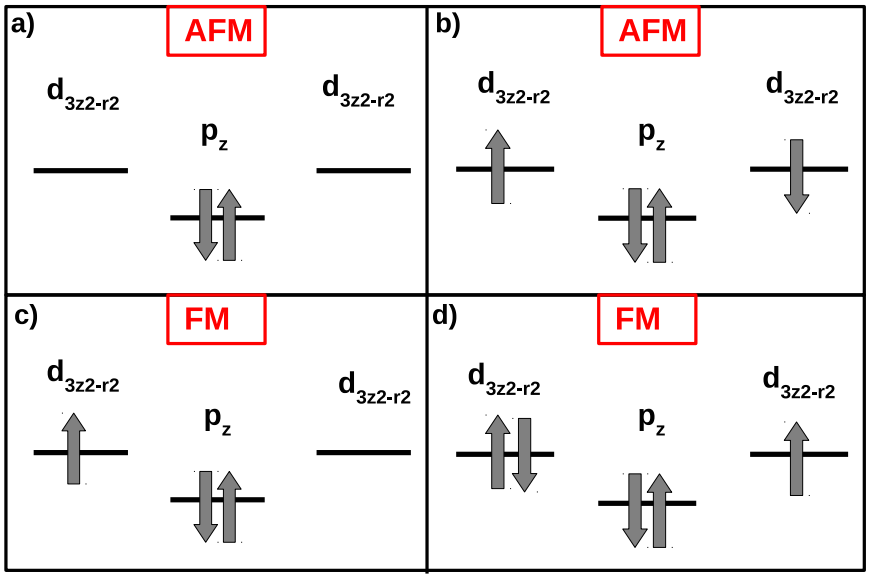

Figure 1.4: The Goodenough-Kanamori-Anderson rules: In a 180° geometry of $d-p-d$ group, (a) and (b) yield the antiferromagnetic alignment of spins on d orbitals, while in (c) and (d) the favored alignments are ferromagnetic.

2) When a) orbital on one cation is empty and on other cation it is half filled or b) one is half filled and other is fully filled, then the superexchange will be ferromagnetic in nature shown in Fig 1.4c and 1.4d respectively.

1.2.4 Itinerant Exchange

In metallic systems, the exchange mechanism might be entirely different and it can be mediated by the conduction electrons. When the conduction electrons get spin-polarized by a localized magnetic moment of a magnetic ion, this polarization then couples to a magnetic moment on a neighboring atom at a distance r giving rise to an indirect exchange interaction known as itinerant exchange or RKKY interaction. The name RKKY stands for Ruderman, Kittel, Kasuya and Yosida, the discoverers of this interaction [27–29]. For a large value of, the exchange constant has the form,

$$J_{RKKY}(r) \propto \frac{\cos(2k_F r)}{r^3} \tag{1.9}$$

where k_F is the radius of spherical Fermi surface. This long range oscillatory interaction, depending upon the separation between the magnetic atom can be either ferromagnetic or antiferromagnetic in nature.

1.2.5 Double Exchange

Occurrence of a ferromagnetic exchange interaction due to mixed valency (more than one oxidation state) shown by the magnetic ions present in the system is known as double exchange. It can also be understood as the case when both, the kinetic exchange and Coulomb exchange, work simultaneously and was proposed by Zener in 1951 [30]. Since average electron per cation is non-integral and some sites have more number of electrons than others dut to mixed valency of magnetic ions [31], electrons can hop between such sites without any cost of U in such systems. Consider the example of $LaMnO_3$ which contains Mn^{3+} ions has A-type antiferromagnetic ground state. After 17.5% doping of Sr atoms, the systems becomes ferromagnetic with ordering temperature around room temperature below which it becomes metallic. Since Sr is divalent (Sr^{+2}), La is trivalent (La^{+3}) and oxygen has valency of -2, in $La_{1-x}Sr_xMnO_3$, it is clear that a fraction x of Mn ions are Mn^{4+} and rest $1-x$ are Mn^{3+}. The ferromagnetic ordering in this

doped material [32, 33] is due to double exchange which can be best understood by the Fig 1.5. The e_g elctron from the Mn^{3+} can hop to neighboring Mn site if the e_g orbital of the same spin is available which is the actual case of Mn^{4+} sites. But the intra atomic exchange interaction between the t_{2g} and e_g electrons would like to keep them all aligned in the same direction in order to lower the energy because of the first Hund's rule.

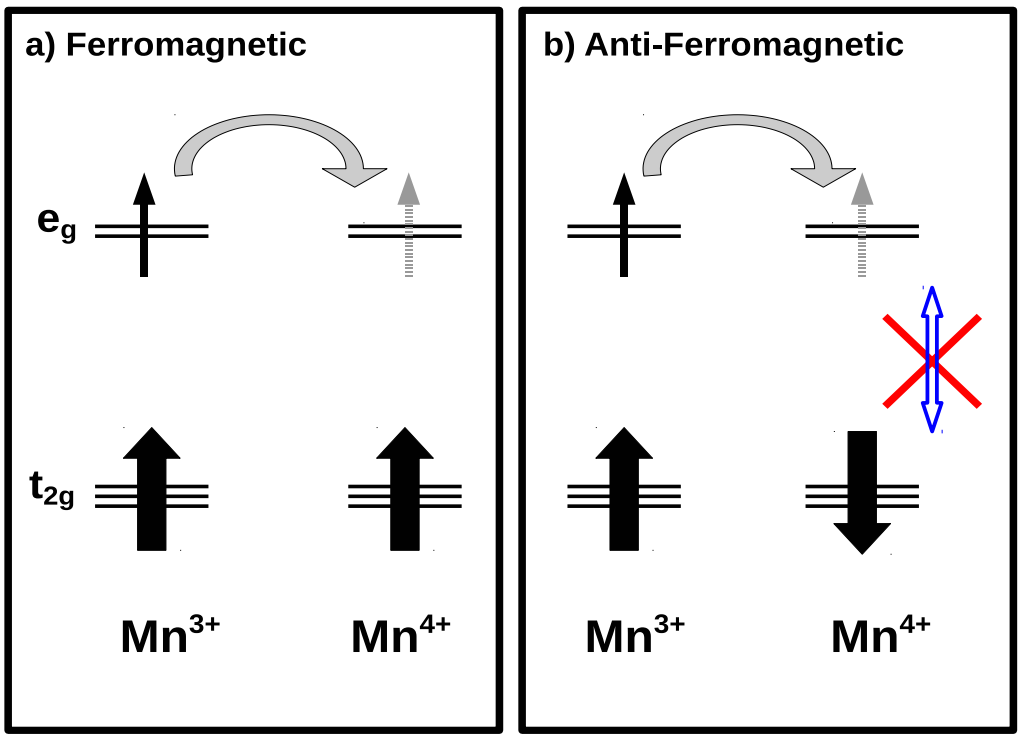

Figure 1.5: The double-exchange mechanism in hole doped manganite perovskite. Coupling between the localized spins on Mn^{3+} and Mn^{4+} ions and the itinerant electrons in a) ferromagnetic alignment, (b) antiferromagnetic alignment of localized spin. The ferromagnetic alignment of the localized spins stabilized through Hund's exchange coupling.

Thus ferromagnetic arrangement of neighboring ions is necessary to maintain the condition of high spin arrangement. Since hopping results in kinetic energy reduction, it lowers the overall energy of the system. As in this ferromagnetic ordering, the e_g electron can hop through out the crystal, the system becomes metallic. Suppression of the double exchange mechanism may occur in the presence of orthogonal arrangement of the oxygen dumbbells [34].

1.3 Electron-Electron Correlation

The insulating state of many systems like NiO [35], which would have been metallic in the conventional one electron band picture are explained by considering electron-electron interaction between the magnetic atoms. This interaction is called electron-electron correlation. We know that expectation value of a product of two quantities of an interacting system has not the same value as the product of their individual expectation values. This is due to the effect of correlation. For example in a system, when a particle at position $\mathbf{r}_1$ with density $\rho(\mathbf{r_1})$ will interacts with a particle at position $\mathbf{r}_2$ with density $\rho(\mathbf{r_2})$, then average of product of these densities $\langle\rho(\mathbf{r_1})\rho(\mathbf{r_2})\rangle$ cannot be factorize to the product of individual averages which is $\langle\rho(\mathbf{r_1})\rangle\langle\rho(\mathbf{r_2})\rangle$. This establishes the fact that correlation effect is beyond the factorization approximation as considered in Hartree or Hartree-Fock theories.

The electron being a quantum particle exhibits both wave and particle like characteristics. According to Blöch theorem [36], electron behavior in a periodic lattice can be approximated as an extended plane wave. With increase in the number of electrons in a solid, their is no more free motion of electrons and the mutual electron-electron interaction becomes more significant. In such correlated electron system, for example, d electrons in transition metal compounds experience two competing forces : Coulombic repulsion which try to localize electrons individually at the atomic sites (dominating particle-like behavior) while hybridization with oxygen p electronic states which try to delocalize electrons (dominating wave-like behavior). The balance between two makes these correlated materials excellent resources for studying various electronic properties [37–39].

In a solid, the correlated electrons with a well defined dispersion ϵ_k, corresponds to the band width (W) which is the result of hopping interactions between the electrons. If τ is the average time spent by electrons on an atom then $\tau \propto 1/W$ implies that narrow bands lead to the longer time that an electron resides on an atom thereby, feels the presence of other electrons. The correlation between electrons enhances due to the formation of the narrow bands making them "strongly correlated" materials. There are various examples among the transition metals and their oxides such as V, Cr, Fe or rare-earth metals such as Ce where electrons occupy narrow bands. The profound effects of correlation on electronic and magnetic properties of materials can

be understood with a simple example of Nickel Oxide (NiO). The local density approximation within density functional theory (DFT) predicts a nonmagnetic metallic ground state while local spin density approximation (LSDA) gives a small gap, hence describing NiO as a Slater insulator [40,41]. Both the band gap and the magnetic moment are poorly underestimated in this case when compared to the experimentally measured values of 4.1 eV [42] and 1.7 μ_B respectively. Experimentally, it is also found to be an antiferromagnetic Mott insulator. Thus to get the correct band gap and moment, the vital role of strong electronic correlation in such material is evident which will bring this system close to the Mott regime [43]. Electron correlations are also known to be essential for phenomenon like magnetism and high temperature superconductivity [44]. In fact, at low temperatures, the interplay between the spin, charge and orbital as well as lattice degrees of freedom of the correlated d and f electrons leads to variety of unusual phenomena.

1.3.1 The Hubbard Model

Consider a simple case of hydrogen atoms separated by distance a, having non-degenerate $1s$ level at each site. The tight binding Hamiltonian for this system considers the hopping of electrons from site to site and is given by,

$$H = -t \sum_{<ij>,\sigma} c^{\dagger}_{i\sigma} c_{j\sigma} + H.C. \tag{1.10}$$

where $c^{\dagger}_{i\sigma}(c_{j\sigma})$ creates (annihilates) electrons at site i (j) with spin σ and t is the hopping matrix element, and sum is over the nearest neighbors. For N-lattice sites system, there will be N energy levels in this band and according to Pauli principle 2N places available for electrons in this band. Thus the exact half filling of bands implies the system should be metallic. This conclusion is independent of matrix element t which determines the total bandwidth W = 2nt where n is the number of nearest neighbors which means that such systems will always be metallic for any distance between the sites and for arbitrarily small value of t. This unphysical result is the consequence of the ignored important physical effect of Coulomb repulsion between the electrons in the one-electron Hamiltonian. Now, within the same picture, when electron from site i will hop to site j which already had an electron would cost the additional energy of Coulomb

repulsion between two electrons at site j and is denoted by U. A schematic picture representing the various process involved in this model is shown in Fig 1.6. So the new Hamiltonian will take the form,

$$H = -t \sum_{<ij>,\sigma} c^{\dagger}_{i\sigma} c_{j\sigma} + U \sum_{i} n_{i\uparrow} n_{i\downarrow} + H.C. \tag{1.11}$$

where $n_{i\sigma} = c^{\dagger}_{i\sigma} c_{i\sigma}$ is the number operator with σ either up or down. This is known as Hubbard model [45]. When $t \gg U$, this model reduces to the previously explained tight-binding model and the electrons are delocalized over the whole crystal.

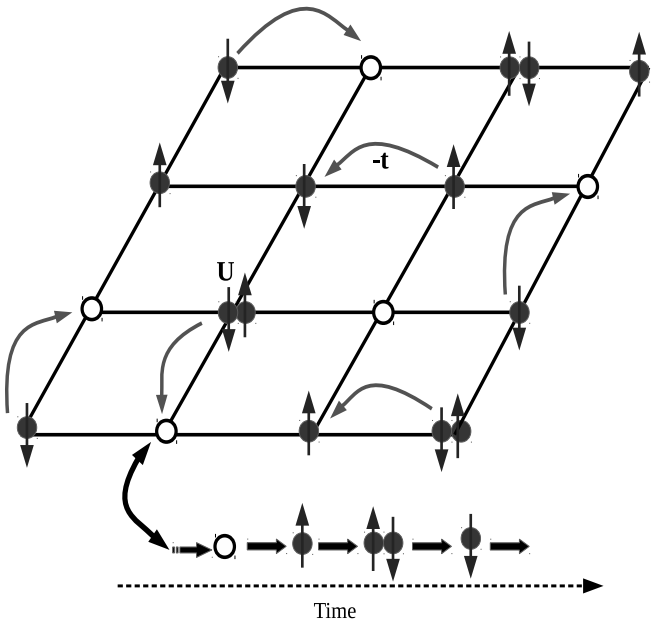

Figure 1.6: Schematic illustration of interacting electrons in a square lattice in terms of the Hubbard model. In this lattice, electrons, which have a negative charge (-), mass and a spin ($\uparrow$ or $\downarrow$), move from one site to another site with a hopping amplitude t. Therefore, the quantum dynamics leads to fluctuations in the occupation of any lattice site (i) with time, indicated by the time sequence. A lattice site may thus either be doubly occupied with $\uparrow$ and $\downarrow$ both spins, singly occupied with $\uparrow$ or $\downarrow$ spin or unoccupied. A doubly occupied site costs an interaction energy U.

For $U \gg t$, the energy band which was previously half filled for non-interacting case would split into two subbands separated by an energy gap $E_g \sim U$-W ($=U$-2nt) with the lower band occupied and the upper one empty. These bands are called lower and upper Hubbard bands. Materials described by this insulating mechanism are called Mott or Mott-Hubbard insulators. Depending on the interplay between t, U and the filling n, whether a system is insulating or metallic is illustrated by Fig 1.7.

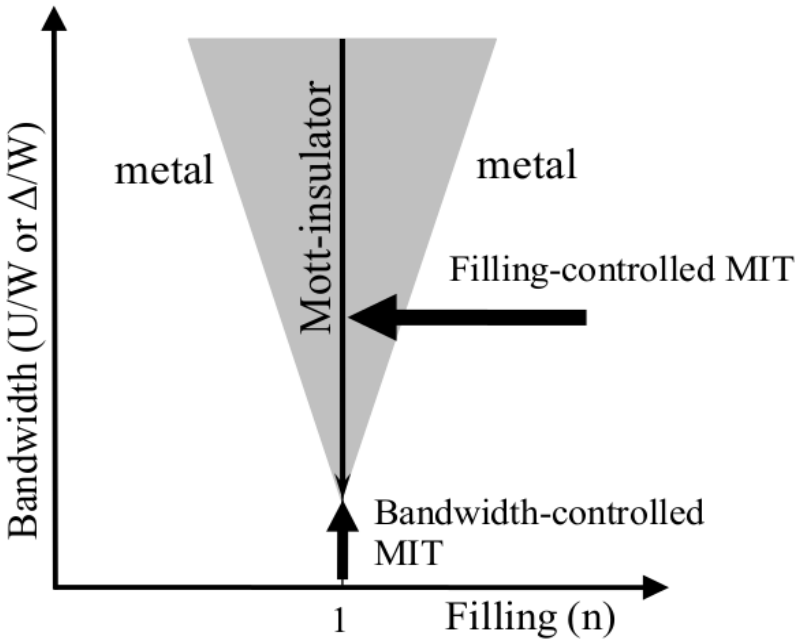

Figure 1.7: The schematic metal-insulator phase diagram within the Hubbard model in the electron correlation strength (U/W or Δ/W) and band filling (n) plane. There are two routes for the metal-insulator transition (MIT), which are shown as the bandwidth-controlled MIT and the filling-controlled MIT. This figure is redrawn from Ref [46]

In an antiparallel arrangement of spins, the virtual hopping process of an electron from one site to another and back lowers the energy of the system, so the energy gain is proportional to t^2, while cost for the double occupancy of a site in the intermediate state is U. Hence the energy gain in this process would be $\propto$ -t^2/U. The magnetic state of such systems may also be described by effective Heisenberg Hamiltonian which is a spin only Hamiltonian and is given as,

$$H_{eff} = J \sum_{ij} \mathbf{S}_i \cdot \mathbf{S}_j, \qquad J = \frac{2t^2}{U} \tag{1.12}$$

where $\mathbf{S}_{i/j}$ are the spin operators at sites i/j and J is exchange interaction strength discussed in the previous sections.

1.4 Effect Of Different Environments In A Crystal

The spherical symmetry of an isolated atom or ion is violated when in a crystal and the resulting symmetry is determined by the local symmetry of the crystal structure. Since atomic orbitals have angular dependencies (except s orbitals which are spherically symmetric) and so, in the local environment of the crystals which are often not spherically symmetric, different orbitals behave differently. This results in rich and complex electronic properties in the case of correlated materials.

1.4.1 Crystal Field Splitting

The electric field derived from orbitals on the neighboring atoms which are treated as negative point charges is called crystal field [47]. In the case of a transition metal ion, energies of d orbitals increases due to Coulomb repulsion when the negative point charges approach the metal ion. In a crystal, the electrostatic field produced by surrounding negative charges are never spherically distributed and so the five d orbitals in a transition metal atom will be affected differently in the presence of these negative charges which were otherwise degenerate in energy. The magnitude and nature of crystal field effect highly depend on the local symmetry in the crystal. In many transition metal compounds, metal ions sit at the center of octahedron formed by anions such as oxygen. The d_{xy}, d_{yz}, d_{xz} orbitals have the lobes pointing between x,y and z axes feel less Coulomb repulsion of the anionic point charges than the $d_{z^2-r^2}$ and $d_{x^2-y^2}$ orbitals whose lobes point along the z-axis and x,y-axes respectively. A schematic representation of it is given in Fig. 1.8.

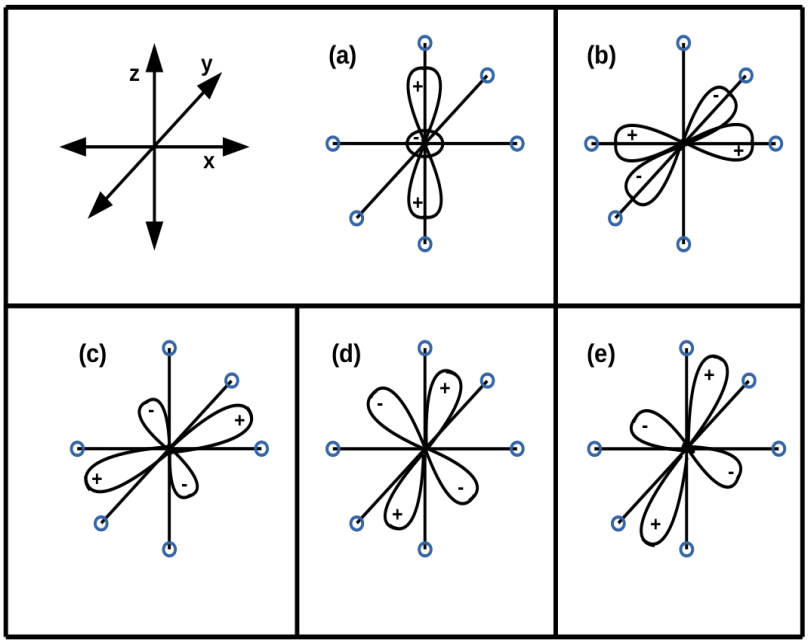

Figure 1.8: Schematic representation of electron densities for five different d orbitals in a transition metal atom in an octahedral environment. The two e_g orbitals, (a) d_{z^2} and (b) $d_{x^2-y^2}$ have spatial spread along the axes while the three t_{2g} orbitals, (c) d_{xy}, (d) d_{xz} and (e) d_{yz} have their special spread between the axes.

This split the transition metal d orbitals into two sets, triply degenerate (d_{xy}, d_{yz}, d_{xz}) t_{2g} orbitals which are lower in energy and doubly degenerate ($d_{z^2-r^2}$ and $d_{x^2-y^2}$) e_g orbitals higher in energy. In a tetrahedral geometry, this trend of splitting is reversed with e_g orbitals lower in energy than the t_{2g} orbitals. The other geometries like square-planar and linear have the level ordering d_{xy}, $d_{x^2-y^2}$; d_{xz}, d_{yz}; $d_{z^2-r^2}$ and d_{xz}, d_{yz} ; $d_{z^2-r^2}$;d_{xy}; $d_{x^2-y^2}$, respectively in the order of increasing energy. The splitting of energy levels in various environments of crystal field is shown in Fig 1.9.

In real materials, the point charge model yields unsatisfactory results for the crystal-field splitting suggesting corrections beyond the point-charge approximation. An improvement on the approximation of crystal field theory (CFT) with consideration of the overlap between the d orbitals on the transition metal ion with orbitals on surrounding legands (ions) is known as legand field theory.

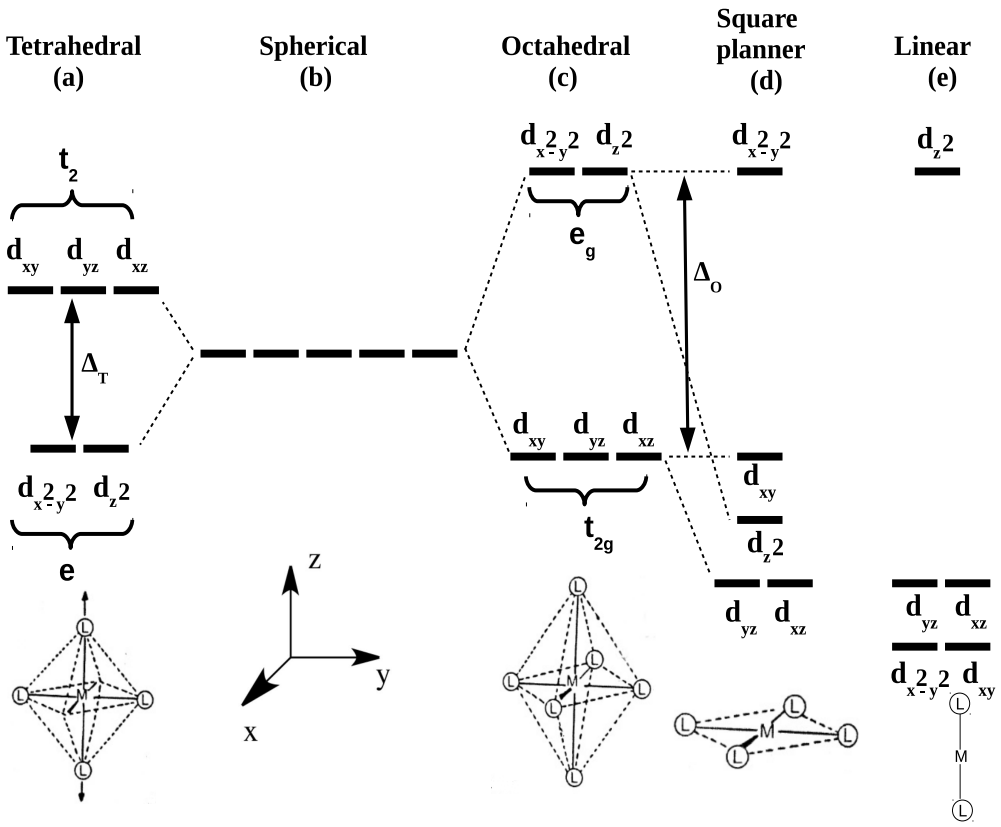

Figure 1.9: Schematic representation of the splitting of d orbitals under various crystal field symmetries such as (a), for tetrahedral, (b), for spherical, (c), for octahedral, (d), for square planar and (e), for linear symmetries respectively.

When d electrons surrounded in an octahedron of negative ions (ligands), the crystal field splitting which is denoted by Δ_{CF} (or 10Dq [48]), has the energy of $E_{t_{2g}} = -\frac{2}{5} = -4Dq$ and of $E_{e_g} = +\frac{3}{5} = +6Dq$. Precise filling of the orbitals in the case of a transition metal ion depends upon competition among crystal field energy, Hund's exchange coupling (J_h) and the energy cost due to Coulomb repulsion because of the double occupancy of an orbital.

In the large U ($> \Delta_{CF}$) limit as in the case of $3d$ transition metal oxides, the competition between Hund's exchange coupling and the crystal field can give rise to a high spin (HS) state in case when $J_h > \Delta_{CF}$ and low spin (LS) state in case of $\Delta_{CF} > J_h$. If $\Delta_{CF} < J_h$ i.e. in the weak crystal field limit, each t_{2g} and e_g orbital will be singly occupied first and after that double occupancy of orbitals will take place hence system have a high spin configuration. On other hand when $\Delta_{CF} > J_h$, double occupancy of lower t_{2g} orbitals occurs first, then only electron

will occupy the higher e_g orbitals. For example, in the case of a trivalent Co ion, if $J_h > \Delta_{CF}$, then six valence electrons in the $3d$ orbitals will give rise to a high spin $t_{2g}^4\ e_g^2$ state by obeying the Hund's rule. On the other hand, if $\Delta_{CF} > J_h$, then the ground state will be a low spin state with $t_{2g}^6\ e_g^0$ configuration. The intermediate spin state $t_{2g}^5\ e_g^1$ is energetically unstable and the system gets stable after the lowering the symmetry by Jahn-Teller distortions discussed in the next section [51, 52].

When one moves from $3d$ to $4d$ to $5d$ transition metals oxides, the values of U and J_h decreases while Δ_{CF} increases. These conditions mostly lead to a low spin state as for example in the case of $SrRuO_3$ [53], Ru is in +4 oxidation state with a low spin (S=1) configuration as the larger spatial extension of Ru $4d$ orbitals is responsible for a larger Δ_{CF}.

1.4.2 Jahn-Teller Theory

Hermann Arthur Jahn and Edward Teller have given this theory [54] which states that degeneracy makes the symmetric configuration unstable, gives rise to a strong coupling between electron and phonon resulting in a structural distortion which lift the degeneracy by lowering the symmetry of the crystal and thereby lowering its energy. Jahn-Teller distortion can be simply understood by considering the example of octahedral systems, where it further introduces a splitting in levels of t_{2g} and e_g symmetry. Cubic perovskite $LaMnO_3$ [49, 50] is an example of Jahn-Teller Material where double degenerate e_g orbitals with an electron in it (Mn^{+3}-$3d^4$: t_{2g}^3, e_g^1) needs to lower its symmetry via structural distortion. Another example of a strong Jahn-Teller active material is $KCuF_3$ [55].

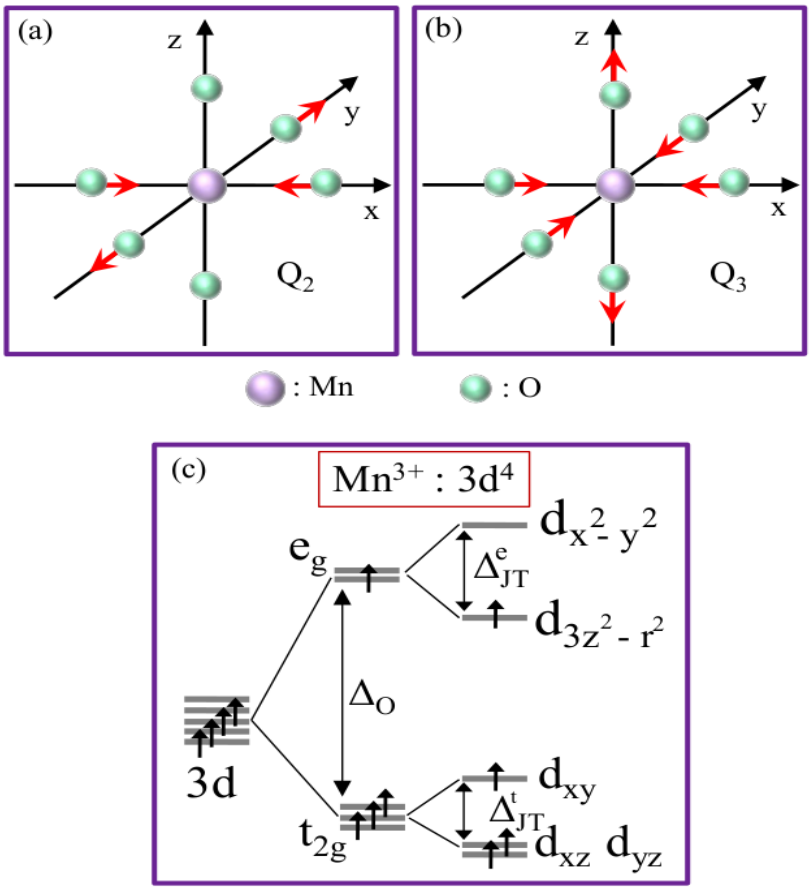

Figure 1.10: (a) and (b), schematically represent the vibrational modes, Q_2 and Q_3, respectively for a perovskite, $LaMnO_3$, while (c) describes the resultant Jahn-Teller splitting in the t_{2g} and e_g manifolds due to tetragonal Q_3 mode.

There are two types of structural distortion which are represented by two vibrational modes, orthorhombic Q_2 mode and tetragonal Q_3 mode as shown in Fig 1.10. Lowering of structural symmetry by these modes result in degeneracy lifting of the highest occupied e_g orbitals. For the experimentally observed Jahn-Teller distortion, the Q_3 mode is dominant over the Q_2 mode as it brings more stabilization in the energy of the $d_{z^2-r^2}$ orbital than the $d_{x^2-y^2}$. Although the same phenomena is true for the systems having electronically degenerate t_{2g} orbitals, in this case its effect is relatively weaker due to weak π bond formation by the triply degenerate t_{2g} orbitals. $LaTiO_3$ [56] and $LaVO_3$ [57] are the examples of weak Jahn-Teller active materials.

The Jahn-Teller distortions are differ by two points for t_{2g} and e_g case. First is that, unlike in the e_g case, degeneracy lifting of t_{2g} orbitals also occurs due to trigonal distortions as shown in Fig. 1.11.

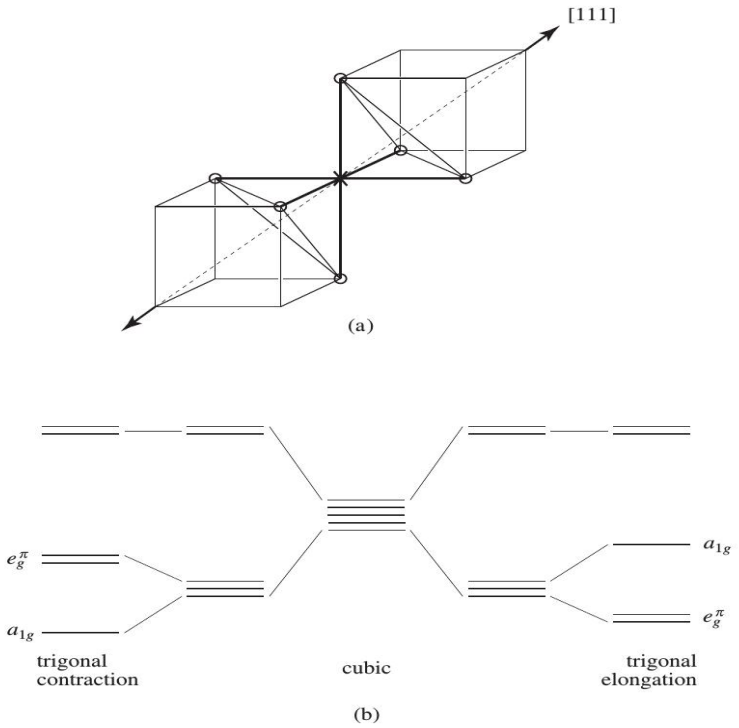

Figure 1.11: Splitting of d orbitals in the trigonal distortion is shown. (a) Trigonal distortion in a perovskite lattice. (b) Contraction and elongation give rise to degeneracy lifting of t_{2g} orbitals forming singlet a_{1g} and doublet e_g^π. Figure is taken from Ref. [58]

In this case, splitting of t_{2g} levels into a singlet a_{1g} and a doublet e_g^π occurs, both having the character of all the planner orbitals. Second point is, Jahn-Teller distortions in this can lead to both, the elongation and compression of MO_6 octahedra in the Q_3 mode. This depends upon the number of electrons in the partially filled t_{2g} orbitals. For 2 or 7-d electrons, it would be energetically favorable to occupy the lowest doublet state with 2 or 4 electrons which leads to elongation c/a > 1. If there are 1 or 6-d electrons, lowest singlet would be occupied first and so the compression of MO_6 octahedra can lead to a compression c/a < 1. This is schematically represented in Fig. 1.12.

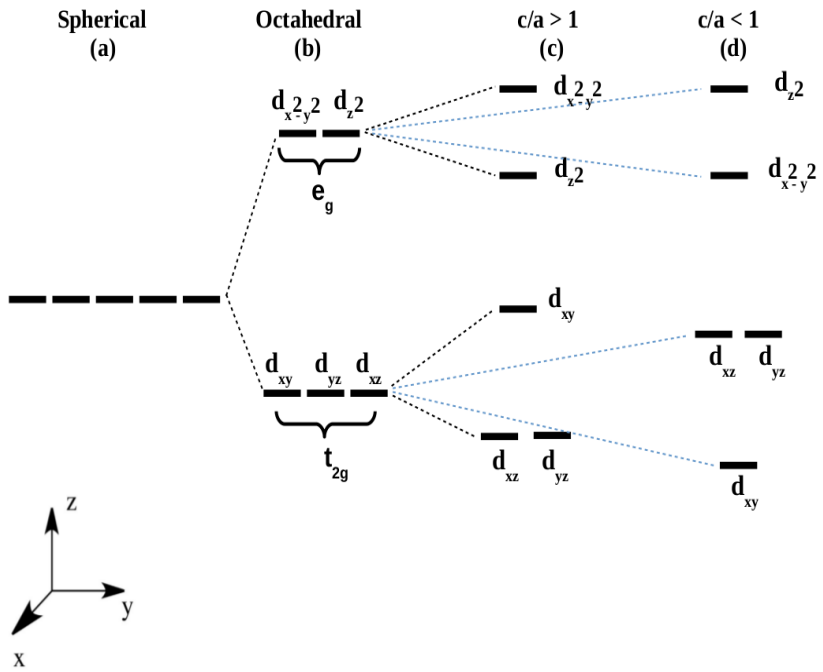

Figure 1.12: (a) and (b) represent d orbitals in spherically symmetric and in octahedral environment of anions respectively. Depending upon the number of electrons in t_{2g} orbitals, splitting of t_{2g} and e_g orbitals (c) in an elongated (c/a $>$ 1) MO_6 octahedra and (d) in a compressed (c/a $<$ 1) MO_6 octahedra.

1.5 The Case Of Doped Correlated Systems

When dealing with transition metal compounds, involvement of spin, charge and lattice degree of freedom and their interplay give rise to several interesting phenomena. For example, alteration of the magnetic properties of a system, appearance of charge ordering, metal to insulator transitions, high-temperature superconductivity etc can occur in strongly correlated systems with the change in electron concentration. Considering the example of doping a Mott insulator by electrons or hole, for example $La_{1-x}Ca_xMnO_3$. with the average Mn valency of Mn^{3+x}, one can explore the properties of a system which has non-integer electron concentration with partially filled bands. Also, in a transition metal oxide where overlapping of localized d levels with less correlated broader d bands one can have a metallic state with correlations still playing

an important role. To understand the above mentioned aspects, properties of doped transition metal oxides at various limits of the band filling is discussed in the next section.

1.5.1 Magnetism at different filling in Hubbard Model

Considering non degenerate Hubbard Hamiltonian given by equation 1.11 at exact half electron filling i.e. for n=1, we know that for $U \gg$ t, it is a Mott insulator with antiferromagnetic ground state (discussed previously). With decrease U/t at n=1, one expects an insulator to metal transition (Mott transition), however in certain cases with the special property called nesting of fermi surface [59], metallic state is found to be unstable, and occurrence of charge density wave (CDW) or spin-density wave (SDW) opens a gap at the fermi energy making the system insulating even in the presence of a weak interaction.

For $n\neq$1 i.e. deviation of electron density from one electron per site, the situation is even more complicated as the strong Coulomb repulsion $U/t \gg 1$ with antiferromagnetic background of the undoped case is still present. This antiferromagnetic ordering of the background spins prevent the motion of the extra electron due to spin on the neighboring sites (Pauli exclusion principle). Thus the antiferromagnetic background appears to hinder the motion of the extra electron and so the gain from the kinetic energy is very less in this case. Now in a ferromagnetic background of spins, the extra doped electron or hole will be able to move unobtrusively and the gain from kinetic energy would be $\sim$ W $\sim$ zt. So for $U \gg$ t, we lose the exchange energy by $\sim \frac{t^2 V_f}{U}$ (where V_f is ferromagnetic volume of the system) but we gain by the doped electron's kinetic energy $\sim t\delta$ (where δ is the doping concentration), when we make the system ferromagnetic instead of antiferromagnetic. In $U = \infty$ limit, it was shown by Nagaoka [60, 61] that even the slightest doping of electron or hole in the system can destroy the antiferromagnetism making it ferromagnetic. For large but finite U and finite concentrations of holes (δ= 1-n), the phase diagram produced by numerical calculations is given in Fig. 1.13

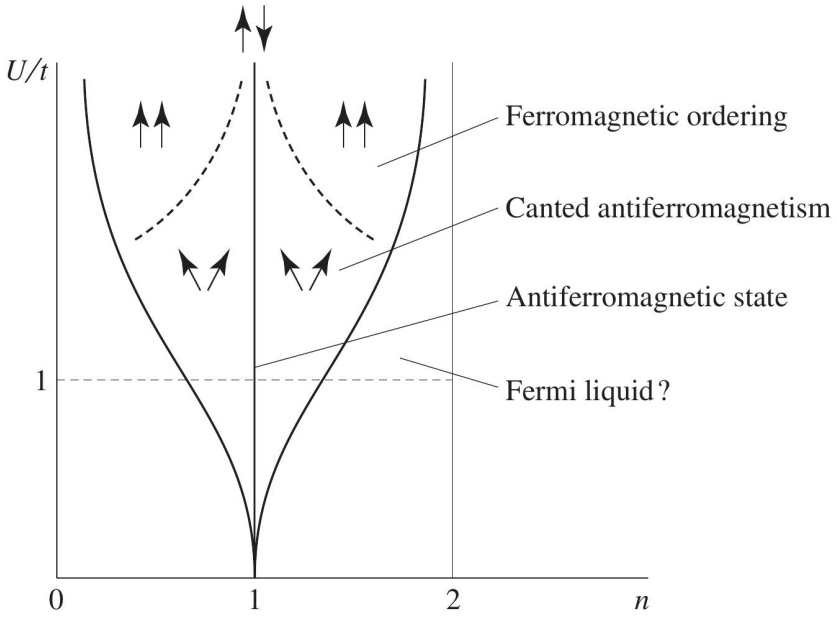

Figure 1.13: Phase diagram obtained for Hubbard model with arbitrary filling of bands and for different interaction strengths U/t. This figure is taken from the reference [62, 63]

.

In the presence of the strong correlations, doping region where the transition from AFM state to FM state takes place have possibility of stabilizing different intermediate states for example canting of spins, spiral magnetic order etc. The critical situation for this transition from AFM to FM state is approximately given by 0.25 $\delta_c = t/U$. The non degenerate Hubbard model for bipartite lattices, there is an electron-hole symmetry. However in cases where further nearest neighbor hopping or the orbital degeneracy is considered, this symmetry might break and the solution to Hubbard model at the same electron and hole doping might be different [64].

1.5.2 Charge Ordering

A typical examples of Charge ordering (CO) in the transition metal compounds are the systems doped with electron or holes as in the example of $La_{1-x}Ca_xMnO_3$. At x=0, Mn ions are in a homogeneous +3 state and with the increase in doping concentration different valence states of Mn appear may causing charge ordering at low temperatures. In the case of half-doped systems i.e. where two different valence states have equal half concentrations, one has checker-

board pattern of charge ordering in the basal plane. For example, in half doped manganites $La_{0.5}Ca_{0.5}MnO_3$ (LCMO) [33] and $La_{0.5}Sr_{1.5}MnO_4$ (LSMO) [65], Mn^{3+} and Mn^{4+} have equal concentration, ordered in a checkerboard pattern. A phase diagram for $La_{1-x}Ca_xMnO_3$ is given in Fig. 1.14. The first guess about appearance of such pattern of CO might be attributed to phenomena of minimization of Coulomb repulsion in the system by placing this two different valence sites as far as possible from each other but then these valence states should order in the similar pattern along the third direction as well which is not the case. So, other interactions such as electron-phonon coupling are believed to play an important role in stabilizing the charge ordered state in such systems.

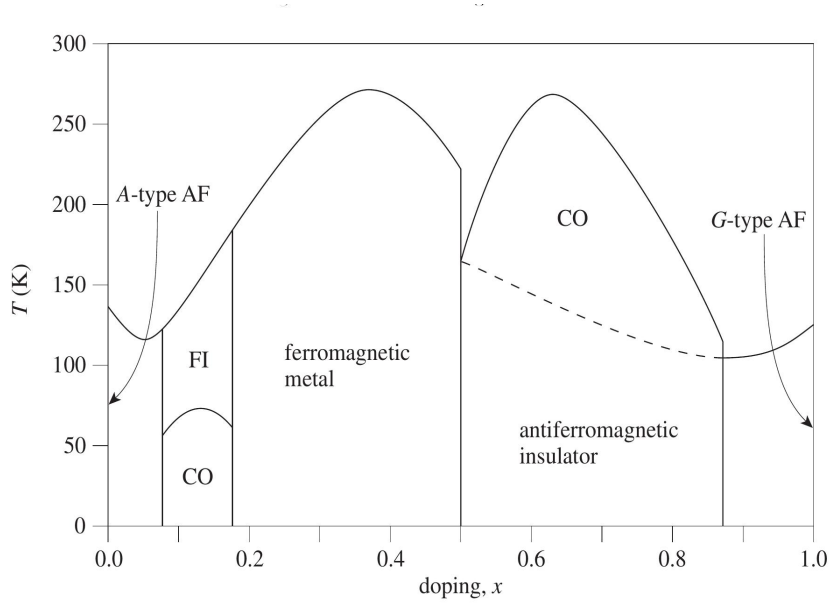

Figure 1.14: Charge ordered phases present in both low and high hole doping limits in $La_{1-x}Ca_xMnO_3$. This figure is taken from the Ref. [67]

In actual case, difference in the charge of different ions is usually less than 1 when compared to their usual valences of +3 and +4 and in the CO state the actual valency was believed to be 3.5±0.2. However, a first principle study in Ref. [66] on $La_{0.5}Sr_{1.5}MnO_4$ found that although, this system has two different types of Mn atoms namely Mn^{+3} and Mn^{4+} with very different environment formed by oxygen atoms, the net charge associated with them is very similar. They concluded that the charge ordered state in this system can be understood in terms of the modification of Mn-4*p* density of states at charge ordered lattice site.

In another quantum mechanical explanation is that it is the quantum numbers of these states which coincides with their typical valency of 3+ and 4+. A negligibly small charge difference of the different transition metal (TM) sites are also attributed to the strong TM d and oxygen p hybridization in these systems and the small charge transfer energy causes the leak of charges from TM sites to oxygens and so not much change in the charges on Mn sites but Mn-O states have the total quantum numbers of either Mn^{3+} or Mn^{4+}.

The case of charge ordering away from the half filling can be understood by considering the phase diagram of $Pr_{1-x}Ca_xMnO_3$ (PCMO) [68–70] given in Fig. 1.15. Here, one can find that PCMO remains in the charge ordered state in the doping range of 0.3 to 0.5 with the checkerboard pattern of the ordering. LCMO in this range is metallic as the holes are delocalized in nature but PCMO remain insulating all over the region and the reason behind it is still debatable.

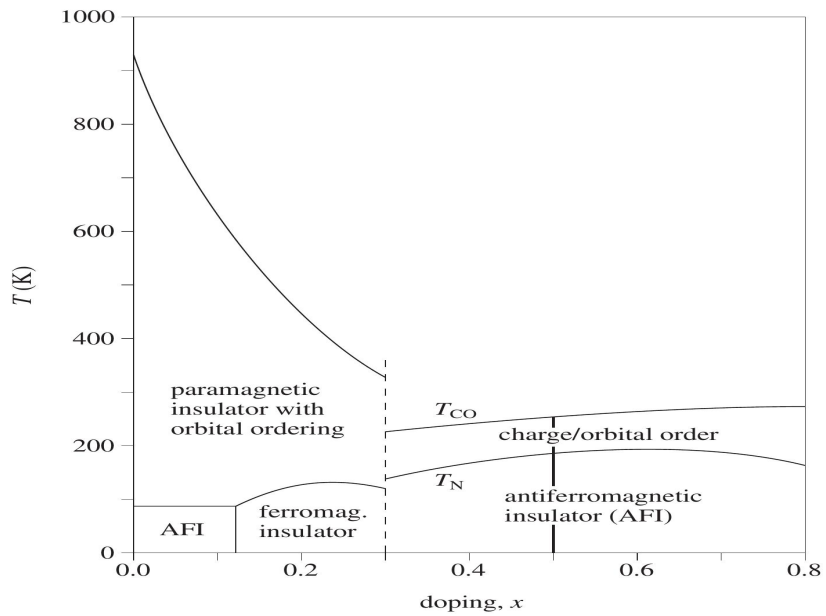

Figure 1.15: Charge ordered phases away from the half filling in a large range of doping concentrations above a certain critical temperature in $Pr_{1-x}Ca_xMnO_3$. This figure is taken from the Ref. [69].

One important fact to notice here is that there is no electron-hole symmetry in the above mentioned cases of doped manganites and the appearance of this asymmetry is mostly attributed to the orbital degree of freedom available in such systems but the topic is not well settled [64].

1.5.3 Orbital Ordering

The systems with doubly degenerate e_g orbitals e.g. Cr^{2+} , Mn^{3+} (t_{2g}^4 e_g^1) or with partially filled triply degenerate t_{2g} orbitals in a symmetric crystal field environment are found to have orbitally ordered ground state. In such systems, structural phase transitions are highly probable which lift this orbital degeneracy leading to occupancy of specific orbitals, making the system orbitally ordered. $LaVO_3$ [72] and $LaMnO_3$ [71]are examples of undoped systems with orbitally ordered ground state. With doping, in the case of half doped maganites, for example $La_{0.5}Ca_{0.5}MnO_3$, Mn exists in +3 and +4 valence states. Mn^{3+} has the doubly degenerate e_g orbitals with one electron in it. The Jahn-Teller distortion lifts the degeneracy of the e_g orbitals and favors the occupancy of either $d_{3z^2-r^2}$ or $d_{x^2-y^2}$. This ordering phenomenon is always accompanied by the structural distortions. Electron density on an ion becomes anisotropic (like elongated in particular direction) after orbital ordering takes place. Orbital ordering can also be explained by purely electronic mechanism suggested by Kugel and Khomskii in 1973. Partial occupancy of t_{2g} or e_g levels in multi band Hubbard model plays an important role in determining the spin dynamics and the model describing such a mechanism is the Kugel-Khomskii Model.

Kugel and Khomskii [73] have shown that in systems with strong correlations having degenerate t_{2g} or e_g, orbital ordering could take place due to purely superexchange mechanism through many body effects. The energy gains, calculated by second-order perturbation methods, associated different spin and orbital configurations via superexchange mechanism is shown in Fig. 1.16.

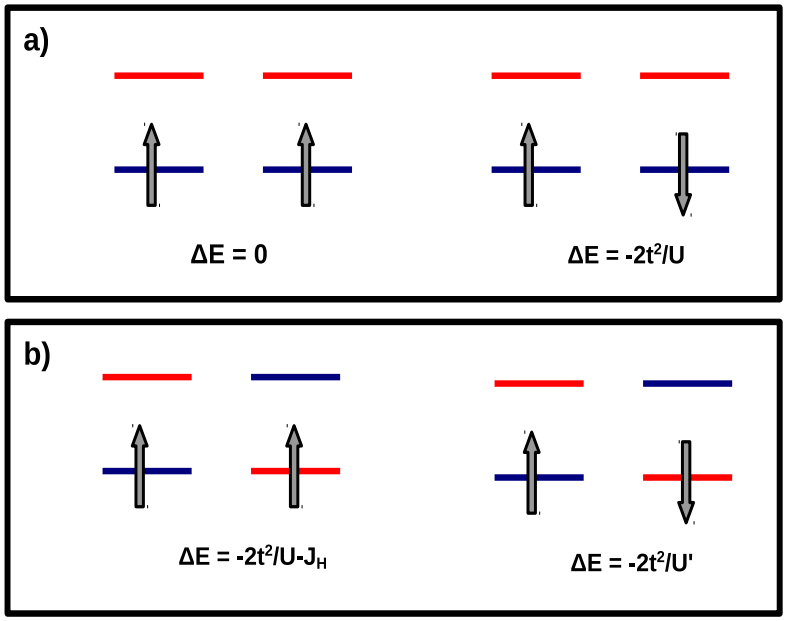

Figure 1.16: Superexchange in the case of two-fold degenerate orbitals, two colors blue and red represent two different orbitals. (a) shows ferromagnetic and antiferromagnetic spin alignment and corresponding energies in ferro-orbital stacking and (b) shows ferromagnetic and antiferromagnetic spin alignment and corresponding energies in antiferro-orbital stacking.

The intra and inter-orbital Coulomb repulsion and the Hund's exchange coupling strength are represented by U, U' and J_h respectively. It is clear that ferromagnetic spin configuration with different orbital character is favored by Hund's coupling in this model. A simple example is magnetic ordering in $LaMnO_3$, where the antiferro orbital ordering in xy-plane results in the ferromagnetic spin coupling in the plane, while ferro-orbital stacking leads to antiferromagnetic alignment of spins in z-direction.

Orbital ordering usually occurs at higher temperatures (typically ~ 5 times higher) than magnetic ordering. Also, in specific case, the orbital ordering can lead to reduction of dimensionality of electronic subsystem. For example in the case of $KCuF_3$ [74], because of the occupation of particular orbitals, the antiferromagnetic exchange interaction in z-direction is much stronger than xy-plane ferromagnetic exchange interaction. Due to this effect, despite of being in almost cubic lattice, the magnetic lattice is one-dimensional antiferromagnet.

1.6 Magnetism in Double-Perovskite

The first report of ferrimagnetic behavior above the room in Re based double perovskite (DP) oxides was by Longo and Ward in 1961 [75]. Double perovskite oxides have the chemical formula of $A_2BB'O_6$, where A site is occupied by divalent or trivalent cation, B and B′ sites are occupied by two different transition metal elements. From the structural point of view, double perovskite $A_2BB'O_6$ structure can be constructed by replacing B-cation by B′-cation alternately in a ABO_3 lattice in all the three directions. This finding led to discovery of many other ferromagnetic DP materials such as Sr_2FeMoO_6 [76]. The highly conductive behavior of these compounds and the room temperature ferrimagnetic ordering of B and B′ sites (Sr_2FeReO_6 $T_c = 401$ K; Sr_2FeMoO_6 $T_c = 420$ K) despite of the separation between the magnetic sites $\sqrt{2}$ larger than that in the usual perovskite lattice, ruled out the ordinary superexchange mechanisms to explain the underlying physics. In a study on Sr_2FeMoO_6 by Sarma *et al.* [77], they proposed an unusual mechanism in which the hopping interaction between nearest neighbor Fe and Mo atoms induced magnetic moment on Mo sites which are otherwise nonmagnetic because of the highly delocalized nature of the 4*d* orbitals. This induced antiferromagnetic coupling between spins on Fe and Mo sites consequently results in ferromagnetic coupling between the Fe atoms, explaining the room temperature ferromagnetic T_c of Sr_2FeMoO_6.

Among various models considered to describe magnetism in these materials, the most accepted one is a Kondo-like model [78–81] in which the interaction between the occupied Fe up spin states is approximated by a localized spin (**S**) and the itinerant conduction electron spin (σ) is antiferromagnetic in nature.

$$H = -t \sum_{<ij>,\sigma} c^{\dagger}_{i\sigma} c_{j\sigma} - J_H \sum_{i,\alpha,\beta} \vec{S}_i \cdot c^{\dagger}_{i\alpha} \vec{\sigma}_{\alpha\beta} c_{i\beta} + H.C. \tag{1.13}$$

where at each site the itinerant spin rotated in such a way that the spin quantization axis is parallel to the core spin direction at that site. This model successfully explained the high T_c behavior of Sr_2FeMoO_6 which had one electron on the nonmagnetic Mo atom. However, their prediction about the suppression of critical temperature T_c with increase in electron density above a certain value contradict the experimental findings of increase in T_c with electron doping.

Further progress was made by Brey *et. al.* [82] and they showed that (Fig. 1.17) by considering the electron-electron correlations on the non-magnetic site, one can penalize the double occupancy of site lifting the degeneracy of the up and down spin states at the nonmagnetic sites. By introduction of a Hubbard U term of a non-magnetic site, they were able to capture the experimental trend of increasing T_c with electron doping.

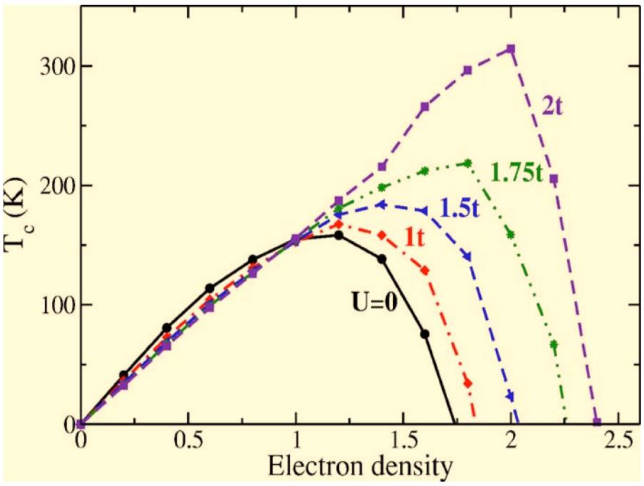

Figure 1.17: Increase in T_c with electron density at different value of Hubbard U on the nonmagnetic site. The suppression of T_c is shifted towards the high electron density with the moderate value of electronic correlation on the nonmagnetic site. This figure is taken from Ref. [82]

1.7 Confinement Effects On Electronic Structure Of TM Compounds

The simplest example of confinement effect can be found in the text books as a particle-in-a-box problem. The confinement of particles in this problem lead to quantization of energy eigenvalues with a drastic modification in the electronic structure. There are various examples of size dependent bang gap variation among nanomaterials and was attributed to effects of quantum confinement. The average separation between the electron-hole pair in a bound state generated by excitation across the band gap in a semiconductor is the Bohr exciton radius. When the system size is smaller than the corresponding Bohr exciton radius, the role of quantum confinement effects in determining the electronic structure of the materials becomes crucial.

A similar variation of the band gap is found in two-dimensional transition metal dichalcogenides as a function of layer thickness. These transition metal dichalcogenides have layered structural form with chemical formula as MX_2 where M = Mo, Ti, W etc. and X = S, Se, Te etc. Different layers in these compounds are interacting by weak van der Waals interactions. The properties of these materials change drastically while going from bulk to the monolayer limit. For example, the bulk MoS_2 has an indirect bandgap of 1.3 eV which get enhanced to 1.6 eV in the bilayer limit. This band gap of MoS_2 further get enhanced to 1.9 eV with a transition from indirect to direct band gap in the monolayer limit. Similarly, in the case of $MoSe_2$, an indirect band gap of 1.1 eV of bulk changes into a direct band gap of about 1.66 eV in the monolayer limit.

In this thesis we have tried to understand some of the unusual yet interesting phenomenon which exist in transition metal compounds. It is an attempt to address a number of issues like spin, charge and orbital ordering in correlated materials by employing a combination of *ab initio* calculations as well as a mapping onto model Hamiltonians wherever possible. A major part of this thesis is devoted to the study of magnetism in transition metal oxides. Usual examples among the compounds exhibiting magnetism have been considered. These include antiferromagnetic metals, ferromagnetic insulators, as well as a double perovskite oxide. In some instances charge ordering or orbital ordering accompanies the magnetism and their role in the observed magnetic order has been investigated.

In chapter 2, I first discuss the basic methods used in electronic structure calculations. Starting from the many body Hamiltonian, I have discussed different approximations and approaches which has been useful to understand the basic principles on which density function theory work.

Recently there is a shift in focus towards antiferromagnetic spintronics [86, 87]. There are very few examples of antiferromagnetic metals among the transition metal oxides which are needed for an oxide based electronics. The general convention is that the antiferromagnetism comes hand in hand with an insulating state while ferromagnetism is usually accompanied by metallicity. Among the few examples of transition metal oxides, $CaCrO_3$ is one which has C-type antiferromagnetic metallic ground state with T_N of ~ 90 K. If one looks for some other examples of AFM-metal among $3d$ transition metal oxides, considering the most well studied compound, the phase diagram of manganites obtained by varying hole doping concentrations (discussed previously in the section of charge ordering) does not have a region in which such a phase is

stable. Other phases in the phase diagram are believed to be stabilized by the interplay between electronic and lattice degrees of freedom. So one has to go to a system where the effect of electron-phonon coupling is low which is actually the case for a $5d$ transition metal oxide where we can have a phase diagram which is not significantly modified by electron-phonon interactions. But due to the large bandwidth of this class of compounds, it is not very common to find a magnetic member among them. The perovskite oxide $NaOsO_3$ is an example of a $5d$ transition metal oxide with an G-type antiferromagnetic insulating ground state and is believed to a Slater insulator. In a previous study by Middey *et al.* [83], using *ab initio* calculations, they have shown that with 25 % electron doping, one can stabilize a robust G-type antiferromagnetic metallic ground state. However, it is unclear whether this is a generic feature or there is something special about electron doped $NaOsO_3$ which allowed an antiferromagnetic metallic phase to be stabilized. In view of this, chapter 3 of this thesis focuses on the study of electron doping as a possible route to realize the antiferromagnetic metallic phase in a $5d$ transition metal oxide. We found that an antiferromagnetic metallic ground state was found in the small U regime and a further increase of U resulted in localization of the extra electron onto a particular transition metal site giving rise to a charge ordered insulating phase. The study was done using a multiband Hubbard Hamiltonian and the operative microscopic mechanisms behind it have been examined in detail. We also compare our results with the a $3d$ transition metal oxide case and find surprisingly that in this case their is no antiferromagnet metallic region in the obtained phase diagram. This led us to the conclusion that the Hund's exchange interaction plays an important role in determining the magnetism in the metallic phases found in the phase diagram for doped transition metal oxides.

Possible changes in the resistivity/conductivity of a system would occur with doping of extra charge carriers into it and the system may go from an insulator to a metal beyond a certain percolation threshold value as is explained by the percolation theory. However, there are some special examples of systems which refuse to become metallic even at high carrier doping concentrations. For example, $La_{1-x}Sr_xCrO_3$ [84] and $La_{1-x}Sr_xFeO_3$ [85] remain insulating even at hole doping concentrations of 50 % and 40 % respectively. It was suggested that the local polaronic distortions localize the doped holes in states much above the Fermi energy and these states do not have sufficient bandwidth to overlap with the valence band maximum and hence

an insulating ground state follows. In chapter 4 of this thesis, we have studied the operational mechanism behind the robust insulating state present in some perovskite oxides even at large carrier doping concentrations. Using a multiband Hubbard model, we show that the exchange splitting induced localization of carriers and the polaronic distortions play an almost equal role in driving the system insulating among the $3d$ transition metal oxides. We rule out the role of large Hund's interaction in the stabilization of such an unusual ground state and show that this mechanism will be operational in systems with small values of Hund's interaction also, suggesting that there could be examples among the $4d$ and the $5d$ transition metal oxides which also refuse to go metallic on doping. This mechanism is operational at half-filling of the band and is elucidated for the first time. We also show that the superexchange mechanism is weaker in the case of hole doping when compared to the electron doping case which leads to asymmetry in the phase diagrams obtained in these two cases. Based on our results we suggested hole doping as a more viable route to stabilize antiferromagnetic metallic state when compared to electron doping among the $5d$ transition metal oxides.

The large Hund's stability of half-filled bands manifests itself in other cases. Doping Cr at the V site in VO_2 has been seen to stabilize the +3 valency in Cr as was found in the experimental studies, while an isovalent substitution would have led to a +4 valency being associated with Cr. An unusual ferromagnetic insulating was found upto $\sim$ 18 % Cr doping in these experimental studies, however it was not very clear what lead to the formation of Cr^{+3} ionic state along with V atom nearest to Cr being in +5 ionic state rather than +4 state. The first principle studies in the past predicted a half-metallic ferromagnetic ground state in this case which was clearly not in agreement with the experiments. In chapter 5 of this thesis, we show that the Cr^{+3} state indeed emerges from the strong stability associated with half-filled t_{2g} orbitals and is additionally stabilized by the formation of V^{+5} at the nearest neighbor V site. The attractive Coulomb interaction between Cr^{+3} and V^{+5} sites provides additional stability. The presence of empty d orbitals at the V^{+5} sites and filled t_{2g} orbitals at the Cr^{+3} sites leads to hopping pathways that stabilize a ferromagnetic insulating state. By mapping onto a tight binding model involving Cr,V d states and O p states in the basis, we are able to show for the first time how charge ordering helps in stabilizing the ferromagnetic insulating state in this system.

The low temperature and high magnetic field CMR response of manganites initiated extensive research towards new materials having magnetic transition temperature above room temperature and a new class of materials named double perovskite have been found to be very promising. The magnetic transition temperature of a material usually depends on distance between the magnetic atoms. In double perovskite (DP) oxides, the magnetic lattice is diluted by nonmagnetic ions and so the distance between closest magnetic atoms is now $\sqrt{2}$ times larger than that in the perovskite oxide. An increase in the distance between the magnetic ions implies weaker exchange interactions and hence a decrease in the T_c is expected for such compounds. Despite this fact, many DP compounds have their T_c above room temperature. In chapter 5, I have investigated magnetism in a double perovskite oxide Sr_2FeReO_6 and a microscopic model has been proposed to describe the magnetic properties. First, using the *ab initio* method, we have shown that their is a substantial enhancement in the stability of ferromagnetic ground state when we considered a U of 1 eV on the non-magnetic Re site (U_{Re}). Using the frozen magnon approach, we estimated the exchange interaction parameters in both cases, when there was no U_{Re} and with a U_{Re} of 1 eV while the U at Fe site (U_{Fe}) was fixed at a value of 2.5 eV. We found that the first neighbor exchange interaction strength J_1 got doubled and is ferromagnetic with $U_{Re} = 1$ eV while most surprisingly the second neighbor exchange interaction strength J_2 which was antiferromagnetic for $U_{Re} = 0$ V has changed its sign and become ferromagnetic with $U_{Re} = 1$ eV. Examining the density of states for the ferromagnetic as well as the competing antiferromagnetic state provide evidence for an effective exchange splitting on the Re site in the antiferromagnetic state with the application of U_{Re}. This destabilizes hopping pathways in the antiferromagnetic configuration and hence leads to an enhancement in the ferromagnetic stability. This hypothesis was further verified by varying the exchange splitting at the Re site within our multiband Hubbard Hamiltonian and calculating the stability of the ferrimagnetic ground state with respect to the competing antiferromagnetic state. Here also we find the similar enhancement in the ferromagnetic stability with increase in exchange splitting at the Re site. This suggests a general route to enhanced Curie temperatures of these materials. A comparison with another similar double perovskite Sr_2FeMoO_6 having one valence electron at Mo site was presented and the role of two valence electrons at the Re site in the huge ferromagnetic stability with the application of U_{Re} was outlined.

While chapter 3-5 have examined the properties of transition metal compounds where the spin, charge and lattice degrees of freedom play an active role, in chapter 7 we consider a class of transition metal compounds where the spin, lattice and charge degree of freedom play no role. The electronic structure of transition metal dichalcogenides changes with change in the number of layers. Studies in the past suggested that the quantum confinement effect as well as interlayer hopping interactions play and important role in determining the electronic structure of such materials. In chapter 7, with the help of *ab initio* method as well as using a tight binding model, we have examined the evolution of electronic structure of the whole series of transition metal dichalcogenides as a function of layer thickness. We examine the role of interlayer hopping interactions, geometric confinement effects as well as the Madelung potential effects in the changes in the electronic structure found with thickness. Considering a tight binding for MoS_2 and $MoSe_2$, with Mo d and S/Se p orbitals in the basis, we quantitatively explain the role of each of these effects on the electronic structure. We found that the interlayer hopping interactions play a crucial role in determining the electronic structure in these layered materials which are referred as van der Waals heterostructures due to their weak interlayer coupling, questioning the nomenclature. We ruled out any crucial roles of geometric confinement effect as well the Madelung potential in observed changes in the electronic structure

Bibliography

[1] R. M. BOZORTH, Rev. Mod. Phys., **19**, 29 (1947).

[2] Li Shu-hua, *Origine de la Boussole 11. Aimant et Boussole*, Isis **45**, 175 (1954).

[3] R. T. Merrill and M.W. McElhinny, *The Earth´s magnetic field: Its history, origin and planetary perspective*, (second edition), San Francisco: Academic press, 1 (1983).

[4] J. C. Maxwell, Phil. Trans. R. Soc. Lond. **155**, 459 (1865).

[5] D. J. Griffiths, *Introduction to electrodynamics*, (third edition), Prentice Hall, 559 (1999).

[6] S. Goudsmit and R. de L. Kronig, Naturwissenschaften **13**, 90 (1925).

[7] G. E. Uhlenbeck and S. Goudsmit, Naturwissenschaften **47**, 953 (1925).

[8] P. A. M. Dirac, Proc. R. Soc. London A **117**, 610 (1928).

[9] W. Pauli, Phys. Rev., **58**, 716 (1940).

[10] M. Massimi, *Pauli´s Exclusion Principle*, Cambridge University Press (2005).

[11] G. Herzberg, *Atomic Spectra and Atomic Structure*, Dover Publications (1944).

[12] F. J. Dyson and A. Lenard, J. Math. Phys. **8**, 423 (1967).

[13] F. J. Dyson and A. Lenard, J. Math. Phys. **9**, 698 (1968).

[14] F. J. Dyson, J. Math. Phys. **8**, 1538 (1967).

[15] A. Galindo and C. Sanchez del Rio, Am. J. Phys. **29**, 582 (1961).

[16] R. Skomski and J. M. D. Coey, *Permanent Magnetism*, Institute of Physics, Bristol (1999).

[17] R. Skomski, *Simple Models of Magnetism*, Oxford University Press (2008).

[18] V. L. Moruzzi, J. F. Janak and A. R. Williams, *Calculated Electronic Properties of Metals*, Pergamon, New York (1978).

[19] S. Middey, Ashis Kumar Nandy, S. K. Pandey, Priya Mahadevan and D. D. Sarma, Phys. Rev. B **86**, 104406 (2012).

[20] J. Kubler, A. R. Williams and C. B. Sommers, Phys. Rev. B **28**, 1745 (1983).

[21] E. Sasioglu, L. M. Sandratskii, P. Bruno and I. Galanakis, Phys. Rev. B **72**, 184415 (2005).

[22] S. Chikazumi, *Physics of Ferromagnetism*, Oxford University Press, New York, (1997).

[23] H. A. Kramers, Physica **1**, 182 (1934).

[24] P. W. Anderson, Phys. Rev. **79**, 350 (1950).

[25] A. Galindo and C. Sanchez del Rio, Am. J. Phys. **29**, 582 (1961).

[26] R. J. Boyd and C. A. Coulson, J. Phys. B: At. Mol. Phys. **7**, 1805 (1974).

[27] M. A. Ruderman and C. Kittel, Phys. Rev. **96**, 99 (1954).

[28] Tadao Kasuya, Prog. Theor. Phys. **16**, 45 (1956).

[29] C. Kittel, *Quantum Theory of Solids*, (2 Ed.), Wiley, 360 (1987).

[30] C. Zener, Phys. Rev. **82**, 403 (1951).

[31] P. -G. de Gennes, Phys. Rev. **118**, 141 (1960).

[32] W. E. Pickett and D. J. Singh, Phys. Rev. B **53**, 1146 (1996).

[33] K. Kubo and N. Ohata, J. Phys. Soc. Jpn. **33**, 21 (1972).

[34] J. Winterlik, G. H. Fecher, C. A. Jenkins, C. Felser, C. Muhle, K. Doll, M. Jansen, L. M. Sandratskii and J. Kubler, Phys. Rev. Lett. **102**, 016401 (2009).

[35] N. F. Mott and R. Peierls, Proc. Phys. Soc. **A49**, 72 (1937).

[36] F. Blöch, Z. Phys. **57**, 545 (1929).

[37] P. A. Lee and T.V. Ramakrishnan, Rev. Mod. Phys. **57**, 287 (1985).

[38] D. Belitz and T. R. Kirkpatrick, Rev. Mod. Phys. **66**, 261 (1994).

[39] N.F. Mott, *Metal Insulator Transitions*, Barnes and Noble, New York (1974).

[40] K. Terakura, A. R. Williams, T. Oguchi and J. Kubler, Phys. Rev. Lett. **52**, 1830 (1984).

[41] K. Terakura, T. Oguchi, A. R. Williams and J. Kubler, Phys. Rev. B **30**, 4734 (1984).

[42] G. A. Sawatzky and J. W. Allen, Phys. Rev. Lett. **53**, 2339 (1984).

[43] N. F. Mott, Proc. Phys. Soc. London, Sect. **A62**, 416 (1949).

[44] J. G. Bednorz and K.A. Muller, Z. Phys. B **64**, 189 (1986).

[45] J. Hubbard, Proc. Roy. Soc. A **277**, 237 (1964); *ibid.* **281**, 401 (1964).

[46] M. Imada, A. Fujimori and Y. Tokura, Rev. Mod. Phys. **70**, 1039 (1998).

[47] Carl J. Balheusen, *An Introduction to Ligand Field Theory*, McGraw Hill (1962).

[48] R. Schlapp and W.G. Penney, Phys. Rev. **42**, 666 (1932).

[49] E. Pavarini and E. Koch, Phys. Rev. Lett. **104**, 086402 (20010).

[50] H. Sawada, Y. Morikawa, K. Terakura and N. Hamada, Phys. Rev. B **56**, 12154 (1997).

[51] C. Zobel, M. Kriener, D. Bruns, J. Baier, M. Grüninger, T. Lorenz, P. Reutler, and A. Revcolevschi, Phys. Rev. B **66**, 020402(R) (2002).

[52] György Vankó, Jean-Pascal Rueff, Aleksi Mattila, Zoltán Németh, and Abhay Shukla, Phys. Rev. B **73**, 024424 (2006).

[53] H. -T. Jeng, S. -H. Lin and C. -S. Hsue, Phys. Rev. Lett. **97**, 067002 (2006)

[54] H. A. Jahn and E. Teller, Proc. Roy. Soc. London A **161**, 220 (1937).

[55] B. Lake, D. A. Tennant, C. D. Frost and S. E. Nagler, Nature Materials **4**, 329 (2005).

[56] J. Hemberger, H. -A. Krug von Nidda, V. Fritsch, J. Deisenhofer, S. Lobina, T. Rudolf, P. Lunkenheimer, F. Lichtenberg, A. Loidl, D. Bruns and B. Buchner, Phys. Rev. Lett. **91**, 066403 (2003).

[57] Z. Fang and N. Nagaosa, Phys. Rev. Lett. **93**, 176404 (2004).

[58] D. I. Khomskii, *Transition Metal Compounds*, Cambridge University Press (2014).

[59] D. I. Khomskii, *Basic Aspects of the Quantum Theory of Solids: Order and Elementary Excitations*, Cambridge University Press (2010).

[60] Yosuke Nagaoka, Phys. Rev. **147**, 392 (1966).

[61] Yosuke Nagaoka, Solid State Comm. **3**, 409 (1965).

[62] David R. Penn, Phys. Rev. **142**, 350 (1966).

[63] D. I. Khomskii, Sov. Phys. - Phys. of Metal and Metallography **29**, 31 (1970).

[64] J. van den Brink and Daniel Khomskii, Phys. Rev. Lett. **82**, 1016 (1999).

[65] Y. Tokura and N. Nagaosa, Science **288**, 5465 (2000).

[66] Priya Mahadevan, K. Terakura, and D. D. Sarma, Phys. Rev. Lett. **87**, 066404 (2001).

[67] S. W. Cheong and H. Y. Hwang, *Ferromagnetism versus charge/orbital ordering in mixed-valent manganites Colossal Magnetoresitance Oxides*, London: Gordon and Breach (2000).

[68] Z. Jirak, S. Krupiaka and Z Simsa, J. Mag. Mag. Mater. **53**, 153 (1985).

[69] J. P. Hill *et. al.*, arXiv:cond-mat/0105064.

[70] Y. Tomioka, A. Asamitsu, H. Kuwahara, Y. Moritomo, and Y. Tokura, Phys. Rev. B **53**, 1689(R) (1996).

[71] I. S. Elfimov, V. I. Anisimov, and G. A. Sawatzky, Phys. Rev. Lett. **82**, 4264 (1999).

[72] H. Sawada, N. Hamada, K. Terakura and T. Asada, Phys. Rev. B **53**, 12742 (1996).

[73] K. I. Kugel and D. I. Khomskii, Sov. Phys. Usp. **25**, 231 (1982).

[74] K. I. Kugel and D. I. Khomskii, Sov. Phys.-JHTP **37**, 725 (1973).

[75] J. Longo and R. Ward, J. Am. Chem. Soc. **83**, 2816 (1961).

[76] K. I. Kobayashi, T. Kimura, H. Sawada, K. Terakura and Y. Tokura, Nature **395**, 677 (1998).

[77] D. D. Sarma, P. Mahadevan, T. Saha-Dasgupta, S. Ray and A. Kumar, Phys. Rev. Lett. **85**, 2549 (2000).

[78] J. Kondo, Prog. of Theor. Phys. **32**, 37 (1964).

[79] K. Phillips, A. Chattopadhyay and A. J. Millis, Phys. Rev. B **67**, 125119 (2003).

[80] J. L. Alonso, L. A. Fernandez, F. Guinea, F. Lesmes and V. Martin-Mayor, Phys. Rev. B **67**, 214423 (2003).

[81] G. Jackeli, Phys. Rev. B **68** 092401 (2003).

[82] L. Brey, M. J. Calderson, S. D. Sarma and F. Guinea, Phys. Rev. B **74**, 094429 (2006).

[83] S. Middey, Saikat Debnath, Priya Mahadevan and D. D. Sarma, Phys. Rev. B **89**, 134416 (2014).

[84] K. Maiti and D. D. Sarma, Phys. Rev. B **54**, 7816 (1996).

[85] A.Chainani, M. Mathew and D. D. Sarma, Phys. Rev. B **48**, 14818 (1993).

[86] Claude Chappert, Albert Fert and Frédéric Nguyen Van Dau, Nat. Mat. **6**, 813 (2007).

[87] T. Jungwirth, X. Marti, P. Wadley and J. Wunderlich, Nat. Nano. **11**, 231 (2016).

Chapter 2

Methodology

2.1 Introduction

Physical systems which surround us in our day to day life are made of atoms. An atom consists of a dense and heavy positively charge particle called nucleus surrounded by light negatively charged cloud of electrons. It is only after development of the theoretical methods of quantum mechanics and statistical mechanics that the behavior of electrons in a material can be understood in terms of probabilistic predictions. In quantum mechanics, the motion of electrons in a solid is described by wave functions associated with them having certain discrete energy. An immediate question then arises that what will be the possible energies and the wave functions associated with these electrons.

According to quantum mechanics, motion of the particles in a system is described by the many particle Schrödinger's equation given as,

$$H\Psi(\mathbf{R}_i;\mathbf{r}_i) = E\Psi(\mathbf{R}_i;\mathbf{r}_i)$$

Here $\Psi(\mathbf{R}_i;\mathbf{r}_i)$ is the many particle wavefunction describing the state of the system with ions/nucleus at positions $\mathbf{R}_i$ and electrons at positions $\mathbf{r}_i$. H is the Hamiltonian of the system with corresponding eigenvalue E representing energy of the system.

Within the non-relativistic limit, the most general Hamiltonian H of any many particle system can be written as

$$H = -\frac{\hbar^2}{2m_e}\sum_i \nabla_i^2 + \frac{1}{2}\sum_{i\neq j}\frac{e^2}{|\mathbf{r}_i - \mathbf{r}_j|} - \frac{\hbar^2}{2M_I}\sum_I \nabla_{\mathbf{R}_I}^2 + \frac{1}{2}\sum_{I\neq J}\frac{Z_I Z_J e^2}{|\mathbf{R}_I - \mathbf{R}_J|} - \sum_{i,I}\frac{Z_I e^2}{|\mathbf{R}_I - \mathbf{r}_i|} \quad (2.1)$$

In this Hamiltonian, the electronic indices are represented by the lower case scripts and the nuclei/ionic part with charge Z_I and mass M_I denoted by the upper case subscripts. Here e is the electronic charge. The first two terms in the Hamiltonian represent kinetic energy of electrons and the electron-electron Coulomb repulsion respectively. The third and fourth term represent kinetic energy and ion-ion interactions of the ions respectively. Fifth term represents the ion-electron interactions. As discussed previously, this Hamiltonian is the most informative one describing the interactions of electrons and nuclei with each other and themselves. This Hamiltonian when used in the Schrödinger's equation can predict various properties exhibited by the system.

In a few cases only, this problem can be fully solved analytically but mostly it is almost impossible to solve this many particle problem within the full quantum mechanical treatment. Also even the numerical solutions to this problem is limited to small number of particles. The electron and ions with each having a particular dynamics and particularly the many particle Coulomb interaction term which makes decoupling of the wavefunction difficult contribute to the prevention of the exact solution to this problem. One has to then take care of the electronic (3 spatial + 1 spin)n degrees of freedom and ionic 3N spatial degree of freedom all coupled together. There are large number of electrons in a typical solid which make this problem even more complex and go beyond the computing capacity of any computer. In order to simplify this problem, some assumptions have been made to solve this problem. The first approximation in this context is based upon the the adiabatic separation of electronic and ionic degrees of freedom called the Born-Oppenheimer approximation (BAO) [1].

2.2 The Born-Oppenheimer Approximation

Even though the change in momentum of electrons and nuclei due to the forces originated from interactions of their charges are similar in nature, the timescale associated with their motion are quite different. The massiveness of the nuclei when compared to the electrons make their motion of nuclei much slower than the electrons. Based on this fact, an approximation can be made that at any instant of time, electrons will be in their ground state with respect to the instantaneous ionic configuration. So one can decouple the electronic and the nuclear motion and hence for a particular ionic configuration, the electronic wavefunction is a solution of the Schrödinger's equation. The new electronic Hamiltonian can be obtained from Eq. 2.1 as,

$$H^e_{BOA} = -\frac{\hbar^2}{2m_e}\sum_i \bigtriangledown_i^2 + \frac{1}{2}\sum_{i\neq j}\frac{e^2}{|\mathbf{r}_i - \mathbf{r}_j|} - \sum_{i,I}\frac{Z_I e^2}{|\mathbf{R}_I - \mathbf{r}_i|} \tag{2.2}$$

The eigen value equation is then used to evaluate the energy of an electronic configuration with respect to a particular ionic configuration given as

$$H^e_{BOA}\psi_n(\mathbf{r};\mathbf{R}) = \epsilon_n\psi_n(\mathbf{r};\mathbf{R}) \tag{2.3}$$

where $\psi_n(\mathbf{r};\mathbf{R})$ is the decoupled electronic wavefunction represents an electronic state for the set of nuclear positions, $\mathbf{R}$. It can be then used to obtain the states associated with the ionic motion.

Even after the simplification of the original Hamiltonian with this adiabatic approximation, it is still difficult to solve the electronic part of the Hamiltonian. A major part of complexity is in solving the e^--e^- Coulomb interaction term which involves coordinates of two different electrons. In order to extend it's applicability to the realistic systems, one has to make additional approximations. Progress have been made in this direction and different theories like the Hartree-Fock (HF) and Density Functional theory (DFT) were developed in which the two body interaction term is replaced by an effective single body potential. We will try to solve the previously discussed electronic Hamiltonian only within these HF and DFT methods.

2.3 Ground State Solution : The Variational Principle

In order to calculate the energy eigen values of the Hamiltonian when a system is in any arbitrary state Ψ, the expectation value of the Hamiltonian can be written as,

$$E = \frac{\langle\Psi|H|\Psi\rangle}{\langle\Psi|\Psi\rangle} \tag{2.4}$$

According to the variational principle, any initially guessed eigenfunction Ψ_i will lead to a state which is higher in energy than the ground state and the ground state eigen function $|\Psi_0\rangle$ and the associated energy $E[\Psi_0] = E_0$, can be obtained by a full minimization of functional $E[\Psi_i]$ with respect to all allowed N-electrons wavefunctions $\{\Psi_i\}$,

$$E_0[\Psi_0] = \min_{\Psi_i \to \Psi_0} E[\Psi_i] \tag{2.5}$$

Thus, with variational principle, one can determine the ground state properties of a given many particle system. The main issue arises here the large number of initial trail wavefunctions and their choice in order to have a quick approach towards the ground state wave function.

2.4 Ground State Determination Of A Many Particle System

2.4.1 Hartree-Fock Approximation

In order to solve the issue discussed in the previous section, Hartree (1982) [2] assumed the complex N-electron wavefunction into a simple form of product of N one-electron wavefunctions considering them non-interacting,

$$\Psi^H(\mathbf{r}_i) = \phi_1(\mathbf{r}_1)\phi_2(\mathbf{r}_2).....\phi_N(\mathbf{r}_N) \tag{2.6}$$

where ϕ_i represent the individual one electron wave functions. These single particle states are considered to be orthonormal. Within this approximation, the Fermionic nature of the electrons and hence the effects of exchange symmetry was not taken into account. Fock in 1930 [3]

improved on it by introducing the antisymmetric nature of the electron wave function. This is Hartree-Fock approximation. Now, the many body wavefunction can be written in terms of Slater [4] determinant with the antisymmetric orthonormal N-one electron wavefunctions as,

$$\Psi^{HF}(\mathbf{r}_i) = \frac{1}{\sqrt{N!}} \begin{vmatrix} \phi_1(\mathbf{r}_1) & \phi_1(\mathbf{r}_2) & \cdots & \phi_1(\mathbf{r}_N) \\ \phi_2(\mathbf{r}_1) & \phi_2(\mathbf{r}_2) & \cdots & \phi_2(\mathbf{r}_N) \\ \vdots & \vdots & \ddots & \vdots \\ \phi_N(\mathbf{r}_1) & \phi_N(\mathbf{r}_2) & \cdots & \phi_N(\mathbf{r}_N) \end{vmatrix} \tag{2.7}$$

Note that the sign of the determinant changes with an interchange of the positions of it's two variables, hence sign of the many body wavefunction will change if the positions of the two electrons interchange. Hartree-Fock energy associated with this new wavefunction Ψ^{HF} is given by,

$$E^{HF} = \langle \Psi^{HF} | H | \Psi^{HF} \rangle = \sum_{i,\sigma} E_i^{\sigma} + \sum_{i,j,\sigma_i,\sigma_j} C_{ij}^{\sigma_i\sigma_j} - \sum_{i,j,\sigma} X_{ij}^{\sigma} \tag{2.8}$$

In the above equation, first term represents the contribution due to the kinetic energy and the electron-nucleus interactions and is given by,

$$E_i^{\sigma} = \int \phi_i^{*\sigma}(\mathbf{r}) \left[-\frac{\hbar^2 \nabla^2}{2m_e} + V_{ion}(\mathbf{r}) \right] \phi_i^{\sigma}(\mathbf{r}) d\mathbf{r} \tag{2.9}$$

The second and third in Eq.(2.8) are called the Coulomb integral and the exchange integral respectively and are given by,

$$C_{ij}^{\sigma_i\sigma_j} = \frac{1}{2} \int\int \phi_i^{*\sigma_i}(\mathbf{r}) \phi_j^{*\sigma_j}(\mathbf{r}') \frac{1}{|\mathbf{r} - \mathbf{r}'|} \phi_i^{\sigma_i}(\mathbf{r}) \phi_j^{\sigma_j}(\mathbf{r}') d\mathbf{r} d\mathbf{r}' \tag{2.10}$$

$$X_{ij}^{\sigma} = \frac{1}{2} \int\int \phi_i^{*\sigma}(\mathbf{r}) \phi_j^{*\sigma}(\mathbf{r}') \frac{1}{|\mathbf{r} - \mathbf{r}'|} \phi_j^{\sigma}(\mathbf{r}) \phi_i^{\sigma}(\mathbf{r}') d\mathbf{r} d\mathbf{r}' \tag{2.11}$$

The exchange term, as is clear from Eq.(1.13), is only applicable to the like spins. The origin of this term is traced back to Pauli exclusion principle and is a pure quantum mechanical interaction. It should also be noted here that $C_{ij}^{\sigma_i\sigma_j} = C_{ji}^{\sigma_i\sigma_j}$, $X_{ij}^{\sigma} = X_{ji}^{\sigma}$ and their values for any general solid state system are $C_{ij}^{\sigma_i\sigma_j} \geq X_{ij}^{\sigma} \geq 0$.

Applying the variational principle, one now can obtain the N-single particle Hartree-Fock equation [5] with the variation of ϕ_i^σ subjected to the orthonormality and is given in terms of the Fock operator $\hat{f}$ as,

$$\hat{f}_i^\sigma = \hat{T} + \hat{V}_{ext}(\mathbf{r}) + \hat{V}_{i\sigma}^{HF}(\mathbf{r}) \tag{2.12}$$

In the above equation $\hat{V}_{i\sigma}^{HF}(\mathbf{r})$ is known as Hartree potential and is the average repulsive potential for an electron due to the remaining N-1 electrons and is given by,

$$\hat{V}_{i\sigma}^{HF}(\mathbf{r}) = \sum_{j\sigma'} \hat{C}_j^{\sigma\sigma'}(\mathbf{r}) - \sum_j \hat{X}_j^\sigma(\mathbf{r}), \tag{2.13}$$

where

$$\hat{C}_j^{\sigma\sigma'}(\mathbf{r}) = \int |\phi_{j\sigma}(\mathbf{r}')|^2 \frac{1}{|\mathbf{r} - \mathbf{r}'|} d\mathbf{r}' \tag{2.14}$$

is the Coulomb potential experienced by an electron due to all other electrons in the system. Here it should be pointed out that unlike in the case of Coulomb operator, the exchange operator requires that the value of function ϕ_i^σ should be known at each point in the configuration space in order to get it's outcome with ϕ_i^σ at a single point in space. In this sense the exchange operator is nonlocal in nature and differ from the Coulomb operator which is local in nature i.e. depend only on the value of function ϕ_i^σ at a particular point in configuration space.

Electron correlation effect is ignored in HF approximation. Also, the non-local nature of the exchange term make it's calculation computationally very costly. These facts limit it's application to small and weakly correlated systems.

2.5 Beyond Hartree-Fock Approach

The average Coulomb interactions within the electrons treat the electron correlations poorly and is improved on by considering a linear combination of Slater determinants including the excited electronic states. The linear combination is expressed as,

$$\Psi_{corr} = \sum_i c_i \Psi_i^{HF} \tag{2.15}$$

where Ψ_0^{HF} and $\Psi_i^{HF}, i > 0$ are the HF ground state and excited states respectively and c_i are the weights of different states. The c_i are then optimized by using the variational principle. This method is known full configuration interaction [5] when all possible excited state determinants are considered and becomes computationally very expensive as the number of electrons in the system increases. In order to overcome this problem, the excited states relative to the ground state are often truncated to a certain degree such as single or double excited states in many configuration interaction approximations [6, 7].

Apart from this, another approach to determine the ground state energy is called density functional theory which is computationally less expensive and is quite accurate.

2.6 Density Functional Theory (DFT) Approach

An efficient method to solve the many body Schrödinger equation is density functional theory. It simplifies the extremely complex problem of 6N (3N spatial $\times$ 2 spin coordinates) dimensional dependence of the N-electron wavefunction. The idea was to use the electron density $n(\mathbf{r})$ which depends only on three spatial and one spin coordinates and hence simplification to a 6 dimensional problem independent of the size of the system. Based on this approach, many attempts have been made by Thomas (1927), Fermi (1928), Slater (1951) [8–10] to solve the many particle Schrödinger equation but it was Hohenberg and Kohn (1964) who successfully used this idea to solve for the ground state. The spin independent density of electrons, is defined as,

$$n(\mathbf{r}_i) = N \int \Psi^{\star}(\mathbf{r}_1, .., \mathbf{r}_i, ..., \mathbf{r}_N)\Psi(\mathbf{r}_1, ..., \mathbf{r}_i..., \mathbf{r}_N)dr_1dr_2...d_{i-1}dr_{i+1}...dr_N \tag{2.16}$$

Just like the wavefunction, this $n(\mathbf{r}_i)$ also vanishes at infinity and integrates out to the total number of particles in the system. From the experimental point of view, $n(\mathbf{r})$ is a physical quantity which can be measured in X-ray diffraction experiments.

2.6.1 The Hohenberg and Kohn Theorems

Theorem 1 : This theorem states that the ground state electron density $n_0(\mathbf{r})$ is uniquely defined for a given external potential $V_{ext}(\mathbf{r})$ of a system of many interacting electrons [11].

Conversely, the ground state density $n_0(\mathbf{r})$ uniquely determines the external potential $V_{ext}(\mathbf{r})$ of a system. To prove this let us consider that there are two different external potentials V_{ext} and V'_{ext} which differ by more than a constant and corresponds to the same ground state density $n(\mathbf{r})$. This will result in two different Hamiltonians H and H' and hence two different ground state wavefunctions ψ and ψ' with same ground state density. Since ψ' is not the corresponding ground state of H, so

$$\begin{aligned} E &= \langle\psi|H|\psi\rangle && (2.17)\\ &< \langle\psi'|H|\psi'\rangle = \langle\psi'|H'|\psi'\rangle + \langle\psi|[H-H']|\psi\rangle && (2.18)\\ &< E' + \langle\psi|\left[V_{ext} - V'_{ext}\right]|\psi\rangle && (2.19)\end{aligned}$$

A similar expression can be obtained for E' as,

$$E' < E + \langle\psi'|\left[V'_{ext} - V_{ext}\right]|\psi'\rangle \tag{2.20}$$

Adding both the above equations we get,

$$(E+E') < (E+E') - \langle\psi'|(V_{ext} - V'_{ext})|\psi'\rangle - \langle\psi|(V_{ext} - V'_{ext})|\psi\rangle \tag{2.21}$$

which if we write in terms of density gives,

$$\int n(\mathbf{r})[V_{ext}(\mathbf{r}) - V'_{ext}(\mathbf{r})]d^3r - \int n(\mathbf{r})[V_{ext}(\mathbf{r}) - V'_{ext}(\mathbf{r})]d^3r = 0, \tag{2.22}$$

Hence we get $E + E' < E + E'$ which is clearly contradictory and proves the fact that the wave function must be a unique functional of density and so the energy functional E_V[n] for a given external potential $V_{ext}(\mathbf{r})$ is a unique functional of density too.

Theorem 2 : The second theorem states that for a particular valid V_{ext}, a universal functional of energy $E(n)$ can be defined in terms of the density $n(\mathbf{r})$ and the exact ground state energy is the global minimum value of this functional. $E(n)$ alone is sufficient to determine the exact ground state energy and density. The total energy functional in terms of density $n(\mathbf{r})$ is given

by,

$$\begin{aligned} E[n(\mathbf{r})] &= \langle\Psi|H|\Psi\rangle && (2.23)\\ &= T[n] + E_{int}[n] + \int V_{ext}(\mathbf{r})n(\mathbf{r})d^3r && (2.24)\\ &= F_{hk}[n] + \int V_{ext}(\mathbf{r})n(\mathbf{r})d^3r. && (2.25) \end{aligned}$$

$F_{hk}[n]$ in the above equation is the sum of kinetic energy ($T[n]$) and the electron-electron interaction term ($E_{int}[n]$) and is called Hohenberg-Kohn functional. This $F_{hk}[n]$ is universal for any many-electron system having unique density $n(\mathbf{r})$. The ground state energy of the system can be determined using this functional only when the density $n_0(\mathbf{r})$ is the ground state density corresponding to a unique V_{ext}. This implies that for any density $n'(\mathbf{r})$ other than ground state density,

$$E[n'(\mathbf{r})] = F_{hk}[n'] + V_{ext}[n'] \geq E[n_0(\mathbf{r})] \quad (2.26)$$

Therefore using the variational principle, one can find the exact ground state density and hence energy of the system by minimizing the total energy, calculated with the functional $F_{hk}[n]$, with respect to variations in density $n(\mathbf{r})$.

2.7 Kohn-Sham Formulation Of Density Functional Theory

The unknown functional form of Hohenberg-Kohn functional makes it difficult to calculate the ground state energy in terms of the electron density. An approach to solve this problem was proposed by Kohn and Sham and the idea was the replacement of interacting N-electrons system by a hypothetical a system of N non-interacting electrons whose ground state density coincides with the interacting N-particle system. Within this formalism it would be possible to make realistic approximations to the universal functional $\mathrm{F}_{hk}[\mathrm{n}(\mathbf{r})]$. This ground state density $n(\mathbf{r})$ of N-independent electron system can be written as,

$$n(\mathbf{r}) = \sum_i \phi_i^\star(\mathbf{r})\phi_i(\mathbf{r}). \quad (2.27)$$

Using the variational principle one can minimize the energy functional with respect to the ϕ_i. The advantage of this method is that the eigenstate of the single particle Hamiltonian of N-non interacting particles can be expressed in terms of Slater determinant.

The kinetic term $T_0[n(\mathbf{r})]$ and the electron-electron Coulomb interaction $\mathrm{V}_H[n(\mathbf{r})]$ (Hartree potential) in terms of density take the form,

$$T_0[n(\mathbf{r})] = \sum_i \langle\phi_i| - \frac{\hbar^2\nabla^2}{2m_e}|\phi_i(\mathbf{r})\rangle \tag{2.28}$$

$$V_H[n(\mathbf{r})] = \frac{e^2}{2}\int n(\mathbf{r})\frac{1}{|\mathbf{r}-\mathbf{r}'|}n(\mathbf{r}')d^3r d^3r' \tag{2.29}$$

$$= \frac{e^2}{2}\sum_{i,j}\langle\phi_i\phi_j|\frac{1}{|\mathbf{r}-\mathbf{r}'|}|\phi_i\phi_j\rangle \tag{2.30}$$

Adding and subtracting $T_0[n(\mathbf{r})]$ and $V_H[n(\mathbf{r})]$ in the Hohenberg-Kohn functional given in Eq. 2.25,

$$E[n(\mathbf{r})] = F_{hk}[n] + \int V_{ext}(\mathbf{r})n(\mathbf{r})d^3r + (T_0[n(\mathbf{r})] - T_0[n(\mathbf{r})] + V_H[n(\mathbf{r})] - V_H[n(\mathbf{r})]) \tag{2.31}$$

$$= T_0[n(\mathbf{r})] + V_H[n(\mathbf{r})] + \int V_{ext}(\mathbf{r})n(\mathbf{r})d^3r + E_{XC}[n(\mathbf{r})] \tag{2.32}$$

where $E_{XC}[n(\mathbf{r})]$ is called Exchange-Correlation functional [13] and is defined as,

$$E_{XC}[n(\mathbf{r})] = F_{hk}[n] - T_0[n(\mathbf{r})] + V_H[n(\mathbf{r})] \tag{2.33}$$

Therefore the energy functional in the Kohn-Sham scheme as in terms of N orbitals can be given as,

$$E[n(\mathbf{r})] = \sum_i \langle\phi_i| - \frac{\hbar^2\nabla^2}{2m_e} + V_{ext}(\mathbf{r})|\phi_i\rangle + \frac{e^2}{2}\sum_{i,j(i\neq j)}\langle\phi_i\phi_j|\frac{1}{|\mathbf{r}-\mathbf{r}'|}|\phi_i\phi_j\rangle + E_{XC}[n(\mathbf{r})].$$

The ground state density can be obtained from above by varying the orbitals under the constraint of orthonormalization condition of wave functions $\phi_i(\mathbf{r})$. Minimization of $E[n(\mathbf{r})]$ using variation

principle under the constrained of normalized density ($\int n(\mathbf{r})d(\mathbf{r}) = N$) as,

$$\frac{\delta}{\delta n(\mathbf{r})}\left[E[n] - \mu_L\left(\int n(\mathbf{r})d(\mathbf{r}) - N\right)\right] = 0 \tag{2.34}$$

where μ_L is the Lagrange multiplier. This lead to the self-consistent Kohn-Sham equations [12] given as,

$$[-\frac{\hbar^2\nabla^2}{2m_e} + V_{ion}(\mathbf{r}) + V_H(\mathbf{r}) + V_{XC}(\mathbf{r})]\phi_i(\mathbf{r}) = \epsilon_i\phi_i(\mathbf{r}) \tag{2.35}$$

where $V_{XC}(\mathbf{r})$ is the functional derivative of $E_{XC}[n(\mathbf{r})]$ with respect to $n(\mathbf{r})$ and can be written as,

$$V_{XC}(\mathbf{r}) = \frac{\delta E_{XC}[n(\mathbf{r})]}{\delta n(\mathbf{r})} \tag{2.36}$$

Here one should be aware of the fact that only the ground state density calculated by solving the above mentioned single-particle Kohn-Sham equations has the physical meaning. The single particle wavefunctions here are solely mathematical functions with no physical meaning associated to them.

The Kohn-Sham energy depends on the electron density which itself depends on the eigen function of the Kohn-Sham Hamiltonian and so this self-consistent problem can be solved by iterative method. In this approach, with a trial density, Kohn-Sham Hamiltonian is constructed initially and the single particle Kohn-Sham equation is then solved for $\phi_i(\mathbf{r})$. These $\phi_i(\mathbf{r})$ then result in a modified electron density and therefore, an updated Kohn-Sham Hamiltonian. This process is continued until it converges to the correct electron density with a correct Kohn-Sham Hamiltonian. Once it is done, the exact ground state energy of the many electron system can be calculated as,

$$E_0 = \sum_i \epsilon_i - \frac{e^2}{2}\sum_{i,j(i\neq j)}\langle\phi_i\phi_j|\frac{1}{|\mathbf{r}-\mathbf{r}'|}|\phi_i\phi_j\rangle + E_{XC}[n(\mathbf{r})] - \int V_{XC}(\mathbf{r})n(\mathbf{r})d^3r \tag{2.37}$$

2.8 Spin Density Functional Theory (SDFT)

In discussions till now, we have not considered electron's spins which is absolute necessary when dealing with the magnetic properties of materials. We introduce electronic spin in density functional theory and the formalism is called spin density functional theory (SDFT) [14]. Details of this formalism are similar to the non-spin polarized case, only the main steps have been outlined here. In case of spin polarized systems, the Kohn-Sham equations are obtained separately for up-spin and down-spin orbitals. Defining σ as the spin index, we can write,

$$\left[-\frac{\hbar^2\nabla^2}{2m_e} + V^{\sigma}_{ion}(\mathbf{r}) + V^{\sigma_H}(\mathbf{r}) + V^{\sigma}_{XC}(\mathbf{r})\right]\phi^{\sigma}_i(\mathbf{r}) = \epsilon_i\phi^{\sigma}_i(\mathbf{r}) \tag{2.38}$$

The spin polarized electron density in this case is defined as,

$$n^{\sigma}(\mathbf{r}) = \sum_i \phi^{\sigma_i\star}(\mathbf{r})\phi^{\sigma}_i(\mathbf{r}). \tag{2.39}$$

which has a 2 $\times$ 2 matrix form given as,

$$\begin{pmatrix} n_{\uparrow\uparrow} & 0 \\ 0 & n_{\downarrow\downarrow} \end{pmatrix}$$

The orthogonality condition between up and down spin orbitals causes the off-diagonal terms to be zero. The exchange correlational functional which is also now spin polarized is given by,

$$V^{\sigma}_{XC}(\mathbf{r}) = \frac{\delta E_{XC}[n(\mathbf{r})]}{\delta n^{\sigma}\mathbf{r}}. \tag{2.40}$$

In SDFT, the total electron density $n(\mathbf{r})$ is obtained by adding the up-spin and the down-spin electrons as $n(\mathbf{r}) = n^{\uparrow}(\mathbf{r}) + n^{\downarrow}(\mathbf{r})$. This total electron density is often used instead of the spin densities n_{σ} and the local spin polarization can be obtained as $m(\mathbf{r}) = \mu_e[n^{\uparrow}(\mathbf{r}) - n^{\downarrow}(\mathbf{r})]$, where μ_e denotes the magnetic moment of an electron. Within this formalism one can now define an average exchange correlational functional is written as $\bar{V}_{exe}(\mathbf{r}) = \frac{\delta E_{XC}[n(\mathbf{r})]}{\delta n(\mathbf{r})}$ and an effective local magnetic field $B_{XC}(\mathbf{r}) = -\frac{\delta E_{XC}[m(\mathbf{r})]}{\delta m(\mathbf{r})}$. The Kohn-Sham equation for different spin densities now take the form,

$$[-\frac{\hbar^2\nabla^2}{2m_e} + V_{ion}(\mathbf{r}) + V_H(\mathbf{r}) + \bar{V}_{XC}[n(\mathbf{r})]] - \mu_e B_{XC}(\mathbf{r})]\phi_i^{\uparrow}(\mathbf{r}) = \epsilon_i\phi_i^{\uparrow}(\mathbf{r}) \quad (2.41)$$

$$[-\frac{\hbar^2\nabla^2}{2m_e} + V_{ion}(\mathbf{r}) + V_H(\mathbf{r}) + \bar{V}_{XC}[n(\mathbf{r})]] + \mu_e B_{XC}(\mathbf{r})]\phi_i^{\downarrow}(\mathbf{r}) = \epsilon_i\phi_i^{\downarrow}(\mathbf{r}) \quad (2.42)$$

From these equations, the total energy of a magnetic system can be obtained as,

$$E[n(\mathbf{r})] = \sum_{\sigma}\sum_{i}\epsilon_i^{\sigma} - \frac{e^2}{2}\int\int\frac{n(\mathbf{r})n(\mathbf{r'})}{|\mathbf{r}-\mathbf{r'}|}d\mathbf{r}d\mathbf{r'} + E_{XC}[n(\mathbf{r})] - \int V_{XC}[n(\mathbf{r})]n(\mathbf{r})d\mathbf{r} + \int B_{XC}(\mathbf{r})m(\mathbf{r})d\mathbf{r}$$

2.8.1 Density Functional Theory For Noncollinear Spin Systems

The collinear DFT discussed in the previous section assumes orientation of spins in a particular direction and can be generalized to obtain a noncollinear form in terms of full spin density matrix $n^{\sigma\sigma'}$ having non-zero off-diagonal elements [15]. The analogous single electron Kohn-Sham equations in this generalized formalism can be written as,

$$\sum_{\sigma'}\left[\left\{-\frac{\hbar^2\nabla^2}{2m_e} + V_H(\mathbf{r})\right\}\delta_{\sigma\sigma'} + V_{ion}^{\sigma\sigma'}(\mathbf{r}) + V_{XC}^{\sigma\sigma'}(\mathbf{r})\right]\phi_i^{\sigma'}(\mathbf{r}) = \epsilon_i\phi_i^{\sigma}(\mathbf{r}) \quad (2.43)$$

The exchange-correlation potential in it's matrix form have nonzero off-diagonal terms and the electronic density as well the spin polarization can be obtained by analogy to the previous case as,

$$n_e(\mathbf{r}) = Tr[n^{\sigma\sigma'}(\mathbf{r})] \quad (2.44)$$

$$\mathbf{m}(\mathbf{r}) = \mu_e\sum_{\alpha\beta}\rho_{\alpha\beta}(\mathbf{r})\sigma_{\alpha\beta} \quad (2.45)$$

respectively. The total density matrix takes the form,

$$[n(\mathbf{r})] = \frac{1}{2}[n_e(\mathbf{r})\mathbf{I} + \mathbf{m}(\mathbf{r}) \cdot \sigma] \tag{2.46}$$

where $\mathbf{I}$ and σ are unit matrix (2×2) and the Pauli matrices respectively. Similar to the previous treatment, we define an average exchange-correlation potential and an effective local magnetic field in accordance with new definitions which ultimately provide the following Kohn-Sham equation,

$$\sum_{\sigma'} \left[\left\{ -\frac{\hbar^2 \nabla^2}{2m_e} + V_H(\mathbf{r}) + \bar{V}_{XC}^{\sigma\sigma'}[n(\mathbf{r})] \right\} \delta_{\sigma\sigma'} + V_{ion}^{\sigma\sigma'}(\mathbf{r}) + \mu_e \mathbf{B}_{XC}(\mathbf{r}) \cdot \sigma_{\sigma\sigma'} \right] \phi_i^{\sigma'}(\mathbf{r}) = \epsilon_i \phi_i^{\sigma}(\mathbf{r})$$

The total energy of a noncollinear magnetic system can now be calculated as,

$$\begin{aligned} E[n(\mathbf{r})] = \sum_{\sigma} \sum_{i} \epsilon_i^{\sigma} - \frac{e^2}{2} \int \int \frac{n(\mathbf{r}) n(\mathbf{r}')}{|\mathbf{r} - \mathbf{r}'|} d\mathbf{r} d\mathbf{r}' + E_{XC}[n(\mathbf{r})] \\ - \int V_{XC}[n(\mathbf{r})] n(\mathbf{r}) d\mathbf{r} + \int \mathbf{B}_{XC}(\mathbf{r}) \cdot \mathbf{m}(\mathbf{r}) d\mathbf{r} \end{aligned} \tag{2.47}$$

2.9 Various Approximations For Exchange Correlation Functional

In Kohn-Sham formalism of density functional theory, the only unknown functional is the exchange-correlation potential (V_{XC}) part of which comes from the correlation term containing electrostatic interaction between electrons which is non-classical in nature and hence is the most complex quantity to evaluate in order to explain the physical properties of a many electron system. Efforts have been made towards determining accurate functionals under various approximations led to many different XC-functionals which will be discussed briefly in the coming sections.

2.9.1 Local Density Approximation (LDA)

The most popular and simplest of all is the local density approximation (LDA) [17] proposed by Kohn and Sham. In this approach, the system is considered to have a slowly varying spatial density $n(\mathbf{r})$ which in principle is related to the local density at each point of space and the exchange correlation functional takes the form,

$$E_{XC}^{LDA}[n(\mathbf{r})] = \int \epsilon_{XC}[n(\mathbf{r})]n(\mathbf{r})d\mathbf{r}, \tag{2.48}$$

where, $\epsilon_{XC}[n(\mathbf{r})]$ is the many body exchange-correlation energy per electron in an interacting homogeneous electron gas system of density $n(\mathbf{r})$ [16]. The exchange correlation potential and the ground state energy can be given as,

$$V_{XC}^{LDA}(\mathbf{r}) = \frac{\delta E_{XC}^{LDA}[n(\mathbf{r})]}{\delta n(\mathbf{r})} = \epsilon_{XC}[n(\mathbf{r})] + n(\mathbf{r})\frac{d\epsilon_{XC}[n(\mathbf{r})]}{dn(\mathbf{r})} \tag{2.49}$$

$$E_0^{LDA} = \sum_i \epsilon_i - \frac{e^2}{2}\int n(\mathbf{r})\frac{1}{|\mathbf{r}-\mathbf{r}'|}n(\mathbf{r}')d\mathbf{r}d\mathbf{r}' - \int n(\mathbf{r})\frac{d\epsilon_{XC}[n(\mathbf{r})]}{dn(\mathbf{r})}n(\mathbf{r})d\mathbf{r} \tag{2.50}$$

The above mentioned exchange correlation energy functional can be separated into exchange and correlation parts for non-polarized homogeneous electron gas system i.e.

$$\epsilon_{XC}[n(\mathbf{r})] = \epsilon_X[n(\mathbf{r})] + \epsilon_C[n(\mathbf{r})]. \tag{2.51}$$

This exchange part $\epsilon_X[n(\mathbf{r})]$ was derived analytically by Dirac and is known for a uniform electron gas [18]. In Dirac's derivation it has the form,

$$\epsilon_X[n(\mathbf{r})] = -\frac{3}{4}\left(\frac{3n(\mathbf{r})}{\pi}\right)^{\frac{1}{3}} \tag{2.52}$$

and hence the total exchange energy contribution can be written as,

$$E_X[n(\mathbf{r})] = \int \epsilon_X[n(\mathbf{r})]n(\mathbf{r})d\mathbf{r} \tag{2.53}$$

$$= \frac{3}{4}\left(\frac{3}{\pi}\right)^{\frac{1}{3}}\int [n(\mathbf{r})]^{\frac{4}{3}}d\mathbf{r} \tag{2.54}$$

However, the analytic expressions for the correlation energy (ϵ_C) in case of the homogeneous electron gas is only known in two limits of high and low electron densities. At high density and low density limit, the correlation energy density can be written as,

$$\epsilon_C^h = A_1 + A_2 r_s + (A_3 + A_4 r_s) ln(r_s) \tag{2.55}$$

$$\epsilon_C^l = \frac{1}{2}\left[\frac{a_1}{r_s} + \frac{a_2}{r_s^{3/2}} + ...\right] \tag{2.56}$$

respectively. r_s is the above expression is the radius of Wigner-Seitz cell [19] and is related to the electron density as,

$$\frac{4}{3}\pi r_s^3 = \frac{1}{n(\mathbf{r})} \tag{2.57}$$

Different analytical forms of correlation energy (ϵ_C) within various approaches led to several LDA correlation potential. Few popular examples are Vosko-Wilk-Nusair (VWN) [20], Perdew-Zunger (PZ81) [21], Cole-Perdew (CP) [22], Perdew-Wang (PW92) [23].

In the case of spin-polarized density functional theory, the exchange-correlation functional takes the form,

$$E_{XC}^{LSDA}[n^\uparrow, n^\downarrow] = \int n(\mathbf{r})\epsilon_{XC}[n^\uparrow(\mathbf{r}), n^\downarrow(\mathbf{r})]d\mathbf{r} \tag{2.58}$$

where $n(\mathbf{r}) = n^\uparrow(\mathbf{r}) + n^\downarrow(\mathbf{r})$. For the spin-polarized uniform electron gas of density $n^\sigma(\mathbf{r})$, the exchange energy within LSDA approximation can be given as,

$$E_X[n(\mathbf{r})] = \frac{3}{2}\left(\frac{3}{4\pi}\right)^{\frac{1}{3}} \sum_\sigma \int [n^\sigma(\mathbf{r})]^{\frac{4}{3}} d\mathbf{r} \tag{2.59}$$

2.9.2 Generalized Gradient Approximation (GGA)

Improvement of LSDA has been done by calculating the magnitude of the gradient of density (Δn^σ) in addition to the value of local density ($n(\mathbf{r})$) at each point in space. In this case, a semi local correction to the exchange part in terms of the gradient term is considered in order to partially take into account the inhomogeneity in density. The generalized gradient energy

functional is defined as,

$$E_{XC}^{GGA}[n^{\uparrow}, n^{\downarrow}] = \int \epsilon(n^{\uparrow}, n^{\downarrow}, |\nabla n^{\uparrow}|, |\nabla n^{\downarrow}|) n(\mathbf{r}) d\mathbf{r} \tag{2.60}$$

While performing the first principle numerical calculations, the GGA correlation functional is constructed by taking up to the second order term in the expansion of electron density function. In particular, GGA improves the treatment of core electrons which usually have higher density than the valence electrons and hence the total energy, barrier energy and difference in the structural energy calculations can be improved using GGA potentials. Some of the most popular GGA functionals are Perdew and Wang (PW91) [23], Becke-Lee-Yang-Par (B-LYP) [24] and Perdew, Burke and Enzerhof (PBE) [25] functionals.

Apart from the LDA and GGA functionals, approximations to the exchange-correlation energy have been made with a combination of orbital-dependent Hartree-Fock and an explicit density functional and are called hybrid functionals [26]. One example is the HSE functionals [28] named after J. Heyd, G. E. Scuseria, and M. Ernzerhof. These functionals are expected to be to be more accurate when compared to LDA and GGA functionals while studying the strongly correlated electron systems due to their large self-interaction correction [27] but are computationally expensive.

2.10 Plane Wave As Basis Function

In order to expand the single-particle wave-functions, an appropriate set of basis functions is required so that one can computationally solve the many electron Hamiltonian. With a plane wave basis set, the kinetic energy operator becomes diagonal and the matrix elements of the potential simply consist the Fourier transform of the atomic potential. While dealing with a crystalline solid, periodicity of the lattice allows us to use a Blöch [29, 33] like wavefunction which can be given as,

$$\phi_i(\mathbf{r}) = e^{i\mathbf{k}\cdot\mathbf{r}} u_i(\mathbf{r}) \tag{2.61}$$

where actually a plane wave is modified by a periodic function $u_n(\mathbf{r})$ which is periodic with respect to the lattice translation vector $\mathbf{R}_i$ to take into account the lattice periodicity *i.e.* $u_i(\mathbf{r}) = u_i(\mathbf{r} + \mathbf{R_i})$. This periodic function can be expressed as a linear combination of plane waves in the reciprocal space of the crystal as,

$$u_i(\mathbf{r}) = \sum_{\mathbf{G}} C_{i\mathbf{G}} e^{i\mathbf{G}\cdot\mathbf{r}} \tag{2.62}$$

where $\mathbf{G}$ and $C_{i\mathbf{G}}$ are reciprocal lattice vector of the crystal and the coefficients of the plane waves in the reciprocal space. Therefore the wavefunction can now be given as,

$$\phi_i = \sum_{\mathbf{G}} c_{i,\mathbf{G}+\mathbf{k}} e^{i(\mathbf{G}+\mathbf{k})\cdot\mathbf{r}} \tag{2.63}$$

The combination of these Kohn-Sham basis functions is the basic ingredient of plane wave method. An infinite basis set is required to solve a periodic potential problem which is practically impossible to implement. Therefore a cutoff point E_{cut} is fixed in the expansion of Eq.(2.63) so that, the plane-wave kinetic energy $E_{PW} = \frac{\hbar^2}{2m_e} |\mathbf{k} + \mathbf{G}|^2$ must be lower than the cutoff energy. The error introduced in this can simply be minimized by increasing E_{cut} till the total energy of the system converges.

Among many other approaches which differ in the choice of basis wave functions and schemes, some popular ones which consider all of the electrons in the system are LAPW (linearized augmented plane-wave) [30], FLAPW (full-potential LAPW) [31] and LMTO (linear muffin-tin orbital) [32] etc. There are few other approaches with tight binding method using linear combination of atomic orbitals (LCAO) type basis functions [33], orthogonalized plane wave (OPW) method [34], using plane waves orthogonal to core states as the basis set, augmented plane wave (APW) method [35] etc.

2.11 Pseudopotential Approach

In an atom, the electrons can be separated into two categories. The core electrons which are tightly bound to the nucleus having higher kinetic energies and the electrons of the outermost

shells, namely valence electrons having less kinetic energy than the core electrons. In this context one has to consider two important points. First point is, the physical and chemical properties of solids are usually determined by the valence electrons as they take part in bondings to form the solids. The second point is, in order to represent the core electrons with high kinetic energy a large number of plane-waves are required which will further increase the computational cost. Hence within a reasonably good approximation one can take out the core electrons states constructing a smoother potential for the electronic states. This is the basic idea behind the pseudopotential theory.

In this approximation, the quantum states which represent the core electrons and the valence electrons be $|\psi^c\rangle$ and $|\psi^v\rangle$ respectively. New set of single particle valence states $|\phi^v\rangle$ can be defined in such a way that,

$$|\psi^v\rangle = |\phi^v\rangle + \sum_c \alpha_c \psi^c(\mathbf{r}), \tag{2.64}$$

where α_c can be determined from the orthogonality condition $\langle\psi^c|\psi^v\rangle = \alpha_c\delta_{cv}$ which yields $\alpha_c = -\langle\psi^c|\phi^v\rangle$.

After operating the single particle Hamiltonian (H^{SP}) on these new set of wave functions, we get,

$$H^{SP}\left[|\phi^v\rangle + \sum_c \alpha_c|\psi^c(\mathbf{r})\right] = \epsilon^v\left[|\phi^v\rangle + \sum_c \alpha_c|\psi^c(\mathbf{r})\right] \tag{2.65}$$

Also, for single particle states of the core electrons one can write,

$$H^{SP}|\psi^c\rangle = \epsilon_c|\psi^c\rangle. \tag{2.66}$$

After putting the results obtained from Eq.2.66 into Eq. 2.65 and solving it, we arrive at,

$$\left[H^{SP} + \sum_c(\epsilon^v - \epsilon^c)|\psi^c\rangle\langle\psi^c|\right]|\phi^v\rangle \quad = \quad \epsilon^v|\phi^v\rangle \tag{2.67}$$

It is then clear from the above equation that the single particle Schrödinger equation is satisfied by the new set of states $|\phi^v\rangle$ with a modified potential which is called the pseudo-potential and

is given as,

$$V^{PS} = V^{SP} + \sum_c (\epsilon^v - \epsilon^c)|\psi^c\rangle\langle\psi^c|, \tag{2.68}$$

The corresponding single particle wave functions ($|\phi^v\rangle$) are called pseudo-wavefunctions. Since $\epsilon^v > \epsilon^c$, therefore the second term in the above expression represents a repulsive potential experienced by valence electrons due to the core electrons. The effective pseudo-potential does not contain the $1/r$ singularity due to the ion at the origin and hence is much smoother in practice. Fig.2.1 schematically illustrates the pseudo-potential approach. Beyond the core region i.e. above a cutoff radius, r_c pseudo-wavefunctions and pseudo-potentials are identical to the all electron wavefunctions and potential respectively while in the core region (within r_c), a weaker potential will be experienced by this new set of valence states.

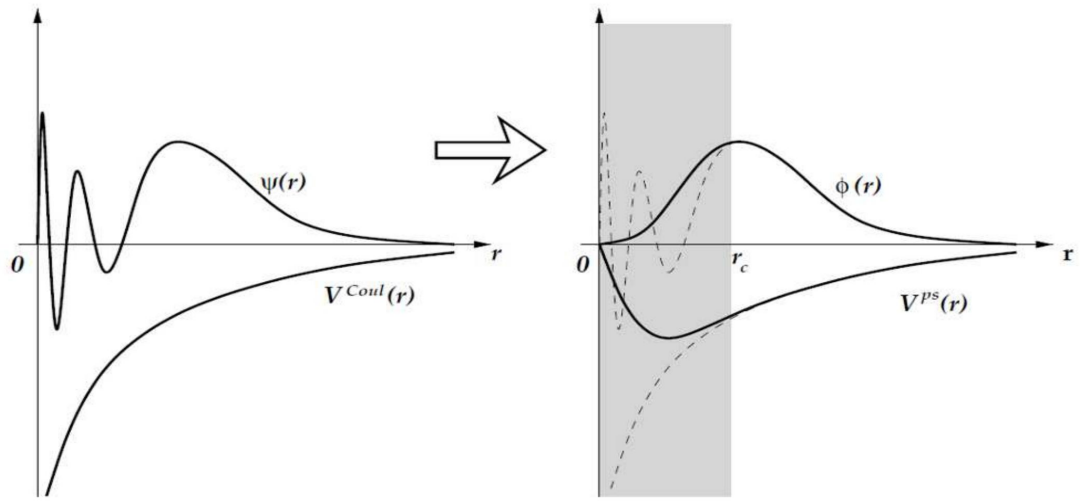

Figure 2.1: Schematic diagram of the Pseudopotential $V^{PS}(r)$ and pseudo-wavefunction $\phi(r)$. The left figure shows valence wave function $\psi(r)$ and Coulomb potential $V^{Coul}(r)$. In the right figure, r_c represents the cutoff radius beyond which the wavefunction and the potential are not affected.

One of the main aims to develop the pseudo-potentials is to construct the pseudo-wavefunctions smoother as much as possible and yet accurate. Efforts have been made towards generation of not only more accurate but also more efficient pseudo-potentials and a suitable example is norm-conserving pesodo potential technique first introduced by Hamann, Schlüter and Chiang. In this technique, the norm-conserving pseudo-wavefunctions are normalized and should preserve all the characteristics of valence electrons in an all electron calculations. This can be achieved

by setting the core radius around the outermost maximum of the all-electron wavefunction. The valence pseudo-wavefunctions will satisfy the orthonormal conditions as,

$$\langle \psi_i^{\sigma,PS} | \psi_j^{\sigma',PS} \rangle = \delta_{i,j}\delta_{\sigma,\sigma'} \tag{2.69}$$

Now, the single particle Schrödinger equations would take the form,

$$H^{\sigma,PS} | \psi_i^{\sigma,PS} \rangle = \epsilon_i | \psi_i^{\sigma,PS} \rangle \tag{2.70}$$

where, $H^{\sigma,PS}$ is the Kohn-Sham Hamiltonian with pseudo-potential approximation. Certain conditions are imposed during the formation of norm-conserving pseudo-potentials as suggested by HSC in it's formalism [36]. Single electron Schrödinger equations with pseudo-wavefunctions are only valid beyond a choosen core radius r_c. For each of the wave function, integrated charge inside the core satisfies the norm-conservation and logarithmic derivatives of all electron pseudo-wavefunctions should be continuous at r_c. Pseudo-potentials constructed with these restrictions are suitable for describing a well localized system (e.g. $3d$ and rare earth elements) but have problems describing the lighter elements (e.g. first row elements in periodic table). In a different approach [37] in which the norm-conserving constraint is relaxed and the pseudo-wavefunctions become smoother with an auxiliary function around each ion core that includes the rapidly varying part of the density and has the form $\phi = r\psi$. The advantage is that, it may be possible to construct smooth pseudo-wavefunction independently with a choosen cutoff radius much larger than that of previously discussed norm-conserving pseudo-potentials.

2.11.1 Projector Augmented Waves (PAWs) method

Projector augmented plane wave method [38] is another pseudo-potential technique developed by Blöch in order to eliminate some of the disadvantages of the ultrasoft potentials. In this technique, an all electron wave function is constructed, with which all integrals are calculated as a combination of smooth functions extending throughout space and contribution from the localized muffin tin orbitals. Hence the total wavefunction in this case is a combination of

valence state wavefunctions $\tilde{\psi}_i^v(\mathbf{r})$ and a linear transformation function relating the all-electron valence functions $\psi_j^v(\mathbf{r})$ to $\tilde{\psi}_i^v(\mathbf{r})$ which is given as,

$$\psi_j^v(\mathbf{r}) = \tilde{\psi}_j^v(\mathbf{r}) + \sum_i (|\phi_i\rangle - |\tilde{\phi}_i\rangle)\langle\tilde{p}_i|\tilde{\phi}_i\rangle \tag{2.71}$$

In the above equation, index i is for the atomic site $\mathbf{R}$, $|\tilde{p}_i\rangle$ are the projector functions for localized pseudo partial wave which satisfy the orthogonality condition, $\langle\tilde{p}_i|\tilde{\phi}_j\rangle = \delta_{i,j}$. Within this formalism, the all electron charge density can be derived from Eq.2.71 as,

$$n(\mathbf{r}) = \tilde{n}(\mathbf{r}) + n^1(\mathbf{r}) - \tilde{n}^1(\mathbf{r}), \tag{2.72}$$

where,

$$\tilde{n}(\mathbf{r}) = \sum_i f_i |\tilde{\psi}_i(\mathbf{r})|^2 \tag{2.73}$$

$$n^1(\mathbf{r}) = \sum_i f_i \sum_{j,k} \langle\tilde{\psi}_i|\tilde{p}_j\rangle \phi_j(\mathbf{r})\phi_k(\mathbf{r})\langle\tilde{p}_k|\tilde{\psi}_i\rangle \tag{2.74}$$

$$\tilde{n}^1(\mathbf{r}) = \sum_i f_i \sum_{j,k} \langle\tilde{\psi}_i|\tilde{p}_j\rangle \tilde{\phi}_j(\mathbf{r})\tilde{\phi}_k(\mathbf{r})\langle\tilde{p}_k|\tilde{\psi}_i\rangle \tag{2.75}$$

In the above expressions, f_i's represent the occupancies of the eigenstates $\tilde{\psi}_i$, $\tilde{n}(\mathbf{r})$ is the pseudo-charge density and is evaluated from the pseudo-wavefunctions with plane wave basis. $n^1(\mathbf{r})$ and $\tilde{n}^1(\mathbf{r})$ are the onsite charge densities localized within the augmented sphere around each atom. Total energy of the system when calculated from these charge densities can also be divided into three parts.

2.12 DFT Calculations : A Typical Flow Chart

Basic informations which are required to start a DFT calculation are the structural data and potentials of the all the constituent atoms. A guessed electron density using the linear combination of individual electron densities is formed first and then using this density in the Kohn-Sham Hamiltonian, it will be then diagonalized. There are two very popular diagonalization subroutines used here. There are the Block Davidson iteration method and residual minimization

method by direct inversion in the iterative subspace. Then system's total energy is calculated and checked for convergence. If the convergence criteria which is set by the user is not yet met, then a new electron density with slight changes in the old one is calculated and the Hamiltonian is again diagonalized. This process is repeated till the convergence criteria is achieved. Now here at this juncture one can opt for structural optimization in which force acting on each atom of the unit cell is calculated. If the convergence criteria for force has not been met then the individual atoms will be moved in the direction of force acting on them and the new electron density is obtained with these new coordinates. The Hamiltonian will again be diagonalized with this new electron density and this process will be repeated until the energy as well as the force convergence criteria is achieved. Thus using the variational principle, one arrives at the ground state single particle electron density in the end. This can now be used to calculate the density of states, band structure, magnetic stability of the ground state, optimized structure and numerous other ground state properties. The flow chart of a typical DFT calculation is shown in Fig. 2.2.

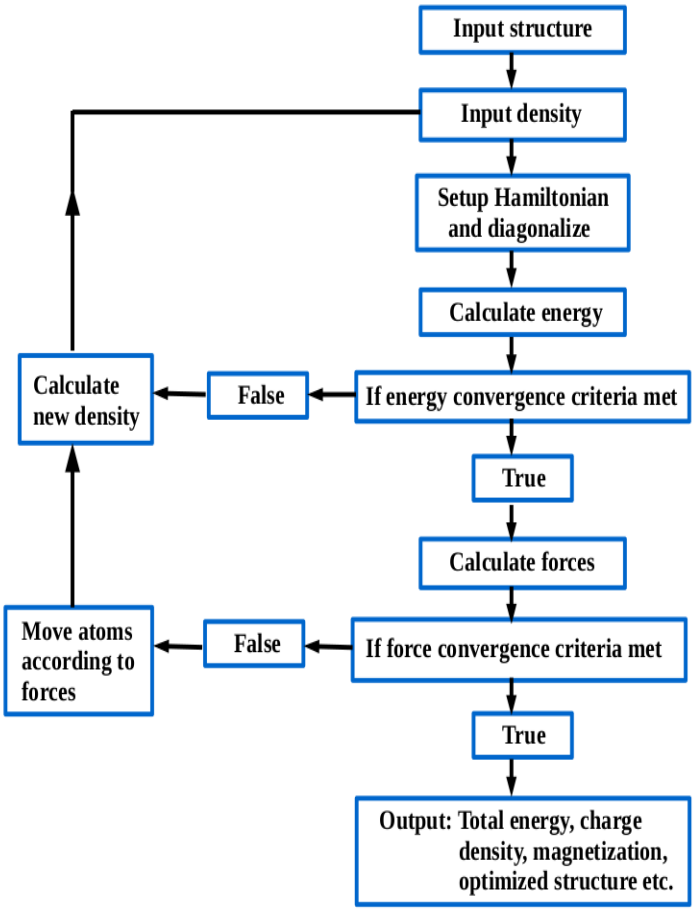

Figure 2.2: Flowchart of a typical DFT electronic structure calculation.

2.13 Tight Binding Approach

Tight binding method is the simplest way of calculating the band structures of solids and is an extension of Blöch's LCAO method [33]. Later in 1954, it was developed and parametrized in terms of Slater-Koster parameters for few simple lattice structures [39]. Within this approximation, the crystal wavefunctions are expanded with the basis set containing the atomic wavefunctions corresponding to orbitals which are assumed to be tightly bound to the atoms on the particular sites.

We first consider, a set of atomic wavefunctions $\phi_l(\mathbf{r} - \mathbf{t_i})$ within a primitive unit cell where $\phi_i(r)$ is an atomic state corresponding to the $i-th$ atom located at position t_i. Index l is used to represent the different type of orbitals (s, p, d etc.). The constructed basis states using these

atomic orbitals obey the Blöch's theorem for a periodic lattice and is so can be written as,

$$\Phi_{\mathbf{k},l,i}(\mathbf{r}) = \frac{1}{\sqrt{N}} \sum_{\mathbf{R'}} e^{i\mathbf{k}.\mathbf{R'}} \phi_l(\mathbf{r} - \mathbf{t_i} - \mathbf{R'}) \tag{2.76}$$

which is normalized by the total number of unit cells N and $\mathbf{R'}$ are translational vectors. The single particle eigen state using these basis functions can be written as,

$$\psi_k^n(\mathbf{r}) = \sum_{\mathbf{l,i}} \mathbf{c_{k,l,i}} \mathbf{\Phi_{k,l,i}}(\mathbf{r}) \tag{2.77}$$

where $c_{k,l,i}$ are evaluated from the condition that $\psi_k^n(\mathbf{r})$ are solutions to the single particle Schrödinger's equations and are orthonormal ($\langle \psi_{\mathbf{k}}^n(\mathbf{r}) | \psi_{\mathbf{k'}}^n(\mathbf{r}) \rangle = \delta(\mathbf{k} - \mathbf{k'})$), *i.e.*

$$H^{SP} \psi_k^n(\mathbf{r}) = \epsilon_{\mathbf{k}} \psi_{\mathbf{k}}^{\mathbf{n}}(\mathbf{r}), \tag{2.78}$$

$$\sum_{i,l} \left\{ \langle \Phi_{\mathbf{k},m,j} | H^{SP} | \Phi_{\mathbf{k},m,j} \rangle - \epsilon_{\mathbf{k}} \langle \Phi_{\mathbf{k},m,j} | \Phi_{\mathbf{k},m,j} \rangle \right\} c_{k,l,i}^n = 0 \tag{2.79}$$

In the above equation all the atomic orbitals within the primitive unit cell have been included. The integrals involved in this can be solved as,

$$\begin{aligned} \langle \Phi_{\mathbf{k},l,i} | \Phi_{\mathbf{k},l,i} \rangle &= \frac{1}{N} \sum_{\mathbf{R'},\mathbf{R''}} e^{i\mathbf{k}\cdot(\mathbf{R'}-\mathbf{R''})} \langle \phi_m(\mathbf{r} - \mathbf{t_j} - \mathbf{R''}) | \phi_l(\mathbf{r} - \mathbf{t_i} - \mathbf{R'}) \rangle \\ &= \frac{1}{N} \sum_{\mathbf{R},\mathbf{R'}} e^{i\mathbf{k}\cdot\mathbf{R}} \langle \phi_m(\mathbf{r} - \mathbf{t_j}) | \phi_l(\mathbf{r} - \mathbf{t_i} - \mathbf{R}) \rangle \\ &= \sum_{\mathbf{R}} e^{i\mathbf{k}\cdot\mathbf{R}} \langle \phi_m(\mathbf{r} - \mathbf{t_j}) | \phi_l(\mathbf{r} - \mathbf{t_i} - \mathbf{R}) \rangle \end{aligned} \tag{2.80}$$

The bracket term in the last expression is called the overlap integrals of the atomic orbitals on the neighboring sites. One can calculate the expectation value of the Hamiltonian with these basis states as,

$$\langle \Phi_{\mathbf{k},m,j} | H | \Phi_{\mathbf{k},l,i} \rangle = \sum_{\mathbf{R}} e^{i\mathbf{k}\cdot\mathbf{R}} \langle \phi_m(\mathbf{r} - \mathbf{t}_j) | H | \phi_l(\mathbf{r} - \mathbf{t}_i - \mathbf{R}) \rangle \tag{2.81}$$

The bracket term in the above expression is called Hamiltonian matrix elements between the atomic orbitals on the neighboring sites and orthogonality condition ($\langle\phi_m(\mathbf{r}-\mathbf{t}_j)|\phi_l(\mathbf{r}-\mathbf{t}_i-\mathbf{R})\rangle = \delta_{l,m}\delta_{i,j}\delta(\mathbf{R})$) can be used in order to arrive at a solution of it. In practice, these integrals are extremely difficult to calculate. However, for certain periodic lattices, these integrals can be parameterized in terms of Slater-Koster parameters and hence a much simplified Hamiltonian in $\mathbf{k}$ space takes the form,

$$H_{TB} = \sum_{k,l,\sigma} \epsilon_{l,\sigma} d^{\dagger}_{k,l,\sigma} d_{k,l,\sigma} + \sum_{n,\gamma} \sum_{k,l,m,\sigma} \left(t^{l,m}_{n,\gamma} d^{\dagger}_{k,l,\sigma} d_{k,m,\sigma} e^{-i\mathbf{k}\cdot\mathbf{R}^{l,m}_{n,\gamma}} + H.C. \right) \tag{2.82}$$

In this expression $d^{\dagger}_{k,l,\sigma}(d_{k,l,\sigma})$ creates (annihilates) an electron with spin σ in the l^{th} orbital. $\mathbf{R}^{l,m}_{n,\gamma}$ is the connecting vector of two orbitals l and m on the neighboring sites (n) with all the γ neighbors. The terms like ϵ and t in the above Hamiltonian are determined as fitting parameters to the *ab initio* band structure. The hopping interactions (t) here are parametrized in terms of Slater-Koster parameters and are evaluated by solving the above Hamiltonian at each $\mathbf{k}$ point in the Brillouin Zone of the considered system.

2.14 Maximally Localized Wannier Functions

In the tight binding method explained in the previous section, the atomic wavefunctions $\psi^n_k(\mathbf{r})$ in Eq.(1.82) are called Wannier functions (WF). These functions are different from atomistic tight binding wavefunctions in mainly two aspects. First point is that these Wannier functions can even be defined for a band which could not be well described under the tight binding approximation. However, in this case Wannier functions would not represent the bands originating from the atomistic level. Secondly, Wannier wavefunctions are the real space representation of the wavefunctions and the Wannier functions corresponding to two different sites are orthogonal in nature. There are many areas where the applications of Wannier functions are possible. For example, utility of Wannier functions in calculating transport properties of realistic systems is well known.

The WF $\psi^n_{\mathbf{R}}(\mathbf{r})$ at site $\mathbf{R}$ can be written in terms of Blöch's state Φ_{mk} as,

$$\psi^n_{\mathbf{R}}(\mathbf{r}) = \frac{V}{(2\pi)^3}\int_{BZ}\left[\sum_m U^{\mathbf{k}}_{mn}\Phi_{m\mathbf{k}}(\mathbf{r})\right]e^{-i\mathbf{k}\cdot\mathbf{R}}d\mathbf{k}, \tag{2.83}$$

where n/m is the band index and k is the crystal momentum index. In the above equation, V is volume of the unit cell and integration is over the whole Brillouin zone. $U^{(\mathbf{k})}$ is the unitary matrix which is used to mix the Blöch states at each $\mathbf{k}$ point in the Brillouin zone of the crystal and is not a unique one. The varying spatial extensions of the Wannier functions depend upon the choice of $U^{(\mathbf{k})}$ in the above expression. This non-uniqueness of $U^{(\mathbf{k})}$ arise from the fact that orbitals represented by Blöch states belong to a set of bands that are separated by energy gaps from each other but have degeneracies within themselves and thus at each $\mathbf{k}$ point there will be many unitary transformations possible within themselves. This makes uses of Wannier functions unsuitable in the case of real problems. A procedure to eliminate this arbitrariness was proposed by Marzari and Vanderbilt in Ref [41]. In this method, iteratively redefined transformations would lead to uniquely defined set of maximally-localized Wannier functions (MLWFs). This approach can be applied to a variety of problems starting from an isolated system to a periodic solid. For the entanglement band problem this approach was extended by Souza *et al.* in Ref [42].

The basic idea in this approach is based upon the minimization of a well defined real space spread (ω) of the WFs given by,

$$\omega = \sum_n \left[\langle\psi^n_{\mathbf{0}}(\mathbf{r})|r^2|\psi^n_{\mathbf{0}}(\mathbf{r})\rangle - |\langle\psi^n_{\mathbf{0}}(\mathbf{r})|\mathbf{r}|\psi^n_{\mathbf{0}}(\mathbf{r})\rangle|^2\right] \tag{2.84}$$

Hence, one can choose a unique $U^{(\mathbf{k})}_{mn}$ which will minimize the value of ω given a set Φ_{mk} of Blöch's states. Addition and subtraction of the off-diagonal terms $\tilde{\omega} = \sum_n \sum_{\mathbf{R}m\neq 0n} |\langle\psi^m_{\mathbf{R}}(\mathbf{r})|\mathbf{r}|\psi^n_{\mathbf{R}}(\mathbf{r})\rangle|^2$ in the above equation, we get,

$$\omega = \omega_I + \tilde{\omega} = \omega_I + \omega_D + \omega_{OD} \tag{2.85}$$

ω_I in the above expression is given by,

$$\omega_I = \sum_n \left[\langle \psi^n_{\mathbf{0}}(\mathbf{r}) | r^2 | \psi^n_{\mathbf{0}}(\mathbf{r}) \rangle - \sum_{\mathbf{R}m} |\langle \psi^m_{\mathbf{R}}(\mathbf{r}) | \mathbf{r} | \psi^n_{\mathbf{0}}(\mathbf{r}) \rangle|^2 \right] \tag{2.86}$$

This term is invariant under any arbitrary unitary transformation given in Eq.(1.89) of the Blöch's states and hence it would suffice to minimize only $\tilde{w}$ which is further decomposed into diagonal ω_D and off-diagonal ω_{OD} terms given as,

$$\omega_D = \sum_n \sum_{\mathbf{R}\neq 0} |\langle \psi^n_{\mathbf{R}}(\mathbf{r}) | \mathbf{r} | \psi^n_{\mathbf{0}}(\mathbf{r}) \rangle|^2 \tag{2.87}$$

$$\omega_{OD} = \sum_{m\neq n} \sum_{\mathbf{R}} |\langle \psi^m_{\mathbf{R}}(\mathbf{r}) | \mathbf{r} | \psi^n_{\mathbf{0}}(\mathbf{r}) \rangle|^2 \tag{2.88}$$

This procedure is sufficient to obtain the maximally localized Wannier functions for isolated bands as in the case of valence states in an insulator. In the case of entangled bands, difficulty appears in selection of N bands specially at those $\mathbf{k}$ points where hybridization of bands, that we are interested in, took place with other unnecessary bands. For entangled bands, disentanglement procedure given in Ref. [43] is used to obtain the maximally localized Wannier functions. In this procedure, first an energy window containing N number of bands, that we are interested in, is defined. Now at each given $\mathbf{k}$ point, the number of bands $\mathrm{N}_{(\mathbf{k})}$ inside this window is either equal or larger than N. Now performing unitary transformation within the Blöch states, present at each $\mathbf{k}$ point in this energy window, one can obtain a set of N Blöch states as,

$$|u_{n\mathbf{k}}\rangle = \sum_{m\in N^{(\mathbf{k})}} U^{(\mathbf{k})}_{mn} |u_{m\mathbf{k}}\rangle \tag{2.89}$$

$U^{(\mathbf{k})}$ in the above equation is a N $\times$ $\mathrm{N}_{(\mathbf{k})}$ matrix and after minimization of the spread ω_I, in the bigger energy window, set of $U^{(\mathbf{k})}$ are obtained. Then minimizing $\tilde{\omega}$ using the previously explained MV procedure we can obtain the maximally localized Wannier functions for this subspace of bands.

Due to mixing between spreads of the states in this procedure, it is possible that the bands in this subspace will not correspond to any of the originally selected bands. Hence, a second

smaller energy window was introduced and the states within this energy window are considered to be "frozen" *i.e.* are kept unchanged in the subspace. Thus in a given energy range, the exact basic properties will be preserved by this procedure.

Usually the bands lying in a small energy window close to the Fermi energy dominantly contribute to the electronic properties of solids. Such a minimal set of bands are the key idea behind many models such as Hubbard model in which one assumes spatially localized orbitals on different sites in a lattice. In the next section, we will discuss the Hubbard model within a model framework which we have used extensively in this thesis.

2.15 Model Framework For Hubbard Model

We have already discussed the basic aspects of Hubbard model in chapter 1 of this thesis. In this section we will explain the model framework for Hubbard model that we used within our calculations. In transition metal oxides, the important electron structure features near the Fermi energy arise mainly from effective transition metal-oxygen interactions. Hence when setting up a model in such cases, best choice of basis set would be the transition metal d orbitals along with the oxygen s and p orbitals. A multiband Hubbard Hamiltonian considering such a basis can be given as,

$$\begin{aligned} H = &\sum_{i,l,\sigma} \epsilon_d d^{\dagger}_{il\sigma} d_{il\sigma} + \sum_{i,l,\sigma} \epsilon_p p^{\dagger}_{il\sigma} p_{il\sigma} + \sum_{i,l,\sigma} \epsilon_s s^{\dagger}_{il\sigma} s_{il\sigma} \\ &- \sum_{i,j,l_1,l_2,\sigma} \left(t^{l_1 l_2}_{i,j,pd} d^{\dagger}_{il_1\sigma} p_{jl_2\sigma} + \mathbf{H.c.} \right) \\ &- \sum_{i,j,l_1,l_2,\sigma} \left(t^{l_1 l_2}_{i,j,pp} p^{\dagger}_{il_1\sigma} p_{jl_2\sigma} + \mathbf{H.c.} \right) \\ &- \sum_{i,j,l_1,l_2,\sigma} \left(t^{l_1 l_2}_{i,j,sd} d^{\dagger}_{il_1\sigma} s_{jl_2\sigma} + \mathbf{H.c.} \right) \\ &+ \sum_{\alpha\beta\gamma\delta,\sigma_1\sigma_2\sigma_3\sigma_4} U^{\alpha\beta\gamma\delta}_{dd} d^{\dagger}_{\alpha\sigma_1} d^{\dagger}_{\beta\sigma_2} d_{\gamma\sigma_3} d_{\delta\sigma_4} \end{aligned} \tag{2.90}$$

where $d^{\dagger}_{il\sigma}$ ($d_{il\sigma}$) creates (annihilates) an electron with spin σ in the lth d orbital on transition metal site in the ith unit cell while $p^{\dagger}_{il\sigma}$ ($p_{il\sigma}$)/$s^{\dagger}_{il\sigma}$ ($s_{il\sigma}$) creates (annihilates) an electron with

spin σ in the lth p/s orbital on oxygen atom in the ith unit cell. The s orbitals on oxygen are included as they simulate the effect of a crystal field splitting on the transition metal d states and were kept fixed deep inside the valence band to their approximate position [44, 45]. The hopping interactions in the above Hamiltonian are parametrized in terms of Slater-Koster parameters and are estimated by solving a tight binding model, explained in Section (1.13) of this chapter, considering transition metal d and oxygen p orbitals in the basis. The eigenvalues of the model are fitted to the *ab initio* nonmagnetic band structure of the transition metal oxide in the relevant energy window near the Fermi level and the parameters entering the tight binding Hamiltonian are determined by a least square error minimization procedure.

In our model, parameterization of the Coulomb matrix elements on the transition metal d states in terms of the Slater integrals F^0, F^2 and F^4 [46], which has the dimension of energy, help us taking care of the rotational invariant nature of the Coulomb interactions (independent of the magnetic quantum number m_l) and the multi-orbital effects. Atomistic Hartree-Fock calculations have been used to obtain the values of these parameters. However, F^0 was believed to be substantially screened because of the solid state effects present in the real materials. Values of F^2 and F^4 were obtained considering the respective ionic configuration of transition metal atoms in an oxide in these atomistic HF calculations and are also screened from their atomic values. The role of F^0 in our model is to obtain a suitable value of multiplet averaged Coulomb interaction strength (U) and F^2, F^4 were scaled so that they reproduce the expected intraatomic exchange interaction strength in a transition metal oxide. F^0 is related to U by the relation,

$$F^0 = U + \frac{2\eta}{63}(F^2 + F^4) \tag{2.91}$$

The factor η in the above expression is related to the Hund's exchange interaction strength as,

$$J = \eta\frac{F^2 + F^4}{14} \tag{2.92}$$

and has been introduced to account for the screening of the intraatomic exchange interaction strength. For example in the case of a $3d$ transition metal its value is ~ 0.8 eV while in the $4d$ and $5d$ cases, it may have the values of $\sim$ 0.3-0.4 eV and 0.1 eV respectively. In some of our

work, we have varied the values of U on the transition metal site to analyze its effect on the system. In such cases, one has to keep fix the charge transfer energy (Δ) of the system. In order to do this, one should choose the closest energetically efficient charge fluctuation between the oxygen p and transition metal d orbitals and define (Δ) as,

$$\Delta = E_f - E_i = (d^{n+1}\bar{L}) - d^n \tag{2.93}$$

The right hand side in the above expression will result in an expression containing the onsite energies for transition metal d, oxygen p and Coulomb interaction term U. For example in the case of $NaOsO_3$ (chapter 3), the above expression came out as $\Delta = \epsilon_d - \epsilon_p + 3U$ after considering charge fluctuation as $d^4\bar{L} - d^3$.

It is obviously difficult to solve the multiband Hubbard Hamiltonian given in Eq.(1.96) exactly and one needs an alternative method to solve it. We used the Hartree-Fock approximation to decouple the four Fermionic term such as $d^\dagger_{i\uparrow}d_{i\uparrow}d^\dagger_{i\downarrow}d_{i\downarrow}$ as,

$$\begin{aligned} d^\dagger_{i\uparrow}d_{i\uparrow}d^\dagger_{i\downarrow}d_{i\downarrow} = \langle d^\dagger_{i\uparrow}d_{i\uparrow}\rangle d^\dagger_{i\downarrow}d_{i\downarrow} + d^\dagger_{i\uparrow}d_{i\uparrow}\langle d^\dagger_{i\downarrow}d_{i\downarrow}\rangle - \langle d^\dagger_{i\uparrow}d_{i\downarrow}\rangle d^\dagger_{i\downarrow}d_{i\uparrow} - d^\dagger_{i\uparrow}d_{i\downarrow}\langle d^\dagger_{i\downarrow}d_{i\uparrow}\rangle \\ -\langle d^\dagger_{i\uparrow}d_{i\uparrow}\rangle\langle d^\dagger_{i\downarrow}d_{i\downarrow}\rangle + \langle d^\dagger_{i\uparrow}d_{i\downarrow}\rangle\langle d^\dagger_{i\downarrow}d_{i\uparrow}\rangle \end{aligned} \tag{2.94}$$

Following ansatz for the mean field expectation, values of the order parameters (quantities with $\langle\rangle$) have been considered within a spiral spin density wave with wave vector $\vec{q}$,

$$\begin{aligned} A^d_{ill}e^{i\vec{q}\cdot\vec{R}_i} &= \langle d^\dagger_{il\uparrow}d_{il\downarrow}\rangle \\ A^d_{il_1l_2}e^{i\vec{q}\cdot\vec{R}_i} &= \langle d^\dagger_{il_1\uparrow}d_{il_2\downarrow}\rangle = \langle d^\dagger_{il_2\uparrow}d_{il_1\downarrow}\rangle \\ \langle d^\dagger_{il\uparrow}d_{il\uparrow}\rangle &= \langle d^\dagger_{il\downarrow}d_{il\downarrow}\rangle = \frac{n^d_l}{2} \end{aligned} \tag{2.95}$$

In the $\vec{k}$-space, in terms of Fourier transform, the creation and the annihilation operators can be defined as,

$$d^{\dagger}_{\vec{k}l\sigma} = \sum_{\vec{k}} d^{\dagger}_{il\sigma} e^{i\vec{k}\cdot\vec{R}_i}$$

Using these definitions, one can then write the mean field Hamiltonian (H_{MF}) in the $\vec{k}$-space as

,

$$H_{MF} = \sum_{\vec{k}} (\Phi^{\dagger}_{\vec{k}\uparrow} \Phi^{\dagger}_{\vec{k}+\vec{q}\downarrow}) \begin{bmatrix} M_{\vec{k}} & A_{\vec{k}} \\ A_{\vec{k}\dagger} & M_{\vec{k}+\vec{q}} \end{bmatrix} \begin{bmatrix} \Phi_{\vec{k}\uparrow} \\ \Phi_{\vec{k}+\vec{q}\downarrow} \end{bmatrix} - (\text{constants from decoupling terms})$$

The $\Phi_{\vec{k}\uparrow}$ in the above expression is a row matrix with elements like $(d^{\dagger}_{\vec{k}l\uparrow})$ where l is the index run over the five transition metal d orbitals. Dimension of this matrix depends upon size of the system under consideration. As is clear from above that $M_{\vec{k}}$ and $M_{\vec{k}+\vec{q}}$ are the matrices corresponding to the Hamiltonian for the up and down spins where as $A_{\vec{k}}$ is obtained from the coupling between up and down spin states due to spin spiral ordering. Dimensions of $M_{\vec{k}}$ and $A_{\vec{k}}$ will again depend upon the system size. The constants in the above expression were came from decoupling terms like for example $\langle d^{\dagger}_{il\uparrow} d_{il\uparrow} \rangle \langle d^{\dagger}_{il\downarrow} d_{il\downarrow} \rangle$ term.

Standard numerical methods have been used to self-consistently diagonalized the above Hamiltonian and the ground state can be realized by minimizing the expectation value of this Hamiltonian with respect to the order parameters $\langle d^{\dagger}_{il\uparrow} d_{il\uparrow} \rangle$, $\langle d^{\dagger}_{il\downarrow} d_{il\downarrow} \rangle$ etc. used in the equation [47,48]. Tetrahedron method of integration was used over a 10 $\times$ 10 $\times$ 10 k-mesh to evaluate the total energy as well as the density of states. The magnetic phases within this Hamiltonian are calculated by minimization of energy with respect to the spiral SDW vector $\vec{q}$ in the self-consistent solutions and evaluating order parameter A^d. The value of A^d provide us the magnetic moment on the transition metal site.

Bibliography

[1] M. Born and J. R. Oppenheimer, *Zur Quantentheorie der Molekeln*, Ann. Physik **84**, 457(1927).

[2] D. R. Hartree, *The wave mechanics of an atom with non-Coulombic central field: Parts I, II, III.* Proc. Cambridge Phil. Soc. **24**, 89, 111, 426(1928).

[3] V. Fock, *Naherungsmethode zur Losung des quanten-mechanischen Mehrkorperprobleme*, Z. Phys. **61**, 126(1930).

[4] J. C. Slater, *The Theory of Complex Spectra*, Phys. Rev. **34**,1293(1929).

[5] A. Szabo and S. Ostlund, *Modern Quantum Chemistry: Introduction to Advanced Electronic Structure Theory*, Dover publications, (1996).

[6] J. A. Pople, M. Head-Gordon, and K. Raghavachari, J. Chem. Phys. **87**, 5968(1987).

[7] C. D. Sherrill, H. F. Schaefer III, *The Configuration Interaction Method: Advances in Highly Correlated Approaches*, Adv. Quant. Chem. **34**, 143(1999).

[8] L. H. Thomas, Proc. Camb. Phil. Soc **23**, 542 (1927).

[9] E. Fermi, Z. Phys. **48**, 73 (1928).

[10] J. C. Slater, Phys. Rev. **81**, 385 (1951).

[11] P. Hohenberg and W. Kohn, Phys. Rev. **136**, B864(1964).

[12] W. Kohn and L. J. Sham, Phys. Rev. **140**, A1133(1965).

[13] A. D. Becke, J. Chem. Phys. **98**, 5648 (1993); see also E. Kaxiras, *Atomic and Electronic Structure of Solids*, Cambridge University Press, UK,(2003).

[14] I. V. Solovyev, P. H. Dederichs and V. I. Anisimov, Phys. Rev. B **50**, 16861 (1994); A. B. Shick, A. I. Liechtenstein and W. E. Pickett, Phys. Rev. B **60**, 10763 (1999) ; S. L. Dudarev, G. A. Botton, S. Y. Savrasov, C. J. Humphreys and A. P. Sutton, Phys. Rev. B **57**, 1505 (1998).

[15] L. M. Sandratskii, J. Phys. Condens. Matter **3**, 8565 (1993); J. Phys. Condens. Matter **3**, 8587 (1993); D. Hobbs, G. Kresse and J. Hafner, Phys. Rev. B. **62**, 11556 (2000).

[16] D. M. Ceperley and B. J. Alder, Phys. Rev. Lett. **45**, 566 (1980).

[17] J. P. Perdew, E. R. McMullen and A. Zunger, Phys. Rev. A **23**, 2785(1981).

[18] P. A. M. Dirac, Proc. Cambridge Phil. Roy. Soc. **26**, 376(1930).

[19] E.Wigner and F. Seitz, Phys. Rev. **43**, 804 (1933); ibid, **46**, 509 (1934); E.Wigner, Phys. Rev. **46**, 1002 (1934); see also R. M. Dreizler and E. K. U. Gross, *Density Functional Theory*, Springer, New York (1990).

[20] S. H. Vosko, L. Wilk and M. Nusair, Can. J. Phys. **58**, 1200 (1980).

[21] J. P. Perdew and A. Zunger, Phys. Rev. B **23**, 5048 (1981).

[22] L. A. Cole and J. P. Perdew, Phys. Rev. A **25**, 1265 (1982).

[23] J. P. Perdew and Y. Wang, Phys. Rev. B **45**, 13244(1992).

[24] A. D. Becke, Phys. Rev. A **38**, 3098(1988); C. Lee, W. Yang, R. G. Parr, Phys Rev. B **37**, 785(1988); A. D. Becke, J. Chem. Phys. **96** 2155(1992).

[25] J. P. Perdew, K. Burke, and M. Ernzerhof, Phys. Rev. Lett. **77**, 3865(1996).

[26] A. D. Becke, J. Chem. Phys. **98**, 1372 (1993); A. V. Krukau, O. A. Vydrov, A. F. Izmaylov, and G. E. Scuseria, J. Chem. Phys. **125**, 224106 (2006).

[27] C. Franchini, V. Bayer, R. Podloucky, J. Paier and G. Kresse, Phys. Rev. B **72**, 045132 (2005); C.Franchini, R. Podloucky, J. Paier, M. Marsman, and G. Kresse, Phys. Rev. B **75**, 195128 (2007).

[28] J. Heyd, G. E. Scuseria, and M. Ernzerhof, J. Chem. Phys. **118**, 8207(2003).

[29] N. W. Ashcroft and N. D. Mermin, *Solid state Physics*, Brooks/Cole Thomson Learning Inc., (1976); C. Kittel, Introduction to Solid State Physics, JohnWiley and Sons, Inc., seventh edition, (1996).

[30] P. Blaha, K. Schwartz, G. K. H. Madsen, D. Kvasnicka and J. Luitz; *An Augmented PlaneWave + Local Orbitals Programfor calculating crystal properties* (K. Schwarz, Techn. UniversityWien, Austria, 2001).

[31] S. Blügel and G. Bihlmayer, *Full-potential linearized augmented plane-wave method, Computational Nanoscience: Do It Yourself !*, J. Grotendorst, S. Blügel, D. Marx (Eds.), John von Neumann Institute for Computing, Jülich, NIC Series, Vol. **31**, ISBN 3-00-017350-1, pp. 85-129 (2006).

[32] O. Kaoru and Y. K. Esfarjani, (1999). Computational Materials Science, Springer, p. 52 (1999); L. Vitos, *Computational Quantum Mechanics for Materials Engineers: The EMTO Method and Applications*, Springer-Verlag, p. 7 (2007).

[33] F. Blöch, Z. Physik **52**, 555 (1928).

[34] W. C. Herring, Phys. Rev. **57**, 1169 (1940); W. C. Herring and A. G. Hill, Phys. Rev. **58**, 132 (1940).

[35] T. L. Loucks, *Augmented Plane Wave Methods*, (Benjamin, New York, 1967).

[36] D. R. Hamann, M. Schluter, and C. Chiang, Phys. Rev. Lett. **43**, 1494(1979).

[37] D. Vanderbilt, Phys. Rev. B **41**, 7892(1985).

[38] P. E. Blöchl, Phys. Rev. B **50**, 17953 (1994).

[39] J. C. Slater and G. F. Koster, Phys. Rev. **94**, 1498 (1954).

[40] Walter A. Harrison, *Electronic Structure and Properties of Solids*, (Dover, 1989).

[41] N. Marzari and D. Vanderbilt, Phys. Rev. B **56**, 12847 (1997).

[42] I. Souza, N. Marzari and D. Vanderbilt, Phys. Rev. B **65**, 035109 (2001).

[43] I. Souza, N. Marzari and D.Vanderbilt, Phys. Rev. B **65**, 035109 (2002).

[44] L. F. Mattheiss, Phys. Rev. B, **2**, 3918 (1970).

[45] Priya Mahadevan, N. Shanthi and D. D. Sarma, Phys. Rev. B, **54** 11199 (1996).

[46] J. S. Griffith, *The Theory of Transition-Metal Ions*, (Cambridge University Press, Cambridge) (1961).

[47] Seva Nimkar, D. D. Sarma, H. R. Krishnamurthy and S. Ramasesha, Phys. Rev. B, **48**, 7355 (1993).

[48] Priya Mahadevan, K. Sheshadri, D. D. Sarma, H. R. Krishnamurthy and Rahul Pandit, Phys. Rev. B, **55**, 9203 (1997).

Chapter 3

Doping an antiferromagnetic insulator : A route to an antiferromagnetic metallic phase

3.1 Introduction

Usually antiferromagnetism comes hand in hand with an insulating state while ferromagnetism is accompanied by metallicity. There are very few examples of AFM metals and it is this aspect that makes the search for such systems interesting. Among the elemental metals, Cr is an example, though it has a complex AFM structure and the microscopic origin leading to this uncommon ground state is believed to be fermi surface nesting [1, 2]. Considering the transition metal compounds, where the magnetic interactions are usually superexchange in nature, there are few examples among the pnictides [3, 4] and the oxides [5, 6]. Among the pnictides, the origin is believed to be fermi surface nesting, though several alternate views have also emerged [7]. These aspects make the prospect of identifying a route to AFM metals important from a fundamental point of view.

Increasingly in recent times, AFM metals have been investigated for possible applications in spintronics [8], as spin injectors [9] or electrodes of an anisotropic magnetoresistance device [10, 11]. In view of the paucity of such AFM metallic materials among the transition metal

compounds, we explore here the design principle of doping carriers into an AFM insulator as a route to obtaining AFM metals. The ground state of the single band Hubbard model [12] at half filling is an AFM insulator above a critical value of U though in some models with extended hopping one has an AFM metallic phase even at half-filling [13, 14]. Examining the phase diagram of the former case as a function of doping, one finds that Hartree-Fock results indicate that in the small U regime one has an AFM metallic phase stabilized for low doping [15–18]. As U is increased, the doping concentration up to which one has an AFM metallic phase decreases and a FM metallic phase is stabilized. This has been understood as a competition between the kinetic energy gain from the itinerant electron which favors a FM state and the superexchange energy associated with the localized electron which favors an AFM ground state. This has a doping as well as U dependence with the widest stability for the AFM metallic phase found at intermediate values of U/t where t is the hopping interaction strength. The doping window for which the AFM metallic phase is stable decreases with decreasing U/t with a transition into a paramagnetic metallic regime. The large U/t limit is found to be consistent with the Nagaoka theorem leading to a ferromagnetic metallic state [19, 20].

The antiferromagnetic metallic state has been explored within a multiband Hubbard model in the context of the pnictides. At the half-filled limit it has been seen to exist, and the understanding is that Coulomb interactions are not large enough to open up a gap. This has been used to explain the presence of this phase in several pnictides [21, 22]. Examining the magnetic ground states at other integral fillings of the multiband Hubbard model, it has been seen [23] that antiferromagnetic phases are stabilised with more ferromagnetic neighbors such as C-type and then E-type for some numbers within a five band Hubbard model. These phases are found to be metallic for intermediate values of U as well as exist beyond the integral filling limit [24]. Most other studies using a multiband Hubbard model have focused on understanding what stabilizes the ferromagnetic state that one usually finds when one moves away from half-filling. Among the $3d$ transition metal oxides which have been extensively studied, one finds only ferromagnetic metallic phases.

Considering the example of $NaOsO_3$, the system is found to be an AFM insulator with a magnetic ordering temperature of 410 K [25, 26]. In an earlier work [27], we have reported *ab-initio* and model Hamiltonian calculations for the parent compound $NaOsO_3$ in order to understand its

high ordering temperature, and the implications of the results on other $5d$ transition metal oxides. It should be noted that only *ab-initio* calculations were reported for electron doped $NaOsO_3$ and an antiferromagnetic metallic ground state was found. However, such an ab-initio approach, with all energetics evaluated in a first-principle manner for the specific compound alone, cannot determine that the antiferromagnetic metallic phase would be a generic feature and should be expected for all systems in which one is doping electrons into a half filled t_{2g} band. The present calculations based on a model Hamiltonian approach in contrast to an *ab-initio* one, take parameters relevant for $3d$ transition metal oxides and $5d$ transition metal oxides to establish that there is only one regime in which the antiferromagnetic metallic phase is stable, ascertaining the fact that an antiferromagnetic metallic phase is **not** a generic feature of such doped systems.

Earlier calculations for the phase diagram of the doped Hubbard model considering a single orbital at the transition metal site found an antiferromagnetic metallic phase at intermediate values of U/t while in the large U/t limit they had a ferromagnetic metallic phase. In our calculations, carried out for 1.25 electrons per transition metal site (25% electron doping), we find similar trends at the one band limit, though the AFM metallic phase is found to be only weakly stabilized at the doping concentrations that we are studying. Considering the degeneracy of the d orbitals at the transition metal site, and parameters relevant for a $5d$ transition metal oxide, we find an AFM metal to be strongly stabilized for small U. For larger values of U, in contrast to the single band results which find a FM metallic phase, we find a charge ordered ground state with a non-vanishing moment. Interestingly within the same model, if we consider parameters relevant for a typical $3d$ transition metal oxide, one finds that the large Hund's coupling associated with this limit results in a FM metallic phase in the small U limit at a doping concentration of 25%. At a smaller doping of 12.5%, we find no ferromagnetic metallic phase. In the large U regime, a charge ordered insulating phase is stabilized similar to the case of the $5d$ oxide. The large U limit of the multiband Hubbard model does not give us the ferromagnetic metallic state that we find for the one band case.

3.2 Methodology

In order to understand the stability of different magnetic phases we set up a multiband Hubbard-like Hamiltonian considering the $NaOsO_3$ lattice. The basis consists of d orbitals on Os and s, p orbitals on oxygen atoms. The Hamiltonian is given by

$$\begin{aligned} H = & \sum_{i,l,\sigma} \epsilon_d d^{\dagger}_{il\sigma} d_{il\sigma} + \sum_{i,l,\sigma} \epsilon_p p^{\dagger}_{il\sigma} p_{il\sigma} + \sum_{i,l,\sigma} \epsilon_s s^{\dagger}_{il\sigma} s_{il\sigma} \\ & - \sum_{i,j,l_1,l_2,\sigma} \left(t^{l_1 l_2}_{i,j,pd} d^{\dagger}_{il_1\sigma} p_{jl_2\sigma} + \mathbf{H.c.} \right) \\ & - \sum_{i,j,l_1,l_2,\sigma} \left(t^{l_1 l_2}_{i,j,pp} p^{\dagger}_{il_1\sigma} p_{jl_2\sigma} + \mathbf{H.c.} \right) \\ & - \sum_{i,j,l_1,l_2,\sigma} \left(t^{l_1 l_2}_{i,j,sd} d^{\dagger}_{il_1\sigma} s_{jl_2\sigma} + \mathbf{H.c.} \right) \\ & + \sum_{\alpha\beta\gamma\delta,\sigma_1\sigma_2\sigma_3\sigma_4} U^{\alpha\beta\gamma\delta}_{dd} d^{\dagger}_{\alpha\sigma_1} d^{\dagger}_{\beta\sigma_2} d_{\gamma\sigma_3} d_{\delta\sigma_4} \end{aligned}$$

where $d^{\dagger}_{il\sigma}$ ($d_{il\sigma}$) creates (annihilates) an electron with spin σ in the lth d orbital on transition metal site in the ith unit cell while $p^{\dagger}_{il\sigma}$ ($p_{il\sigma}$)/$s^{\dagger}_{il\sigma}$ ($s_{il\sigma}$) creates (annihilates) an electron with spin σ in the lth p/s orbital on oxygen atom in the ith unit cell. The s orbitals on oxygen are included as they simulate the effect of a crystal field splitting on the Os d states and were kept fixed at -20 eV deep inside the valence band. This represents their approximate position inside the valence band. In a distorted perovskite, the t_{2g} states are not pure d_{xy}, d_{yz} and d_{xz} orbitals but have some admixture of $d_{x^2-y^2}$ and $d_{3z^2-r^2}$. Consequently the introduction of different diagonal energies for d_{xy}, d_{yz}, d_{xz} compared to $d_{x^2-y^2}$ and $d_{3z^2-r^2}$ orbitals to simulate the crystal field splitting cannot be done. An alternate way that has been used in the past [31, 34] is to introduce s orbitals on oxygen which interact only with the e_g orbitals on the Os site. The parameters in the tight binding part of the Hamiltonian were determined by fitting the $ab-initio$ band structure for $NaOsO_3$. The best fit Slater-Koster parameters [30] we got from this fitting are $sd\sigma$= -3.65 eV, $pd\sigma$= -3.75 eV , $pd\pi$= 1.80 eV, $pp\sigma$= 0.7 eV, $pp\pi$= -0.15 eV and $\epsilon_d - \epsilon_p = 0.8$ eV and were used in the earlier work [27] also. The charge transfer energy defined as $\Delta = \epsilon_d - \epsilon_p + 3U$ was kept fixed at 2 eV and a small intra-atomic Hund´s exchange interaction strength (J_h) of 0.1 eV was used. The complete multiplet interactions on the d orbitals on Os

were considered. These were parameterized in terms of the Slater Condon integrals [32], with the values of the Slater integrals F^2 and F^4 set at a fixed percentage of their atomic Hartree Fock values to give the desired value of the intra atomic exchange interaction strength J_h ($=\frac{F^2+F^4}{14}$). The multiplet averaged U was used to define the value of F^0. A mean field decoupling scheme was used to reduce the four fermion terms in the Hamiltonian to two-fermion terms which were then solved for self-consistently [14, 29]. Further details of the calculational approach may be found in Ref$\sim$ [28]. To study the limit corresponding to a $3d$ transition metal oxide, the hopping interactions strength used were -1.88 ($pd\sigma$) and 0.90 ($pd\pi$) which are typical values for a $3d$ transition metal oxide [28, 34]. Additionally a large value of the intra atomic exchange interaction strength (J_h) of 0.8 eV was used. These parameters for a $3d$ transition metal oxide are consistent with earlier estimates for a $3d$ transition metal atom in their oxides [33]. The phase diagrams were calculated at several doping concentrations as indicated in the text. In order to probe the role of degeneracy on the phase diagram, we considered a lattice containing only the transition metal atoms with just one orbital per site and examined the phase diagram for 25% electron doping. The hopping interaction strength was chosen in this case to give us the same bandwidth as the $5d$ oxides. Additionally an onsite Coulomb interaction strength was used. In each case, the total energies of various collinear as well as noncollinear configurations, especially near the phase boundaries, were calculated to evaluate the phase diagram as a function of U.

3.3 Results and Discussion

We have first examined the electronic structure and ensuing magnetic ground state favored when electrons are doped into a $5d$ transition metal oxide. In the undoped limit each transition metal atom had 3 electrons occupying the t_{2g} orbitals. In an earlier work we had argued that the large $p-d$ interaction strength of a $5d$ transition metal oxide as well as the small intra atomic exchange interaction at this limit, lead to a large superexchange coupling between spins on neighboring transition metal atoms. This we had argued would lead to very high magnetic ordering temperatures in these systems and $NaOsO_3$ [27] is an example of a system with this

mechanism at work. The immediate question which followed was whether this exchange splitting and magnetic moment would survive upon doping.

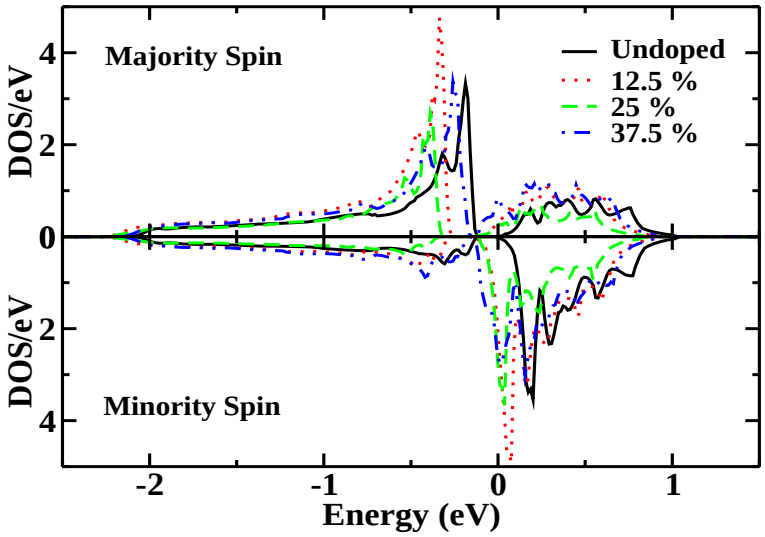

Figure 3.1: Spin projected Os-d partial density of states with t_{2g} symmetry for G-AFM metallic state at U=1 eV for different doping concentrations as well as for undoped case are plotted. The zero of energy is the Fermi energy.

In Fig. 3.1 we have plotted the Os d partial density of states with t_{2g} symmetry at a single Os site. The majority spin contribution is shown in the upper panel, while the minority spin contribution is shown in the lower panel of the figure. The results for the undoped case are shown along with those for the doped cases. The exchange splitting is found to survive even upto a doping of 37.5%. While a moment of $3\mu_B$ is expected at the ionic limit for the undoped case, one finds a reduction of the moment to $\sim 1\mu_B$. Only a part of the moment reduction is contributed by the admixture with oxygen p states. A significant portion of the moment reduction emerges from the strongly itinerant limit one is in. This is shown schematically in Fig. 3.2.

The onset of magnetic moment formation is expected to result in a shift in the density of states in majority spin channel deeper into the valence band and a similar shift in the density of states in the minority spin channel to higher energies (Fig. 3.2(a)). However, what one finds is shown in Fig.3.2(b) where in the same energy window that the majority spin states contribute, one finds the minority spin states also contributing, though with reduced weight. This emerges from the

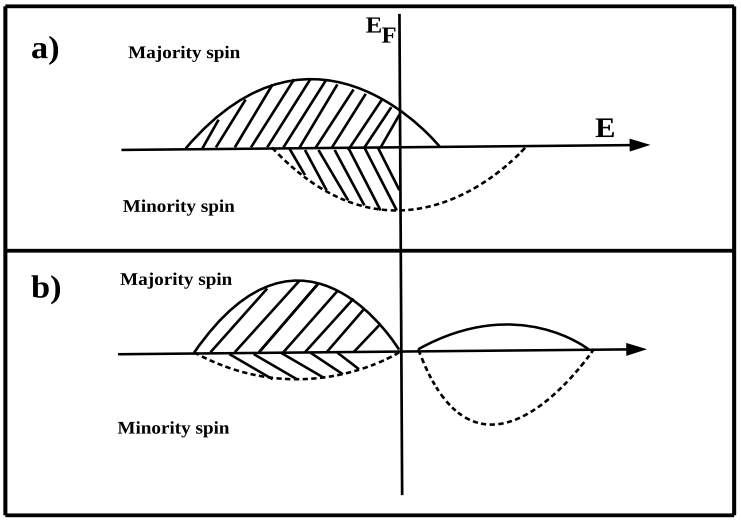

Figure 3.2: Schematic to show the formation of a magnetic moment that is (a) expected within Stoner picture, (b) what is found for $NaOsO_3$.

superexchange interactions between the neighboring transition metal atoms and is representative of the strongly itinerant limit that one is in.

Examining the weight of the minority spin states in the energy window contributed by the occupied majority spin states in Fig. 3.1 for the undoped case, one finds that there are ~ 0.48 electrons. A similar analysis of the states dominantly contributed by the minority spin states which are unoccupied reveals that there are 0.45 electrons. This results in a moment reduction of $0.93\mu_B$. With doping one finds that the doped electron occupies the minority spin t_{2g} states and this results in a decrease in the exchange splitting. However, various features in the density of states, surprisingly remain similar as discussed earlier in Ref. [27].

We went on to examine the stability of various phases with doping for the $5d$ transition metal oxide. In Fig 3.3 we have plotted the stability of the lowest energy phase with respect to the closest energy competing phase. This has been calculated for different concentrations as a function of U_{eff} which is defined as U-J_h. For small U we find that a G-type antiferromagnetic metallic phase is stabilized, while for large U one finds a charge ordered insulator. In order to understand the basic energetics that result in these states being stabilized, we examined the density of states in different U limits. In the low U limit, we have the doped electron occupying the minority spin t_{2g} states and the system is metallic. The majority spin t_{2g} states at each site are completely filled and they would like to favor a totally antiferromagnetic arrangement.

As the energy gain from the superexchange pathway arising from the majority spin t_{2g} states is substantial, a G-type antiferromagnetic arrangement wins over a ferromagnetic arrangement which allows a delocalization pathway for only the doped electron.

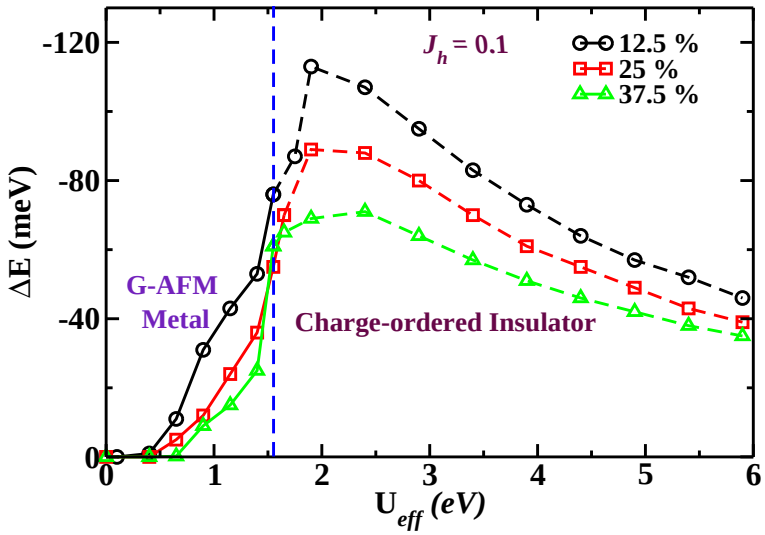

Figure 3.3: Relative stability ΔE calculated for different concentrations as the difference in energy between ground state and the closest competing state as a function of $U_{eff}(= U - J)$ for the multiband case using parameters relevant for a $5d$ oxide. Dashed line at U_{eff}=1.85 eV represents the phase boundary between the metallic (black line) and insulating regime (red line).The CO-insulating state has a magnetic moment of 0.8 μ_B at one of the transition metal sites. The nature of the ground state in each regime has been indicated.

The significant admixture of the minority spin states in the energy window that the majority spin states contribute and vice-versa as shown schematically in Fig. 2(b) allows for the energy gain via delocalization of the doped electron also. As U is increased, the doped electrons are found to be localized at one or more Os sites and a charge ordered insulating state is stabilized. In this insulating state, the antiferromagnetic arrangement of the majority spin t_{2g} states leads to cancellation of the moments from those states. However, the system has a finite moment which is associated with the minority spin t_{2g} states which holds one electron. The large U limit does not give us the ferromagnetic metallic state which is expected at the single band limit (Nagaoka ferromagnetism).

The energy stability of the ground state configuration with respect to the closest lying configuration (Fig. 3) as a function of U_{eff} follows the trend expected based on what is expected from superexchange arguments. The variation as a function of concentration has also been shown.

In each case we find an increase in stability as U_{eff} is increased, it goes through a maximum at a $U_{eff} \sim 2$ eV and then begins to decrease. This non-monotonic variation in the stability could be understood in terms of variation in the superexchange interaction strength that we had pointed out earlier in the context of the undoped $4d$ and $5d$ transition metal oxides [28]. In the low U regime, the hopping interaction strength is large compared to U. Therefore, the latter can be treated as a perturbation and one finds that the energy stability varies linearly with U. In the large U regime, the hopping may be treated as a perturbation and one finds that the energy stability varies as 1/U. Hence one has a peak in the stability at some intermediate value of U.

As the concentration is increased from 12.5 % to 25% and then to 37.5%, one finds a decrease in the stability in both the antiferromagnetic metallic region as well as the charge ordered insulator regime. This decrease can be traced back to the decrease in the gain from superexchange as the number of carriers in the minority spin channel is increased. A periodic super cell that we use in our calculations allows us to examine only doping concentrations commensurate with the lattice. As the presence of various phases remains unaltered, we believe that these phases should exist at other intermediate concentrations not probed by us in our calculations. For a truly incommensurate doping, the system will have to adopt one of the two solutions, namely a homogeneous ground state that may be metallic or even superconducting or an inhomogeneous phase, where electronic phase separation drives the system into some undoped parts and some parts with a commensurate doping with charge-ordering. Either of these two scenarios is well beyond the scope of the present study that can only address commensurate doping levels, like in any other investigation involving periodic systems.

Here one can argue that the spin-orbit interactions present in the case of a $5d$ transition metal oxide may lead to an effective band narrowing due to the splitting of J states, thereby favoring the tendency to the formation of an insulating state. This can significantly change the low U_{eff} region of the phase diagram. However, in an earlier study [27], within the *ab initio* framework, no significant change was found in the properties when spin-orbit interactions were included and the metallic state does survive quite robustly even in the presence of spin-orbit coupling. Based upon this finding, spin-orbit interaction effects were not considered in our results presented in this study.

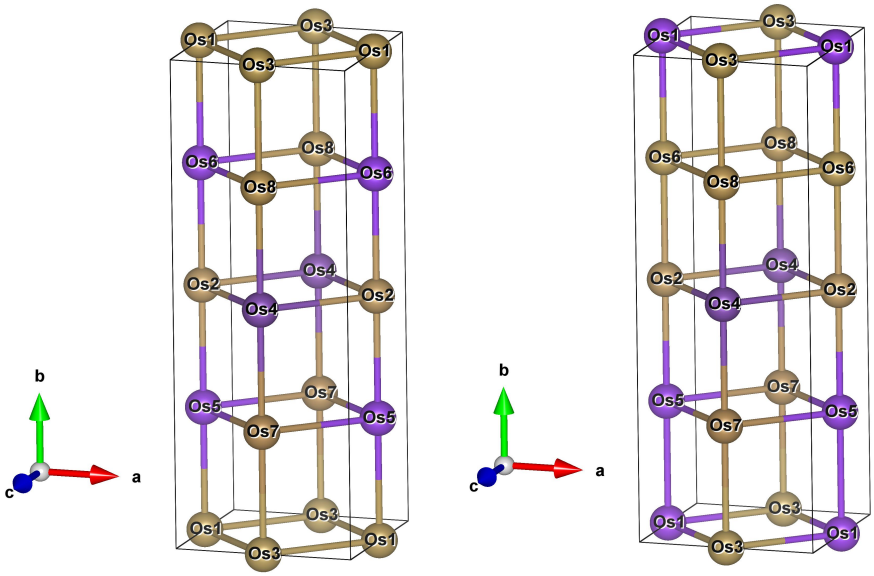

Figure 3.4: In the case of 37.5 % doping, the two closest competing configurations are shown. The configuration shown in panel (a) has been obtained as the ground state in the charge ordered region of the phase diagram while the next competing configuration is shown in panel (b). Blue balls representing the transition metal sites on which doped electrons are localized.

It is important to note here that doping three electrons into a unit cell of eight transition metals is effectively 37.5 % electron doping. There are many possible configurations in which these three electrons can localize onto separate transition metal atoms giving rise to charge ordering in the large U_{eff} region of the phase diagram. We show two of such configurations in which the first one in panel (a) of Fig 3.4 is the ground state while the other one in panel (b) is the next competing configuration. As is clear that in the ground state configuration, charge ordered atoms are arranged in a checker board pattern in all the three directions with each plane having one extra doped electron. This is obvious that for charge ordered state with antiferromagnetic arrangement of background spins, this would be the most stable configuration because of the minimization of Coulomb repulsion. In the panel (b) of Fig. 3.4, the next competing configuration shown has a ferromagnetic hopping pathways available via the nearest neighbor transition metal atom along the y-direction leading to reduction in the stability of antiferromagnetic state.

The next limit we go on to examine is that of the $3d$ transition metal oxides at the same doping concentrations. As the typical values of the intra atomic Hund's exchange is larger for the $3d$ transition metal oxides, we use a J_h of 0.8 eV for these calculations. The calculations were performed for various magnetic configurations and the difference in energy between the G-AFM

configuration with respect to the ferromagnetic configuration is determined. In contrast to the case of $5d$ transition metal oxides, we find that at this limit we have the majority spin t_{2g} and e_g levels first and then the minority spin levels, with the levels of t_{2g} symmetry lying at lower energies than the levels with e_g symmetry in a given spin channel. Hence the doped electron occupies the majority spin e_g levels. This results in a FM metallic state being stabilized at small values of U. While ferromagnetism gets stabilized by the hopping of the electron in the e_g level, in the absence of doping three electrons in the majority spin t_{2g} levels would favor an AFM configuration. One finds that with U, there is a decrease in stability of the FM state. Once the electron in the e_g level is localized a gap opens up. The majority t_{2g} electrons favor a G-type AFM ordering. The AFM background of d^3 configuration cancel out the magnetic moments while the extra electron when localized in one of the e_g states gives a net magnetic moment of approximately 0.8 μ_B per unit cell. Also in this region we do not find any spin-spiral stable ground states to be stable. At large U one finds that the the C-AFM and G-AFM magnetic configurations have comparable energy. We describe this regime as a Curie-Weiss paramagnetic (C-W PM) one.

In contrast to the $5d$ transition metal oxides where the presence of different phases did not show any significant doping dependence, the case of the $3d$ transition metal oxide is very different. Examining the phase diagram at 12.5% doping shown as inset (a) of Fig. 3.5, one finds a nonmagnetic metallic state at low U which transforms into a charge ordered insulating state as U is increased. The low concentration makes the energy gain from ferromagnetism associated with the doped electron small. Consequently no ferromagnetic metallic state is found at this limit.

In order to understand the charge ordered insulating phase found at a large value of U_{eff}, it is essential to understand the energetics stabilizing the different phases. Considering the doping concentration of 25%, the doped electron occupies the e_g level. This leads to a ferromagnetic state being favoured in the low U_{eff} limit. The stability of the ferromagnetic state is found to decrease with U_{eff}. This we find emerges because of the unusual ordering of charge carriers in the competing state in one-dimensional chains (running in the b-direction), while maintaining an overall G-type antiferromagnetic order. This results in a spin splitting of the oxygens flanked by a transition metal atom with the doped carrier on one side and another without the doped

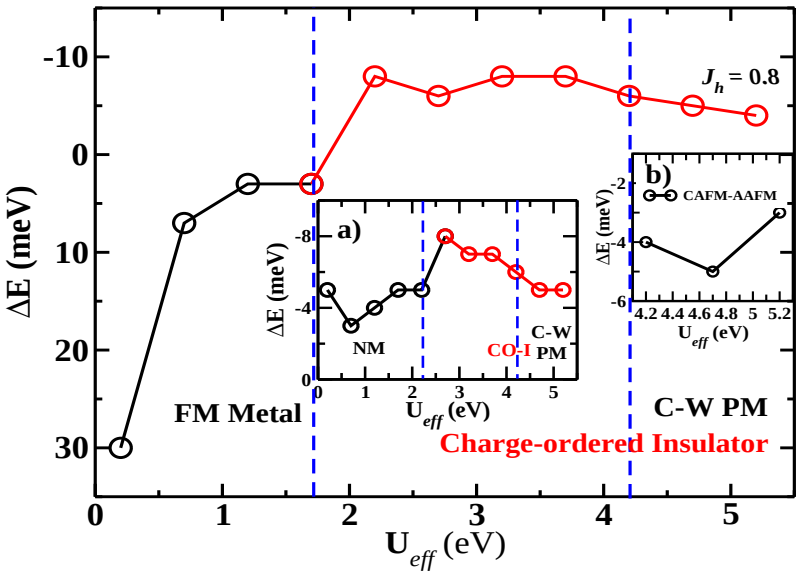

Figure 3.5: Relative stability ΔE calculated as the difference in energy between the G-AFM state and the FM state as a function of $U_{eff}(= U - J)$ at 12.5% (inset (a)) and 25% electron doping for the multiband case using parameters relevant for a $3d$ oxide. Dashed lines at U_{eff}=1.7 eV and 4.2 eV represent the phase boundaries.The CO-insulating state has a magnetic moment of 0.8 μ_B on one of the transition metal sites. In regime U > 4.2 eV The C-AFM and A-AFM magnetic configurations have competing energies as shown in the inset (b) for 25% doping. This lies within the error bars and so we name it as Curie-Weiss paramagnet (C-W PM). The nature of the ground state in each regime has been indicated.

carrier on the other side. This exchange splitting increases with U_{eff} leading to a decreased stability of the ferromagnetic state. We then have the charge carrier localized at a site leading to the charge ordered insulating state described earlier.

Considering the hopping interaction strengths which gives us the same bandwidth as the $5d$ oxide but with one orbital per transition metal site, we examine the phase diagram as a function of U (Fig.3.6). The oxygen atoms were not considered in this model. We find that in the small U limit, upto a U of $\sim$ 1.5 eV the system does not exhibit any magnetic order. One then has a narrow region where a C-type AFM metallic state is weakly stabilized. For large values of U we recover the Nagaoka FM metal limit and the stability of this phase keeps increasing with U. This is because energy of the FM state depends on the hopping interaction strength between sites which has a weak dependence on U. The AFM state, however, arising from the half-filled majority spin band varies as $1/U$. Hence there is an apparent increase in stability of the FM state with U. In between the AFM metallic regime and the FM metallic regime we have a

region where various magnetic configurations have similar energies which we associate with a Curie-Weiss paramagnetic phase.

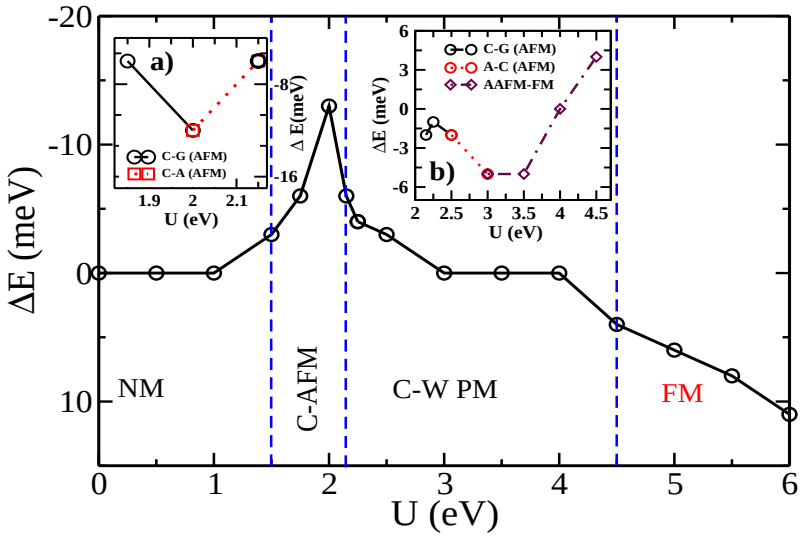

Figure 3.6: Relative stability ΔE calculated for 25% doping as the difference in energy between the C-AFM state and G-AFM/A-AFM as shown in the inset (a) for the region in which C-AFM is stabilized for the single band model. ΔE is computed as the difference in energy between the FM and the G-AFM state for the region in which FM is stabilized. In the region in which the C-W PM is stabilized, ΔE is shown between competing configurations (inset (b)). The nature of the ground state in different regimes has been indicated.

3.4 Conclusion

In conclusion, we have studied the case of electron doping in an AFM insulator within a multi-band Hubbard model considering interactions relevant for a $5d$ transition metal oxide. We explore the stability of various phases with a variation of U on the transition metal site. We found an AFM metallic state to be stabilized at small values of U while in the large U regime a charge-ordered insulating phase with a net magnetic moment per unit cell is found to be stable. In contrast, considering interactions which are relevant for a $3d$ transition metal oxide, one finds no regime where an AFM metallic phase is stable. The relative value of the crystal field splitting with respect to the exchange splitting determines if the doped electron occupies the minority spin t_{2g} level or the majority spin e_g level. When the doped electron is in the minority spin t_{2g} level, we have an antiferromagnetic metallic phase stabilized, while when the doped electron

is in majority spin e_g level, a ferromagnetic metallic phase is stabilized. While one has a FM metallic phase at low values of U, a charge ordered insulating phase is stabilized at large values of U. The large U regime of the multiband model has no limit at which one has a FM metallic phase as expected by the Nagoaka theorem. This is however found in the single band case. Orbital degeneracy is also found to play an important role in the enhanced stability of the AFM metallic phase.

Bibliography

[1] E. Fawcett, Rev. Mod. Phys. **60**1988209.

[2] V. M. Uzdin and C. Demangeat, J. Phys. Cond. Mat. **18**, 2717 (2006).

[3] C. Krellner, N. Caroca-Canales, A. Jesche, H. Rosner, A. Ormeci and C. Geibel, Phys. Rev. B (R) **78**, 100504 (2008).

[4] H. S. Jeevan, Z. Hossain, Deepa Kasinathan, H. Rosner, C. Geibel and P. Gegenwart, Phys. Rev. B **78**, 052502 (2008).

[5] T. Akimoto, Y. Maruyama, Y. Moritomo, A. Nakamura, K. Hirota, K. Ohoyama and M. Ohashi, Phys. Rev. B(R) **57**, 5594 (1998).

[6] A. C. Komarek, S. V. Streltsov, M. Isobe, T. Möller, M. Hoelzel, A. Senyshyn, D. Trots, M. T. Fernández-Díaz, T. Hansen, H. Gotou, T. Yagi, Y. Ueda, V. I. Anisimov, M. Grüninger, D. I. Khomskii and M. Brade, Phys. Rev. Lett. **101**, 167204 (2008).

[7] M.D. Johannes and I.I. Mazin, Phys. Rev. B **79**, 220510 (2009).

[8] T. Jungwirth, X. Marti, P. Wadley and J. Wunderlich, Nature Nano **11**, 231 (2016).

[9] V. Tshitoyan, C. Ciccarelli, A. P. Mihai, M. Ali, A. C. Irvine, T. A. Moore, T. Jungwirth and A. J. Ferguson, Phys. Rev. B **92**, 214406 (2015).

[10] B.G. Park, J. Wunderlich, X. Martí, V. Holý, Y. Kurosaki, M. Yamada, H. Yamamoto, A. Nishide, J. Hayakawa, H. Takahashi, A. B. Shick and T. Jungwirth, Nature Mater. **10**, 347 (2011).

[11] Y.Y. Wang, C. Song, B. Cui, G. Y. Wang, F. Zeng and F. Pan, Phys. Rev. Lett. **109** , 137201 (2012).

[12] J. Hubbard, Proc. R. Soc. A **276**, 238 (1963).

[13] M. Laubach, Darshan G. Joshi, Johannes Reuther, Ronny Thomale, Matthias Vojta and Stephan Rachel, Phys. Rev. B **93**, 041106 (2016).

[14] Seva Nimkar, D. D. Sarma, H. R. Krishnamurthy and S. Ramasesha, Phys. Rev. B **48**, 7355 (1993).

[15] J. E. Hirsch, Phys. Rev. B **31**, 4403 (1985).

[16] W. Nolting and W. Borgiel, Phys. Rev. B **39**, 6962 (1989).

[17] R. Peters and T. Pruschke, New J. Phys. **11**, 083022 (2009).

[18] A. Camjayi, M. J. Rozenberg and R. Chitra, Phys. Rev. B **76**, 195108 (2007).

[19] Yosuke Nagaoka, Phys. Rev. **147**, 392 (1966).

[20] Yosuke Nagaoka, Solid State Comm. **3**, 409 (1965).

[21] K. Kubo and Peter Thalmeir, J. Phys. Conf. Series **200**, 012097 (2010).

[22] Rong Yu, Kien T. Trinh, A. Moreo, Maria Daghofer, Jose A. Riera, S. Haas and E. Dagotto, Phys. Rev. B. **79**, 104510 (2009).

[23] Q. Luo and E. Dagotto, Phys. Rev. B. **89**, 045115 (2014).

[24] Ya-Min Quan, Liang-Jian Zou, Da-Yong Liu and Hai-Qing Lin, J. Phys. Condens. Matter **24**, 085603 (2012).

[25] Y. G. Shi, Y. F. Guo, S. Yu, M. Arai, A. A. Belik, A. Sato, K. Yamaura, E. Takayama-Muromachi, H. F. Tian, H. X. Yang, J. Q. Li, T. Varga, J. F. Mitchell and S. Okamoto , Phys. Rev. B(R) **80**, 161104 (2009).

[26] S. Calder, V. O. Garlea, D. F. McMorrow, M. D. Lumsden, M. B. Stone, J. C. Lang, J.-W. Kim, J. A. Schlueter, Y. G. Shi, K. Yamaura, Y. S. Sun, Y. Tsujimoto and A. D. Christianson , Phys. Rev. Lett. **108**, 257209 (2012).

[27] S. Middey, Saikat Debnath, Priya Mahadevan and D. D. Sarma, Phys. Rev. B **89**, 134416 (2014).

[28] S. Middey, Ashis Kumar Nandy, S. K. Pandey, Priya Mahadevan and D. D. Sarma, Phys. Rev. B **86**, 104406 (2012).

[29] Priya Mahadevan, K. Sheshadri, D. D. Sarma, H. R. Krishnamurthy and Rahul Pandit, Phys. Rev. B **55**, 9203 (1997).

[30] J. C. Slater and G. F. Koster, Phys. Rev. **94**, 1498 (1954).

[31] L. F. Mattheiss, Phys. Rev. B **2**, 3918 (1970).

[32] J. S. Griffith *The Theory of Transition-Metal Ions* Cambridge University Press, Cambridge (1961).

[33] Priya Mahadevan, N. Shanthi and D.D. Sarma, J. Phys. Cond. Mat. **9**, 3129 (1997).

[34] Priya Mahadevan, N. Shanthi and D. D. Sarma, Phys. Rev. B **54**, 11199 (1996).

Chapter 4

Absence of insulator to metal transition at higher band fillings: A model Hamiltonian study

4.1 Introduction

The classical concept of site percolation theory states that in a regular three dimensional lattice containing a fraction of conducting sites and remaining non-conducting sites, a finite conductivity through a connecting path extending over the whole lattice can only be obtained above a critical value of that fraction. In other words, if one dopes an insulating compound with extra charge carriers, it will only become conducting above a certain value of the doping concentration. For a simple cubic lattice which has a nearest neighbor coordination of 6, this critical concentration is ~ 0.31 [1, 2]. There are various existing examples in the literature among transition metal oxides where a insulator to metal transition is achieved by doping [3, 4]. The unusual examples among the doped transition metal oxides are those in which there is no transition into a metallic phase inspite of doping. Several explanations have been given in the literature behind such a resistance to go metallic. For example in an experimental study [5] of $La_{1-x}Sr_xCrO_3$ (LSCO), using photoemission and inverse photoemission spectroscopies, it was found that this system remained insulating even at 50 % hole doping. In this study, it was proposed that the impurity

potential causes localization of doped holes giving rise to an insulating ground state. This process was believed to be aided by a strong electron-phonon coupling leading to the formation of small polaronic distortions which localizes the hole. In another experimental study [6] on $La_{1-x}Sr_xFeO_3$ (LSFO), a similar polaronic picture was proposed for its insulating behavior even at 40 % doping. It was found that doped holes were able to introduce few states in the bandgap of the parent compound, but do not have sufficient bandwidth to overlap with the valence band maximum. Hence, though a substantial reduction in the bandgap occurs with carrier doping, the system remains insulating even at 40 % of hole doping. Although these studies qualitatively gave some insights about the insulating nature of the ground state at such high doping concentrations in these materials, they were unable to qualify the basic reason behind such an unusual but interesting phenomenon. There have been reports of some structural distortions in doped $LaCrO_3$, though the nature of distortions is unclear [7, 8]. Cr ions in $LaCrO_3$ correspond to a half filling of t_{2g} bands while Fe ions in $LaFeO_3$ correspond to a case of half filled e_g bands. In contrast, $LaMnO_3$ which is an insulator, becomes metallic with doping of Sr atoms in it at a doping concentration of $\sim$ 20 % [9]. In this case the Mn^{+3} ions are in d^4 configuration and doping holes in this case seems to be different from the previously discussed case which correspond to half filling of t_{2g}/e_g bands. This raises the question whether the half filled limit has something to do with the inability to drive these systems metallic.

We have examined the studies based on Hubbard model to see if there is any clue about the origin of this behavior. In a study by Wang *et al.* [10], solving the single band t-J model in the large U limit of the Hubbard model within a mean field approach, it was shown that the system remains antiferromagnetic and insulating below a critical doping concentration causing doped holes to have a very narrow bandwidth. Based on this finding, it was speculated that polaronic physics may be operative in this case [11–13]. However, no concrete calculations were shown to support this argument. Another problem with such a single band model is that it misses out the orbital degeneracy present in the case of a real material. Such degeneracies when included in a multiband model can lead to different ground state properties than the single band case with similar parameters used in both the cases. Studies have been done considering multiband Hubbard models in the context of pnictides to explain the antiferromagnetic metallic ground state. Also, the doped multiband Hubbard model has been used to discuss the role of Jahn-Teller

(JT) polaronic distortions, orbital polarization etc. in stabilizing a charge ordered/orbitally ordered insulating phase with doping in transition metal oxides [14, 15]. But these studies have mainly focused on the doped manganites.

In the background of these observations, a detailed study was required to understand the underlying physics behind an insulating nature of the ground state in the hole doped $3d$ transition metal oxides away from half filling. In this chapter, we have addressed this problem using a multiband Hubbard Hamiltonian solved within the mean field approximation. The advantage of using this technique is that we have control over various electronic structure parameters which makes it easier to understand their individual roles in any specific properties shown by the system. Considering the parameters that are relevant for a $3d$ transition metal oxide, stability of the ground state was calculated at different hole doping concentrations as a function of U_{eff} on the transition metal d states. Based on these results, phase diagrams were obtained for different doping concentrations. We found that at U_{eff} values relevant for a $3d$ transition metal oxide, insulating ground states appear. This insulating state was found to be a charge ordered one with the doped holes localized in t_{2g} orbitals at transition metal sites. One would think that the gain in energy for this insulating state is coming from the large Hund's exchange interaction strength (J_h) present in the case of a $3d$ oxide as in this limit there are no delocalization pathways available for the doped holes in a fully antiferromagnetic configuration of background spins. By reducing the value of J_h to a much smaller value we still found the charge ordered insulating ground state stabilized and hence a dominant role of Hund's splitting in this case was ruled out. Although the Hund's exchange interaction strength is reduced artificially in our calculations, the exchange splitting remains large and so there is a substantial gain in this case. This emerged from the large superexchange interaction between neighboring transition metal sites at this limit as in the case when one is away from this limit, other exchange pathways will effectively suppress such a splitting. Also, as we know that the superexchange mechanism between the transition metal d orbitals is mediated via oxygen p orbitals, the charge transfer energy (Δ) is expected to have significant contribution towards superexchange. In order to investigate this, we lowered its value from 2 eV to 0 eV while J_h was kept fixed at its earlier value 0.8 eV. We found that in this case also the charge ordered insulating ground state was stabilized with stability comparatively higher than that of the original case. From this analysis we con-

cluded that it was the gain from strong superexchange background which favors the localization of hole even at large doping concentrations. Our calculations for $La_{1-x}Sr_xCrO_3$ at $x = 25$ % doping within the *ab initio* approach, also supports the charge ordered insulating ground state. We also determined the nature of distortions found in this case. We included these distortions within our model calculations and still find a charged ordered insulating ground state with the bandgap almost doubled from its value when there were no distortions in the structure.

With the considered model Hamiltonian, similar to the $3d$ oxide case, calculations were also done for a $5d$ transition metal oxide. It was found that the presence of large hopping interactions and a small Hund's splitting in this case pushes the system to a more itinerant limit, allowing for the antiferromagnetic metallic state to be stabilized over a wider range of U_{eff}. The superexchange interaction due to the localized spins is much larger for the electron doped case than for the hole doped case. This consequently leads to an asymmetry in the results obtained for electron doping and hole doping. The asymmetry is even stronger in the $3d$ case where the magnetic metallic phase is antiferromagnetic for hole doping and ferromagnetic for electron doping.

4.2 Methodology

In order to understand the stability of different magnetic phases we set up a multiband Hubbard-like Hamiltonian considering the $NaOsO_3$ lattice. The basis consists of d orbitals on Os and s, p orbitals on oxygen atoms. The Hamiltonian is given by

$$\begin{aligned} H = &\sum_{i,l,\sigma} \epsilon_d d^\dagger_{il\sigma} d_{il\sigma} + \sum_{i,l,\sigma} \epsilon_p p^\dagger_{il\sigma} p_{il\sigma} + \sum_{i,l,\sigma} \epsilon_s s^\dagger_{il\sigma} s_{il\sigma} \\ &- \sum_{i,j,l_1,l_2,\sigma} \left(t^{l_1 l_2}_{i,j,pd} d^\dagger_{il_1\sigma} p_{jl_2\sigma} + \mathbf{H.c.} \right) \\ &- \sum_{i,j,l_1,l_2,\sigma} \left(t^{l_1 l_2}_{i,j,pp} p^\dagger_{il_1\sigma} p_{jl_2\sigma} + \mathbf{H.c.} \right) \\ &- \sum_{i,j,l_1,l_2,\sigma} \left(t^{l_1 l_2}_{i,j,sd} d^\dagger_{il_1\sigma} s_{jl_2\sigma} + \mathbf{H.c.} \right) \\ &+ \sum_{\alpha\beta\gamma\delta,\sigma_1\sigma_2\sigma_3\sigma_4} U^{\alpha\beta\gamma\delta}_{dd} d^\dagger_{\alpha\sigma_1} d^\dagger_{\beta\sigma_2} d_{\gamma\sigma_3} d_{\delta\sigma_4} \end{aligned}$$

where $d^{\dagger}_{il\sigma}\,(d_{il\sigma})$ creates (annihilates) an electron with spin σ in the lth d orbital on transition metal site in the ith unit cell while $p^{\dagger}_{il\sigma}\,(p_{il\sigma})/s^{\dagger}_{il\sigma}\,(s_{il\sigma})$ creates (annihilates) an electron with spin σ in the lth p/s orbital on oxygen atom in the ith unit cell. The s orbitals on oxygen are included as they simulate the effect of a crystal field splitting on the Os d states and were kept fixed at -20 eV deep inside the valence band. This represents their approximate position inside the valence band. In a distorted perovskite, the t_{2g} states are not pure d_{xy}, d_{yz} and d_{xz} orbitals but have some admixture of $d_{x^2-y^2}$ and $d_{3z^2-r^2}$. Consequently the introduction of different diagonal energies for d_{xy}, d_{yz}, d_{xz} compared to $d_{x^2-y^2}$ and $d_{3z^2-r^2}$ orbitals to simulate the crystal field splitting cannot be done. An alternate way that has been used in the past [16, 17] is to introduce s orbitals on oxygen which interact only with the e_g orbitals on the Os site. The parameters in the tight binding part of the Hamiltonian were determined by fitting the $ab-initio$ band structure for $NaOsO_3$. The best fit Slater-Koster parameters [18] we got from this fitting are $sd\sigma$= -3.65 eV, $pd\sigma$= -3.75 eV , $pd\pi$= 1.80 eV, $pp\sigma$= 0.7 eV, $pp\pi$=-0.15 eV and $\epsilon_d-\epsilon_p$ =0.8 eV and were used in the earlier work [19] also. The charge transfer energy defined as $\Delta=\epsilon_d-\epsilon_p+3U$ was kept fixed at 2 eV and a small intra-atomic Hund´s exchange interaction strength (J_h) of 0.1 eV was used. The complete multiplet interactions on the d orbitals on Os were considered. These were parameterized in terms of the Slater Condon integrals [20], with the values of the Slater integrals F^2 and F^4 set at a fixed percentage of their atomic Hartree Fock values to give the desired value of the intra atomic exchange interaction strength J_h ($=\frac{F^2+F^4}{14}$). The multiplet averaged U was used to define the value of F^0. A mean field decoupling scheme was used to reduce the four fermion terms in the Hamiltonian to two-fermion terms which were then solved for self-consistently [21, 22]. Further details of the calculational approach may be found in Ref∼ [23]. To study the limit corresponding to a $3d$ transition metal oxide, the hopping interactions strength used were -1.88 ($pd\sigma$) and 0.90 ($pd\pi$) which are typical values for a $3d$ transition metal oxide [23, 24]. Additionally a large value of the intra atomic exchange interaction strength (J_h) of 0.8 eV was used. These parameters for a $3d$ transition metal oxide are consistent with earlier estimates for a $3d$ transition metal atom in their oxides [25]. The phase diagrams were calculated at several doping concentrations as indicated in the text. In order to probe the role of degeneracy on the phase diagram, we considered a lattice containing only the transition metal atoms with just one orbital per site and examined the phase diagram

for 25% electron doping. The hopping interaction strength was chosen in this case to give us the same bandwidth as the 5d oxides. Additionally an onsite Coulomb interaction strength was used. In each case, the total energies of various magnetic configurations , were calculated to evaluate the phase diagram as a function of U.

In the *ab initio* part of our analysis, using a plane wave pseudopotential implementation of density functional theory using PAW potentials [26, 27] implemented in Viena *Ab initio* simulation package (VASP) [32], the electronic and magnetic properties of $La_{1-x}Sr_xCrO_3$ at 25 % hole doping is calculated. For this purpose, experimentally proposed structure of $LaCrO_3$ was considered [28] and one out of four La is replaced by Sr atom. Also since there are four Cr sites in a unit cell one doped hole means 25 % of hole doping in this system. For the exchange correlation functional, the GGA PW91 [29, 30] approximation has been used. The effects of electron-electron correlation on the transitional metal d electrons were considered within the GGA+U scheme using the Dudarev *et al.* formalism [31].In our calculations, a U of 3.0 eV on the Cr-d states was considered A Gamma centered k-mesh of $6 \times 4 \times 6$ have been used. In order to determine the ground state and the next excited state, total energies have been calculated for various configurations such as A, C, G-type antiferromagnetic configurations as well as for the ferromagnetic one. All these calculations have been using the

In order to bias the system towards a charge ordered solution, we artificially break the symmetry around one of the Cr site closest to the doped Sr atom. For this purpose, the Cr-O bond lengths that of a particular Cr are made 0.06 Å shorter than their previous values and with these new coordinates we performed simple relaxation of internal coordinates. We found that a U of $\sim$ 2.5 eV was necessary to open up a bandgap at the Fermi energy which enhances with increase of U to the value of 3 eV, the most relevant for this material. All the calculations were then performed considering $U = 3$ eV on Cr d states.

4.3 Results and Discussions

4.3.1 Model Hamiltonian Study

The $3d$ transition metal oxides with a half filled t_{2g} band have been difficult to dope. We first examined hole doping as a route to drive the system metallic. The favored ground state has been calculated for doping percentages of 12.5 %, 25 %, 37.5 % and 50 % and its stability with respect to the closest excited state is given in Fig. 4.1. As discussed earlier, a J_h of 0.8 eV has been used on the transition metal site as this is a typical value for $3d$ transition metals in oxides. As the value of U could vary depending on the transition metal atom, we examine the stability as a function of U. The plots showing the change in stability of the ground state with variation of U_{eff} on the transition metal site is shown in panels (a)-(d) of Fig 4.1.

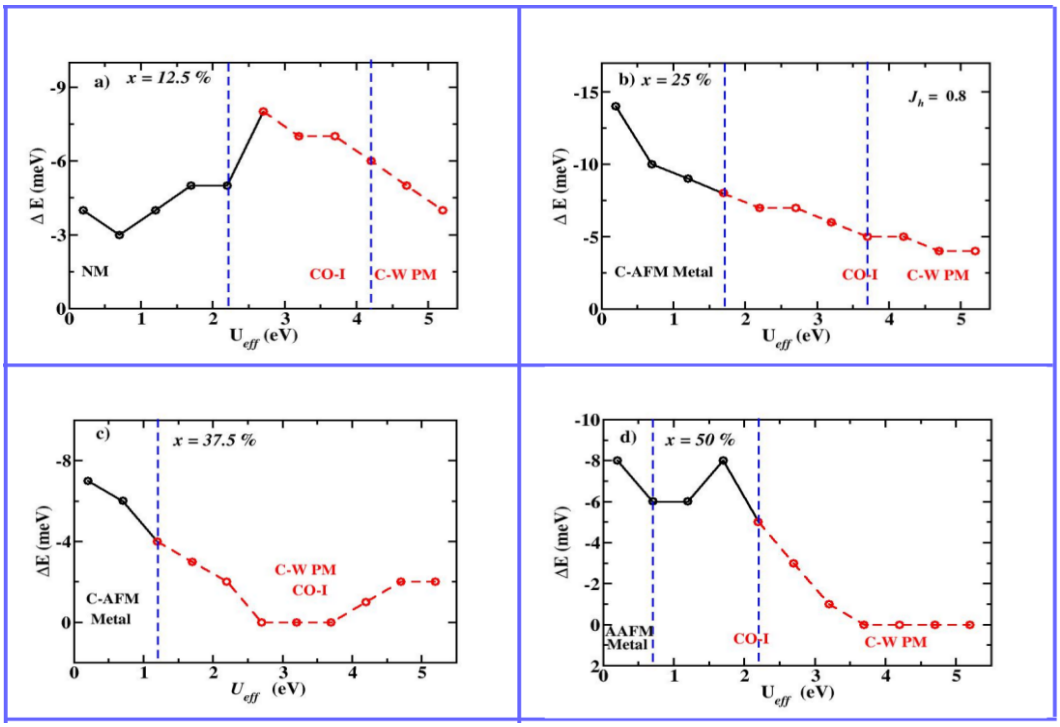

Figure 4.1: Four panels for hole doped $3d$ oxide case at (a) 12.5 %, (b) 25 %, (c) 37.5 % and (d) 50 %. In the relevant region for a $3d$ transition metal oxide between 2-3 eV, in each of these phase diagrams we always have charge ordered insulating phase stabilized.

At a low doping concentration of 12.5 %, in the low U_{eff} region, a non-magnetic metallic ground state was found to be stabilized upto 2.2 eV. When we further increased the value of U_{eff}, a charge ordered insulating state gets stabilized. One should note here that it is the region

with the value of U_{eff} between 2-3 eV which is relevant for an early $3d$ transition metal in an oxide. In our calculations the insulating ground state emerges naturally in this region of the phase diagram. As U_{eff} is increased, magnetic order is stabilized with nearest neighbor spins favoring an antiferromagnetic arrangement. This is determined by the occupied spins at the undoped limit. The doped hole, however, would favor a ferromagnetic arrangement and has no delocalization pathways present in an antiferromagnetic arrangement. A competition of both these energetics determines the favored magnetism. As the hole is localized at a site, a charge ordered insulating state emerges. While the magnetic moment on different transition metal sites in the undoped limit cancel each other out, one finds a net moment of $\sim 0.65\ \mu_B$ at the doped limit. The stability of this charge ordered insulating state decreases with increase of U_{eff}. This can be understood from the fact that gain from superexchange interactions, which varies as t^2/U, decreases with increase in the value of U. This decreases the stability of the G-type antiferromagnetic state associated with the spins at each site. Beyond $U_{eff} = 4.2$ eV, many magnetic configurations start competing and the energy difference between them was found to be negligibly small (less than 5 meV). We call this region a Curie-Weiss paramagnetic (C-W PM) region.

When one goes from 12.5 % to 25 % hole doping, the region at intermediate and higher U_{eff} remain the same with a shift in the phase boundaries. In the intermediate U_{eff} region we have the charge ordered insulating state which turns into a C-W paramagnetic region with an increase of U_{eff}. The low U_{eff} region in this case has changed substantially and now we have a C-type antiferromagnetic metallic region stabilized in this case. Although this region is not relevant for a $3d$ transition metal oxide, we will briefly explain the reason behind such a phase which was not present at a doping concentration of 12.5 %. The spins associated with the three electrons in the majority spin t_{2g} states at each site are antiferromagnetically aligned in each case while the doped hole would like to be in a ferromagnetic configuration to gain from kinetic energy. The competition between these two at this doping percentage leads to a C-type antiferromagnetic phase. As the doping concentration increases, gain from the ferromagnetically aligned spins increases and one can expect lowering in stability of the C-type AFM state. Indeed, when we go from 25 % to 37.5 % hole doping, we have a C-AFM metallic ground state in low U_{eff} region with substantial reduction in its stability both in absolute values as well as the range of U_{eff}.

As the hole concentration is increased, the gain from ferromagnetically aligned spins increases and we found that the competing state at both these doping concentrations was the A-type antiferromagnetic state. When we further increase the doping percentage to 50 %, the A-type antiferromagnetic metallic ground state stabilized in a narrow U_{eff} region at lower values with the stability now calculated with respect to the ferromagnetic metallic one. Further increase of the U_{eff} drives the system insulating and in a smaller window of it till 2.2 eV, we have a charge ordered insulating ground state. A Curie-Weiss paramagnetic region was again found at the higher values of U_{eff} at this doping percentage. We now will discuss in detail the intermediate region of U_{eff}, relevant in the case of a $3d$ transition metal oxide as it is our prime concern here.

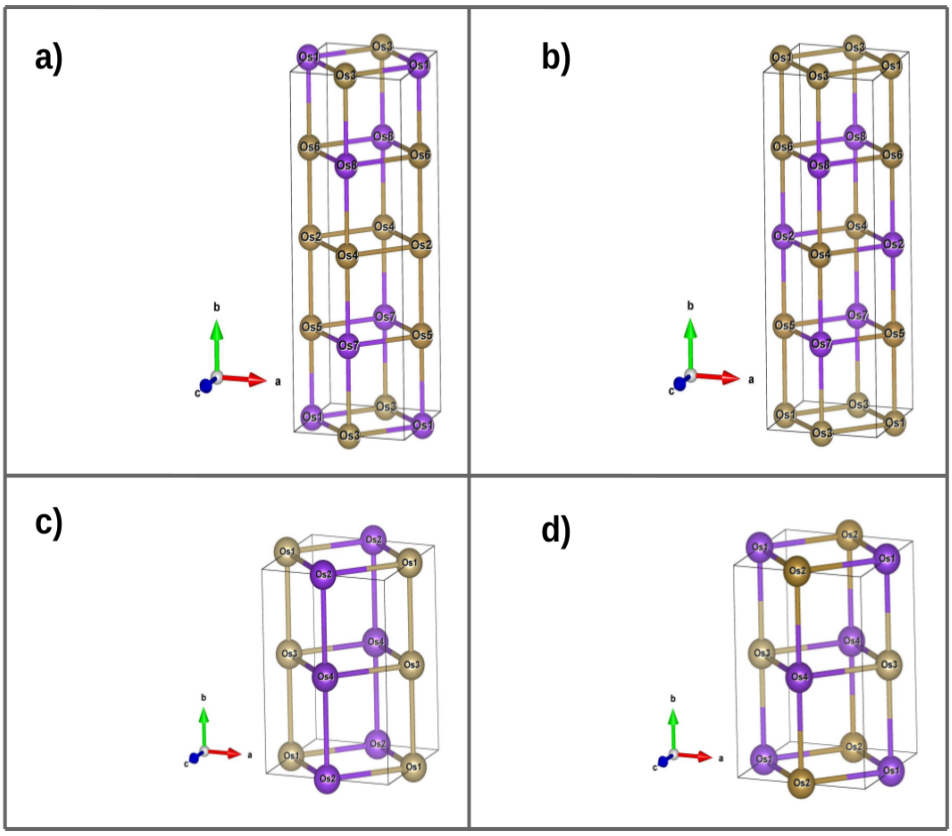

Figure 4.2: Two different charge ordered solutions shown shown in the case of 37.5 % and 50 % hole doping. At 37.5 % doping, charge ordered ground state is shown in panel (a) while the next competing charge ordered solution is shown in panel (b). Similar at 50 % hole doping, CO ground is shown in panel (c) while the next competing CO solution is shown in panel (d).

Doping three holes in the supercell containing eight transition metal atoms is effectively 37.5 % hole doping while doping two holes in the four transition metal atom unit cell is 50 % hole doping. In both these cases, many different charge ordered solutions are possible depending

upon the doped holes being localized on a particular transition metal. We have explored all these configurations. Out of these configurations, we have shown two configurations in Fig 4.2 for each 37.5 % and 50 % hole doping case. The one in the left panel (a) is the ground state while the one in panel (b) is the next competing one for 37.5 % hole doping. Similarly at 50 % doping, ground state is shown in panel (c) while the next competing CO state is shown in panel (d). The blue balls represent the transition metal site which has the hole localized on it.

In the ground state configuration for 37.5 % of hole doping, the transition metal sites with the localized holes are surrounded by the sites with no hole and vice versa. The exchange splitting at the sites with holes is smaller when compared to the sites with no hole and hence the system gain energy by the superexchange interaction in this scenario. Also in the ground state, a plane without a hole on transition metal atom separates two of the planes with the doped hole from the third one. In the case of 50 % hole doping, we found ground state has the hole localized on to nearest neighbor transition metal atoms along the y-direction and is shown in panel (c) while in the next competing configuration the localized holes were found to be on the next nearest neighbor transition metal atoms which is shown in panel (d).

As discussed in the introduction of this chapter, percolation theory predicts the critical carrier doping concentration of ~ 0.31 % for a three dimensional simple cubic lattice beyond which the system is expected to be metallic. However, there are many examples of the $3d$ transition metal oxides with simple cubic crystal structure for whom the experimental studies found no insulator to metal transition even upto a carrier doping concentration as large as 50 %. Transition metal atoms in these oxides had a formal electronic configuration which had either half filled t_{2g} orbitals and hence a d^3 configuration or half filled e_g orbitals with d^5 configuration. Explanation for the inability to drive the system metallic have invoked strong electron phonon interactions which lead to polaron formation and localization of the charge carriers [5,6]. However, if we look at the phase diagrams at different doping concentrations, we found that it is always a charge-ordered insulating ground state that is favored in the relevant U_{eff} range of 2-3 eV. In our model we have not included any lattice distortions and we found an insulating state. This suggests that a part of the energetics stabilizing the insulating state should be present within the model that we have considered here. Lattice distortions help in stabilizing one particular configuration for the localized holes over several degenerate ones.

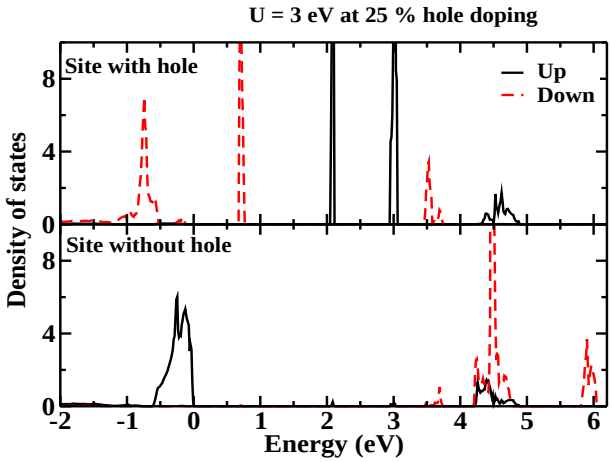

Figure 4.3: Density of state at 25 % hole doped case for $U_{eff} = 2.2$ eV. These are for t_{2g} orbitals at two different transition metal site with (upper panel) and without (lower panel) extra hole.

In order to develop a clear understanding of the charge ordered insulating region in the phase diagrams obtained in Fig 4.1, we have plotted the spin polarized transition metal d density of states in Fig 4.3 at 25 % hole doping for $U_{eff} = 2.2$ eV. In the upper panel, density of states plotted is for the transition metal site with localized doped hole while the lower panel is for the normal transition metal site without any localized hole. A clear difference can be seen in both these plots as one can find a splitting of t_{2g} states in the upper channel plot which is absent in the plot of the lower channel. We found two important features of the density of states which are in reasonable agreement with the experiment. The first one is that the doped hole indeed get localized 0.7 eV above the Fermi energy as was observed in the experimental studies [5, 6]. The second point is that this hole indeed has a vary narrow bandwidth in the antiferromagnetic configuration. Now one should analyze in detail the possible mechanisms behind such a behavior.

A schematic energy level diagram for a $3d$ transition metal oxide is shown Fig 4.4. Due to large Hund's exchange splitting present in these compounds compared to the crystal field splitting. One has first t_{2g} and e_g orbitals in one spin channel lower in energy and then the same ordering of orbitals in other spin channel. The three electrons at a given transition metal site occupy the majority spin t_{2g} levels. The large Hund's exchange interaction strength could be responsible for localizing the doped hole at a single atomic site. This then drives the system insulating.

In order to examine this hypothesis, we reduced the magnitude of Hund's splitting at the transition metal site in our model from 0.8 eV (relevant for a $3d$ oxide) to 0.1 eV (usually the case of

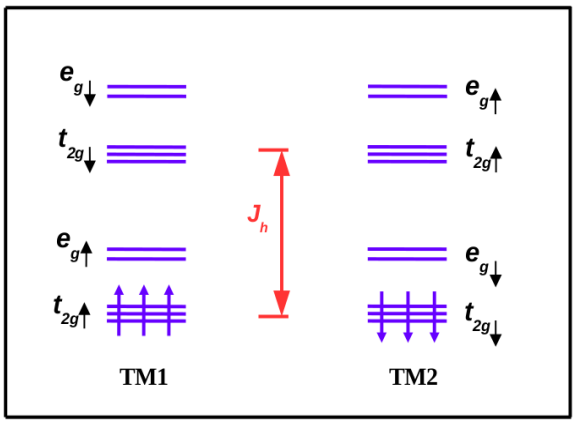

Figure 4.4: Schematic representing energy level diagram of the $3d$ orbitals in a typical $3d$ transition metal oxide with G-type antiferromagnetic arrangement of spins.

a $5d$ oxide) while keeping all the other parameters of the Hamiltonian the same. Although this new combination of parameters does not represent a realistic system, it would atleast provide us an idea about the role of Hund's splitting in such materials. With this small value of J_h we have again calculated the phase diagram at 25 % of hole doping and the obtained plot is shown in Fig 4.5.

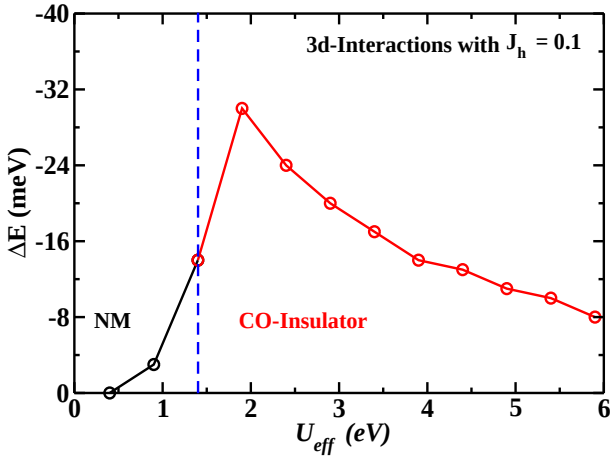

Figure 4.5: Phase diagram obtained for 25 % hole doping in a $3d$ oxide with reduced $J_h = 0.1$ eV. In the region relevant for a $3d$ transition metal oxide, here also we have the charge ordered insulating ground state stabilized.

In the relevant U_{eff} region for the $3d$ oxide, the ground state was still found to be the charge ordered insulating one with the enhanced stability when compared to the case of $J_h = 0.8$ eV. Similar to what we found earlier, the stability of this charge ordered insulating phase was again found to decrease with an increase of U_{eff}.

A quick look at the density of states in this case shown in Fig 4.6 for $U_{eff} = 2.2$ eV, reveals that even for this small value considered for the Hund's interaction strength, we find that the exchange splitting of the states is large. This can be understood as arising from the large superexchange interaction between the neighboring transition metal sites in this limit. This contributes to the large exchange splitting that we find at this limit. At other fillings, the superexchange channel does not play such an important role in determining the exchange splittings.

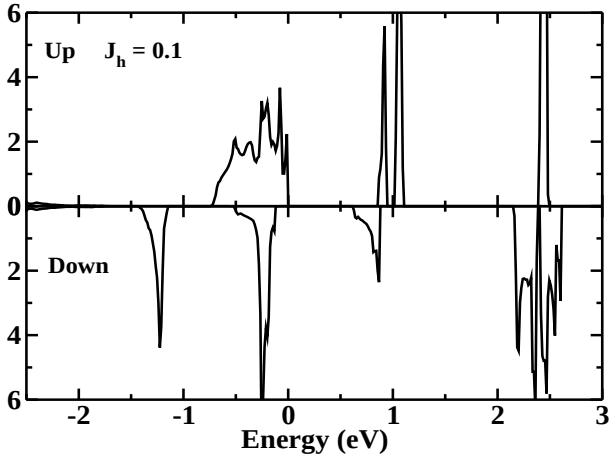

Figure 4.6: The spin polarized transition metal d density of states plot at 25 % hole doping for $3d$ oxide with reduced $J_h = 0.1$ eV at $U_{eff} = 2.2$ eV. Even after reduction of Hund's exchange splitting J_h from 0.8 eV (in original case) to 0.1 eV in present case, an effective exchange splitting is clearly visible in this case.

An alternative route to increasing the superexchange interaction strength is by varying the charge transfer energy. We varied the charge transfer energy (Δ) which is defined as the energy difference between the configurations $d^{n+1}\bar{L}$ and d^n where $\bar{L}$ denotes a hole in the ligand levels. Its value changes from being large and positive in the early $3d$ transition metal oxides to very small or even negative in the case of late transition metal $3d$ oxides.

Considering this point, we reduced Δ within our model from 2 eV to 0 eV while keeping all other parameters the same for a $3d$ oxide. The calculated phase diagram at 25 % doping is shown in Fig 4.7. We found that similar to the previous results in this case also, in the relevant region of U_{eff} value between 2-3 eV, the system is still a charge ordered insulator. The stability is enhanced with respect to the case when we had a large Δ. This is because the superexchange interaction between neighboring transition metal sites is enhanced. Additionally, the stability of this insulating state decreases in the similar fashion with increase in the U_{eff}. This further

supports the hypothesis that it is the gain from the strong superexchange background which favors the localization of hole even at large doping percentages consequently making the system insulating.

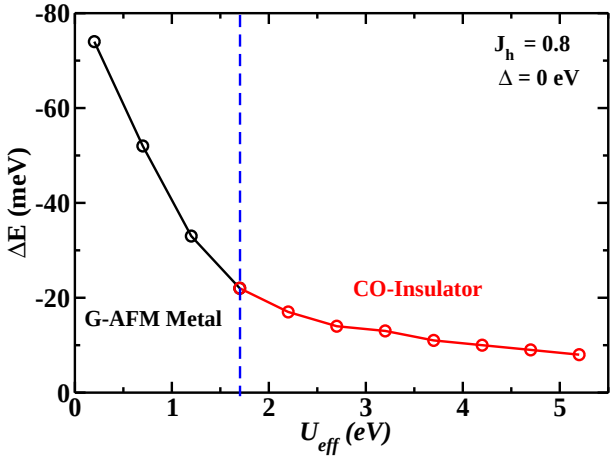

Figure 4.7: Phase diagram obtained in the case of 25 % hole doping in $3d$ transition metal oxide with $\Delta = 0$ eV. Here also we have charge ordered insulating region stabilized with greater stability than the original case of $\Delta = 2$ eV. The extra gain is coming from the enhanced superexchange contribution from the background spins.

4.3.2 *Ab initio* Study

In $LaCrO_3$, Cr in its ionic configuration of 3+ has three d electrons in the t_{2g} orbitals and so an ideal system to study the hole doped case. We took the experimental structure [28], replaced one La atom with Sr which leads to doping of one hole. Since there are four Cr atoms in the unit cell, this corresponds to 25 % hole doping. *Ab initio* calculations have been carried out considering various magnetic configurations like, G-type, C-type, A-type antiferromagnetic and ferromagnetic configurations with a U of 3 eV on the Cr-d orbitals. By simple relaxation of the internal coordinates in these calculations we found that in the absence of any structural distortion, the system is found to be G-type antiferromagnetic metal. For the doped hole, all the four Cr sites in the unit cell are equivalent and so there exists a structural degeneracy in terms of doped holes which has to be broken in order to localize the electron onto one of the Cr site. For this purpose, we choose one of the Cr atom close to doped Sr atom and artificially broke the symmetry by making this Cr-O bondlengths 0.06 Å smaller than that of the other ones. With this new structure we again allowed for relaxation of the internal coordinates and

performed similar calculations for different magnetic configurations. We found that the system is now insulating with G-type antiferromagnetic ground state. After relaxation, the Cr-O bond lengths obtained for the Cr atom (Cr2) which had the hole localized on it is found to be 1.90, 1.91, 1.93, 1.94, 1.96 and 1.97 Å (Fig. 4.8).

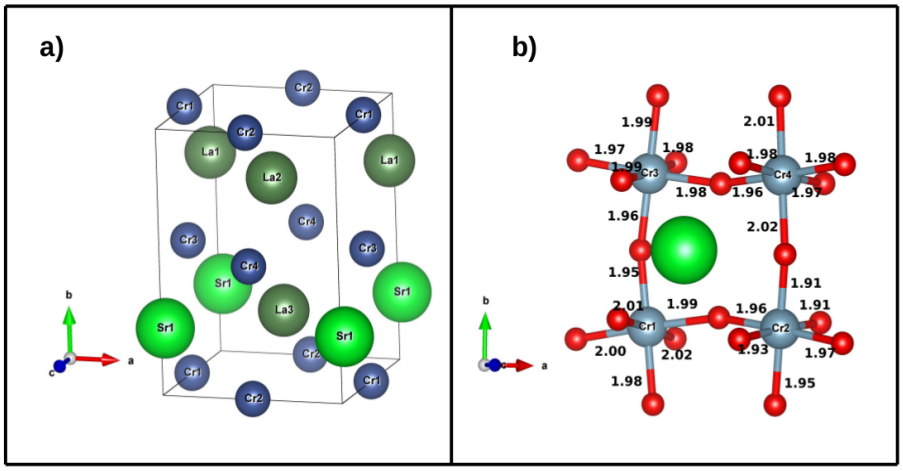

Figure 4.8: The Cr network along with La atoms and doped Sr atom is shown in panel (a). In panel (b), structural distortions at 25 % hole doping in $LaCrO_3$ within the *ab initio* approach. The green big ball is the doped Sr atom. Cr2 has the shortest Cr-O bondlengths. All these bondlengths are in Å unit.

The Cr-O bondlengths of the other Cr atoms have also been shown. A comparison of the energy difference between the previous metallic and now insulating G-type antiferromagnetic reveals that the insulating ground state is stabilized by 18 meV per formula unit of energy. Although we found negligibly small charge difference between the two different Cr sites, as has been observed earlier in other charge ordered systems an analysis of the Cr-O bond lengths and the net magnetic at each Cr site supports the idea of one Cr site being in the +4 oxidation state while all others are in +3 oxidation state. The magnetic moment for the sites identified as Cr^{+3} sites are found to be $\sim 2.81\ \mu_B$ while for the charge ordered site it was $\sim 2.06\ \mu_B$. The next excited here was found to be the C-type antiferromagnetic state and the energy difference between this excited state and the G-type antiferromagnetic ground state was found to be only 7 meV per formula unit. We also found that even after inclusion of magnetism, a minimum U of ~ 2.5 eV was necessary to make the system insulating and a small bandgap of 80 meV was found at this value of U. Hence it can be concluded that the role electron-electron correlations is also crucial in such systems in stabilizing an insulating ground state with doping of charge carriers. At $U = 3.0$ eV,

this bandgap increases to $\sim$ 0.32 eV. Using the new positions obtained for the charge ordered insulating ground state within the *ab initio* calculations and the electronic structure parameters for $LaCrO_3$ from [24], we again set up the multiband Hubbard Hamiltonian to reexamine the the 25 % hole doping case. Here also we found the charge ordered insulating ground state stabilized with the band gap enhanced to almost double the value found in the absence of distortions. This suggests that both effects, the exchange splitting induced localization of the hole, and the polaronic distortions play almost equal role in driving the system insulating.

So far we have discussed the case of a $3d$ transition metal oxide mainly in the context of insulating ground state after hole doping in exactly half filled limit of the t_{2g} orbitals. However, the above discussion will also remain valid for the case of a $3d$ oxide with ionic d^5 configuration and the hole doping would be into the half filled e_g orbitals. The strong superexchange background will still be operative and the system will remain insulating even upto a higher hole doping concentration as was found in the case of $La_{1-x}Sr_xFeO_3$.

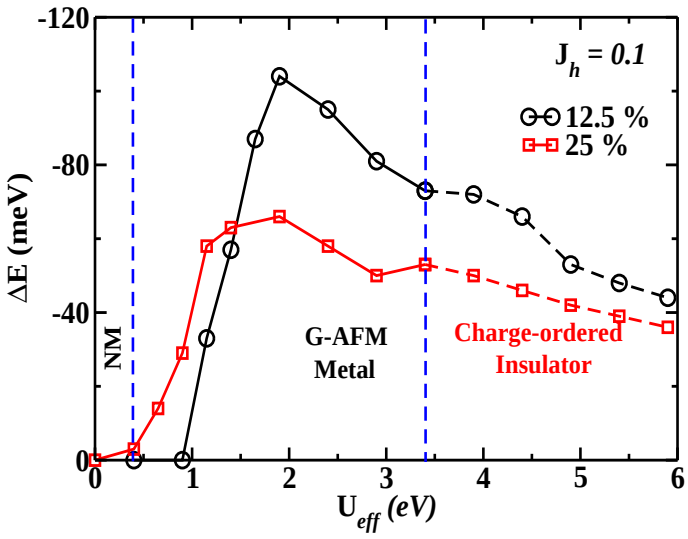

Figure 4.9: Phase diagram obtained for hole doping in $5d$ transition metal oxide at 12.5 % and 25 % doping concentrations. The antiferromagnetic metallic phase is stabilized in a wider range of U_{eff} when compared to their electron counterpart published in Ref [33]. At higher values of U_{eff} we again have the charge ordered insulating ground state.

We next went on to examine the changes in phase diagram that occur when we move from a $3d$ to a $5d$ transition metal oxide. This was mainly motivated by two facts. The first is that in the case of a $5d$ transition metal oxide, the hopping interactions are nearly doubled in magnitude to that

of a $3d$ transition metal oxide while the intra site Coulomb repulsion is smaller in comparison to the $3d$ oxide. Also the Hund's exchange splitting is small in this case. All these can push the system towards more itinerant limit. This can lead to a stronger superexchange background and hence may substantially change the stability of various phases. The second point is that electron doping at the exactly half filled t_{2g} limit of a $5d$ transition metal would lead to delocalization of the electron in the minority spin channel as the Hund's splitting is small for such an oxide. On the other hand, when one dopes holes, they will occupy the majority spin t_{2g} orbitals itself. So one wanted to examine if the physics in the cases of electron and hole doping is similar or would it be substantially different. Using the parameters relevant for a $5d$ transition metal oxide, we set up the similar multiband Hubbard Hamiltonian and calculated the phase diagram as a function of U_{eff} in the same fashion mentioned in previous discussion of the $3d$ oxide. A plot of the phase diagram obtained at 12.5 % and 25 % hole doped case is shown in Fig 4.9. In the small U_{eff} region, initially one has a non-magnetic state stabilized in a comparatively narrow range for 25 % doping than for 12.5 % hole doping and with a further increase of U_{eff}, one has an G-type antiferromagnetic phase stabilized whose stability first increases with increase of U_{eff} upto a certain value and then starts decreasing with increase in U_{eff}. When one compares this region of the phase diagram with electron doped case discussed in Chapter 3, one finds that the antiferromagnetic metallic phase state is stabilized over a wide range of U_{eff} in the present case. This happens because in the case of electron doping, the superexchange background is much stronger and untouched as the doped electron goes into the minority spin channel at transition metal sites. But this superexchange background gets weaker in the case of hole doping as it takes place into the majority spin channel itself. This pushes the charge ordered insulating region to much higher value of U_{eff} providing the antiferromagnetic metallic phase to be stabilized in a much wider region of the phase diagram. This consequently leads to an asymmetry in the results obtained in these two cases. Also these states are strongly stabilized compare to the states in the phase diagram for the $3d$ oxide. One can also find that the gain in stability decreases with increase of the hole doping concentration. These results are similar to what was found in the case of electron doping in a $5d$ transition metal oxide discussed in chapter 3. Hence, based upon this asymmetry obtained in the case of electron and hole doping, one can conclude that hole doping in an exactly half filled $5d$ transition metal oxide is more viable route to stabilize an

antiferromagnetic metallic ground state. With further increase of U_{eff}, we again have a charge ordered insulating phase stabilized at much higher values and we do not have a C-W PM region in this phase diagram of $5d$ oxide. It should be noted that polaronic effects are expected to be weaker in a $5d$ oxide. The U is also expected to be smaller than 3.5 eV, so we don't expect to encounters the charge-ordered state. However in a highly distorted $5d$ oxide, one could be pushed in the regime of a higher U/W. This could result in a charge ordered state being stabilized in a doped $5d$ transition metal oxide. There it would emerge primarily from electronic effects.

The asymmetry introduced by electron doping versus hole doping is even stronger in the low U_{eff} region of the phase diagram for a $3d$ transition metal oxide. As we found in the case of electron doping at 25 % of doping that this region was ferromagnetic metallic while it is found to be antiferromagnetic metallic in the case of hole doping. However this region does not belong to an actual case of a $3d$ transition metal oxide.

4.4 Conclusion

In this study, we have explained the driving mechanism behind the robust insulating state found even at high carrier doping found in the case of some of the transition metal oxides like $LaCrO_3$ and $LaFeO_3$. Phase diagrams were obtained with variation of U on the transition metal d states for both $3d$ and $5d$ transition metal oxides. We found that in the region which is relevant for the $3d$ oxide, charge ordered insulating ground state appears naturally at carrier doping concentrations as high as 50 %. We rule out the role of large Hund's interaction in the stabilization of such an unusual ground state and show that this mechanism will be operational in the systems with small values of Hund's interaction also, suggesting that there could be examples among the $4d$ and the $5d$ transition metal oxides which could also refuse to go metallic on doping. By varying charge transfer energy (Δ), we show that the superexchange interactions of localized spins at the transition metal sites lead to a large exchange splitting at this limit and is mainly responsible for the charge ordered insulating insulating ground state. Hence we conclude that the exchange splitting induced localization of carriers and the polaronic distortions play an almost equal role in driving the system insulating among the $3d$ transition metal oxides. Additionally in the case of a $5d$ transition metal, we found that the superexchange is stronger

in the electron doped case than the hole doped one. Based upon our findings we suggested that hole doping is a more viable route to achieve the AFM metallic phase.

Bibliography

[1] M. F. Sykes and J. W. Essam, Phys. Rev. **133**, A310 (1964).

[2] M. J. Powell, Phys. Rev. B **20**, 4194 (1979).

[3] S. W. Cheong and H. Y. Hwang, *Ferromagnetism versus charge/orbital ordering in mixed-valent manganites Colossal Magnetoresitance Oxides*, London: Gordon and Breach (2000).

[4] J. P. Hill et. al., arXiv:cond-mat/0105064.

[5] K. Maiti and D. D. Sarma, Phys. Rev. B **54**, 7816 (1996).

[6] A. Chainani, M. Mathew, and D. D. Sarma, Phys. Rev. B **48**, 14818 (1993).

[7] J. J. Neumeier and Hirotoshi Terashita, Phys. Rev. B **70**, 214435 (2004).

[8] Kelvin H. L. Zhang *et al.*, Adv. Mat. **27**, 5191 (2015).

[9] O. Chmaissem, B. Dabrowski, S. Kolesnik, J. Mais, J. D. Jorgensen and S. Short, Phys. Rev. B **67**, 094431 (2003).

[10] Y.R. Wang and M.J. Rice, Synthetic Metals **80**, 159 (1996).

[11] L.N. Bulaevskii and D.I. Khomskii, Sov. Phys. JEEP, **25**, 1067 (1967).

[12] L.N. Bulaevskii, E.L. Nagaev and D,l. Khomskii, Sov. Phys. JETP, **27**, 839 (1968).

[13] W.F. Brinkman and T.M. Rice, Phys. Rev. B, **2**, 4302 (1970).

[14] Takashi Hotta, Andre Luiz Malvezzi and Elbio Dagotto, Phys. Rev. B, **62**, 9432 (2000).

[15] R. Kilian and G. Khaliullin, Phys. Rev. B, **60**, 13458 (1999).

[16] L. F. Mattheiss, Phys. Rev. B, **2**, 3918 (1970).

[17] Priya Mahadevan, N. Shanthi and D. D. Sarma, Phys. Rev. B, **54** 11199 (1996).

[18] J. C. Slater and G. F. Koster, Phys. Rev., **94**, 1498 (1954).

[19] S. Middey, Saikat Debnath, Priya Mahadevan and D. D. Sarma, Phys. Rev. B, **89**, 134416 (2014).

[20] J. S. Griffith, *The Theory of Transition-Metal Ions*, (Cambridge University Press, Cambridge) (1961).

[21] Seva Nimkar, D. D. Sarma, H. R. Krishnamurthy and S. Ramasesha, Phys. Rev. B, **48**, 7355 (1993).

[22] Priya Mahadevan, K. Sheshadri, D. D. Sarma, H. R. Krishnamurthy and Rahul Pandit, Phys. Rev. B, **55**, 9203 (1997).

[23] S. Middey, Ashis Kumar Nandy, S. K. Pandey, Priya Mahadevan and D. D. Sarma, Phys. Rev. B, **86**, 104406 (2012).

[24] Priya Mahadevan, N. Shanthi and D. D. Sarma, Phys. Rev. B, **54**, 11199 (1996).

[25] Priya Mahadevan, N. Shanthi and D.D. Sarma, J. Phys. Cond. Mat., **9**, 3129 (1997).

[26] P. E. Blöchl, Phys. Rev. B **50**, 17953 (1994).

[27] G. Kresse, D. Joubert, Phys. Rev. B **59**, 1758 (1999).

[28] K. Tezuka, Y. Hinatsu, A. Nakamura, T. Inami, Y. Shimojo and Y. Morii, J. Sol. Stat. Chem., **141**, 404 (1998).

[29] G. Kresse, J. J. Furthmüller, Phys. Rev. B **54**, 11169 (1996).

[30] J. P. Perdew, K. Burke, Y. Wang, Phys. Rev. B **54**, 16533 (1996).

[31] S. L. Dudarev, G. A. Botton, S. Y. Savrasov, C. J. Humphreys, A. P. Sutton, Phys. Rev. B **57**, 1505 (1998).

[32] M. Marsman and J. Hafner, Phys. Rev. B **66**, 224409 (2002).

[33] S. K. Pandey, Priya Mahadevan and D. D. Sarma, Euro Phys. Lett., **117**, 57003 (2017).

Chapter 5

Cr doping in Rutile VO_2: A first principle study

5.1 Introduction

Among the magnetic systems that one encounters, an empirical rule has emerged, which is that ferromagnetism is accompanied by a metallic ground state while antiferromagnetism is found in members that are insulating. The ones that break these empirical trends are the most interesting members as they would require a mechanism beyond the conventionally accepted theories to explain the origin of the magnetic state. In this work we consider one example of a recently discovered ferromagnetic insulator, $V_{1-x}Cr_xO_2$ [1–5]. The parent compounds VO_2 [6–9] and CrO_2 [10–13] are antiferromagnetic insulator and ferromagnetic metal respectively. However, experiments have found that upto 20 % Cr doping in the rutile phase of VO_2, the system is found to become a ferromagnetic insulator. X-ray absorption spectroscopy which, apart from being atom specific is also sensitive to the valence state, reveals the presence of Cr^{+3}-V^{+5} pairs for even higher doping concentrations [5]. The question that follows is what is the origin of these pairs and how do they determine the magnetic state that is favored.

In this work we consider the rutile phase of VO_2 which is the structure favored in the thin films and examine the evolution of electronic structure as well as magnetism on Cr doping. We are able to reproduce the experimental trend of a ferromagnetic insulating state at 12.5 % Cr

doping. This is surprising in two aspects. Firstly as discussed earlier, we have the uncommon realization of a ferromagnetic insulating ground state. Secondly, an isovalent substitution of V by Cr would lead to electron being doped, and therefore a metallic state. What is it that impedes the formation of a metallic state here ?

On doping Cr into VO_2, we find that it spontaneously goes into the 3+ valence state, taking an extra electron from a neighboring V site. Allowing for structural relaxations, stabilizes this Cr^{3+}-V^{5+} pair even more. An examination of the onsite energies of Cr and V determined by a mapping of the *ab initio* band structure onto a tight binding model, supports this observation. The Cr^{3+} levels are found to be below the V levels, allowing for the spontaneous formation of Cr^{3+} configuration. A substantial stabilization for the Cr^{3+} state must be derived from the large Hund's intraatomic exchange strength associated with the d^3 configuration at the Cr site, in addition to the attractive Coulomb interaction one has between Cr^{3+} and V^{5+} ions. The fact that one has unoccupied levels on neighboring V sites to which the electrons on Cr can hop to, allows for a ferromagnetic insulating state to be stabilized. We went on to calculate the energy gain coming from the Cr^{3+}-V^{5+} pathways via-a-vis the Cr^{3+}-V^{4+} one and show that it is the dominant one stabilizing the ferromagnetic insulating state.

5.2 Methodology

In order to calculate the electronic structure of Cr doped VO_2, we have performed first principle density functional calculations using Vienna *ab initio* simulation package [14]. We have used projected augmented wave [15] potentials. For the different k-space integrations we have used a $6 \times 6 \times 8$ Gamma-centered mesh of k-points and a plane wave cutoff of 400 eV with high precession for our calculations. The generalized gradient approximation (GGA) [16] was used for the exchange-correlation functional and electron-electron interactions were considered by including a Hubbard U within the GGA+U formalism [17]. We have used a U of 2.5 eV on V atoms and a U of 3 eV on the Cr atoms. The total energy was calculated self-consistently till the energy difference between successive steps was better than 10^{-5} eV. The total energy of the ferromagnetic configuration was compared with the energy of other antiferromagnetic configurations within the 24 atom $\sqrt{2} \times \sqrt{2} \times 2$ supercell. In order to understand the results further we

have fitted the *ab initio* band structure with a tight binding model using maximally localized wannier functions with WANNIER90-VASP interface [18, 19] implemented within VASP. Using the Cr and V d and O p states in the basis, we extracted the onsite energies as well as the hopping interaction strengths. The band energy has been computed within the tight binding Hamiltonian and it corresponds to the sum over the occupied eigenvalues within the model that we have considered.

5.3 Results and Discussions

In order to understand the electronic and magnetic properties of $V_{1-x}Cr_xO_2$, we first consider 12.5 % Cr doping. In a supercell with eight V atoms, replacement of one V atom with Cr corresponds to 12.5 % doping. We then optimized the unit cell lattice parameters as well as the internal coordinates within our calculations. This was done by considering various magnetic configurations and the ferromagnetic state was found to be the ground state. For the ferromagnetic configuration, the optimized lattice vectors were found to be $a = 6.393$ Å, $b = 6.401$ Å and $c = 5.965$ Å. The optimized lattice parameters obtained in the case of the next excited state (AFM1), which is an antiferromagnetic one, were found to be slightly different from the ferromagnetic case. For the AFM1 configuration $a = 6.390$ Å, $b = 6.397$ Å and $c = 5.976$ Å.

	Total energy (eV)	Net MM (μ_B)
FM	0.0	9
AFM1	0.1	1.0
AFM2	0.12	3.0
AFM3	0.284	1.0
AFM4	0.297	1.0

Table 5.1: Relative energies of different antiferromagnetic magnetic configurations with respect to ferromagnetic configuration for 12.5 % doping of Cr in rutile VO_2.

A comparison of total energy obtained for different magnetic configurations at 12.5 % doping is tabulated in Table 5.1. We can think of the super cell of VO_2 to consist of four V chains running along the c-direction as the distance between the V atoms is the shortest in this direction. In the AFM1 configuration, atoms are aligned ferromagnetically along the chain running along c-direction but the inter-chain coupling is antiferromagnetic. Another, AFM configuration (AFM2) which we have considered has the coupling within the chains antiferromagnetic.

AFM4 configuration was made by considering ferromagnetic coupling within the chain but nearest neighbor chains are coupled antiferromagnetically. We found the ferromagnetic state to be the ground state with an energy difference of $\sim$ 0.1 eV from the next excited state (AFM1). The calculated density of states is shown in Fig. 5.1 and one finds an insulating ground state for the ferromagnetic solution. This is consistent with experiment.

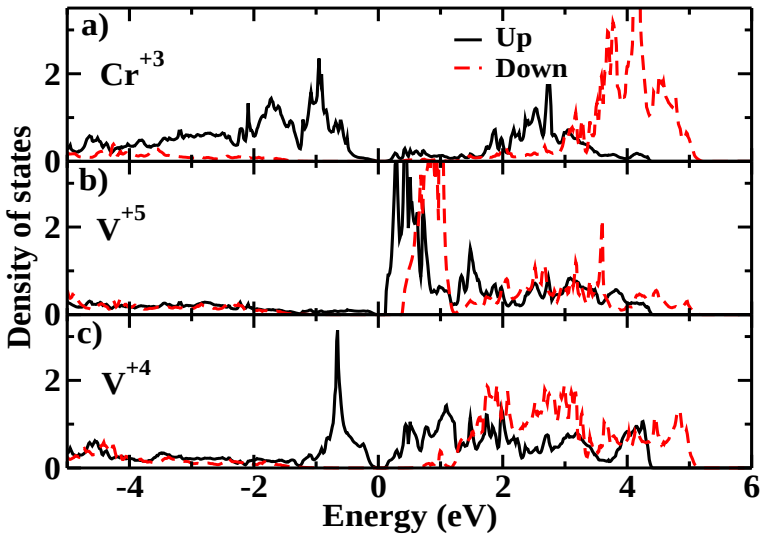

Figure 5.1: Spin-polarized atom projected d density of states plots for ferromagnetic insulating ground state. Different panels correspond to, (a) Cr^{+3}, (b) V^{+5} and (c) V^{+4} ions at 12.5 % Cr doping in rutile phase of VO_2. This plot was obtained after volume optimization of the initial experimental structure of VO_2.

The octahedral environment that the transition metal atoms is in due to the neighboring oxygen atoms splits the five d orbitals into triply degenerate t_{2g} orbitals and doubly degenerate e_g orbitals. By looking at density of states plots, one can clearly see the signature of the presence of two different types of V atoms in this doped compound. V in its +4 ionic configuration has one electron in the t_{2g} orbitals in the majority spin channel. In the case of a higher valency of +5 on V, all the d orbitals are empty. Panel (b) of Fig. 5.1 corresponds to the V atom which has +5 valence state while panel (c) corresponds to the V atom with +4 valence state. Hence, we have a clear signature of charge ordering present at the V sites. The d density of states shown for the doped Cr atom in panel (a) reveals that the t_{2g} orbitals of one spin channel is fully filled while in the other spin channel it is entirely empty suggesting +3 (d^3 configuration) valence state of the Cr atom. After analysis of individual magnetic moments of all the atoms,

we found that the Cr atom has a moment of $\sim 2.95\ \mu_B$ moment reflecting the presence of three valence electrons on it and hence +3 valence state of Cr. V atom close to the Cr site (2.7 Å) has a small moment of $\sim 0.2\ \mu_B$ supporting the presence of a higher valence state of +5. Moments on other V ions remain close to $1.14\ \mu_B$ representing a +4 valence state. We found a negligibly small magnetic moment of $\sim 0.05\ \mu_B$ on the oxygen atoms too. These results clearly indicates the formation of Cr^{3+}-V^{5+} pairs which has been reported in many experimental studies.

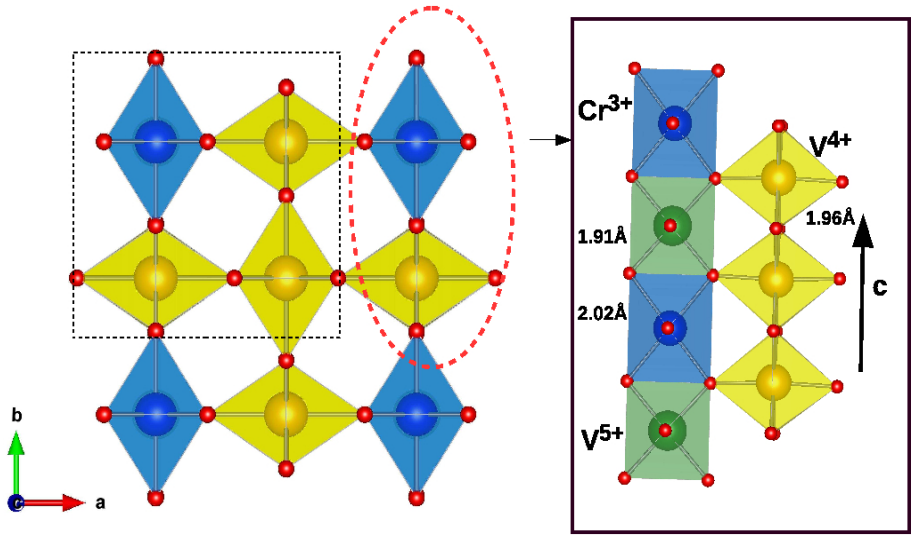

Figure 5.2: The $\sqrt{2} \times \sqrt{2} \times 2$ supercell has been shown in left while the formation of Cr^{+3}-V^{+5} chain as well as the bond lengths have been shown in the right for 12 % Cr doped in VO_2. The blue and green balls represent Cr^{+3} and V^{5+} while V^{+4} ions are represented by the yellow balls.

The considered supercell used for calculations is shown in the left panel of Fig. 5.2. The V atom which has become V^{+5}, is nearest to the doped Cr atom (2.7 Å) and situated in the crystallographic c-direction. These Cr^{3+}-V^{5+} pairs form a chain in the c-direction as shown in the right panel of Fig. 5.2. The blue and green balls represent Cr^{+3} and V^{5+} atoms while V^{+4} ions are represented by the yellow balls. Here we should mention the major changes in fully optimized structure obtained for Cr doped VO_2 when compared to the parent material VO_2. The Cr-O bond lengths in the optimized structure were found to be 1.96 Å ($\times$ 2) along the b-direction and 2.02 Å ($\times$ 4) in the ac-plane. All the V-O bond lengths were 1.96 Å in the undoped VO_2. The V^{+4}-O bond lengths remain more or less similar to the parent compound with two bonds a little shorter (1.92/1.93 Å) along the b-direction. As one would expect shorter V-O bond lengths for a higher valency of V atom, we also found the V^{+5}-O bond lengths to be 1.90 Å ($\times$ 6) smaller than that of the V^{+4}-O ones. Based on these results, several immediate

questions arise. For example, what leads to the charge ordering at the V sites and formation of Cr^{3+}-V^{5+} pairs, how does this pairing helps in realizing the ferromagnetic insulating ground state, why does the doped Cr atom acquire +3 oxidation state rather than +4 oxidation state which would, emerge from an isovalent substitution.

To answer all the above mentioned questions, we have done a tight binding analysis of the unrelaxed Cr doped VO_2 experimental structure. One should note here that, in this structure, both the V as well as the Cr atoms are in +4 oxidation state. In this analysis, the spin-polarized *ab initio* band structure for the ferromagnetic configuration was mapped on to a tight binding model in which the radial parts of the wavefunctions are considered to be maximally localized Wannier functions. Considering the transition metal d and oxygen p orbitals in the basis, the onsite energies were extracted from the obtained mapping. Based upon this analysis, an energy level diagram showing the position of various orbitals in the majority spin channel is shown in Fig. 5.3.

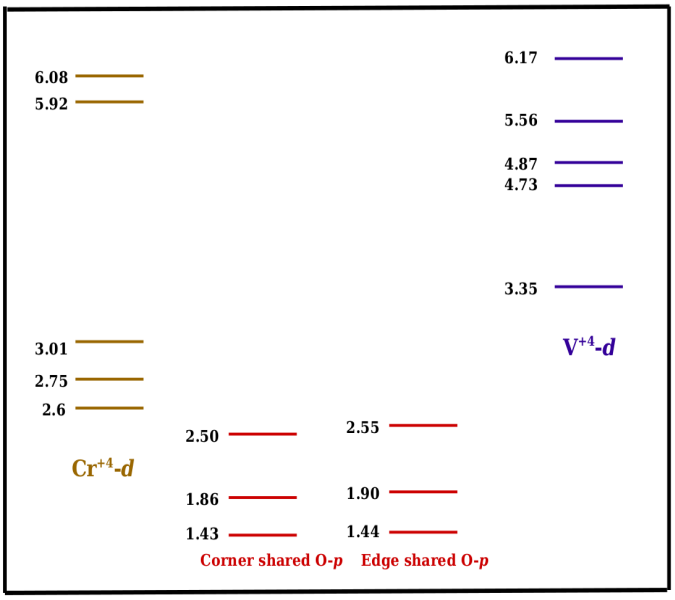

Figure 5.3: Energy level diagram for Cr^{+4} d orbitals, corner and edge shared oxygen p orbitals and V^{+4} d orbitals in the unrelaxed structure for 12.5 % Cr doped VO_2. This was obtained by fitting the *ab initio* band structure within a tight binding model considering Cr, V d and O p orbitals in the basis. The radial part of the wavefunctions are considered to be maximally localized Wannier functions.

Here we found that the lowest lying V-d t_{2g} orbital with the onsite energy 3.35 eV was $\sim$ 0.3 eV higher in energy than the highest Cr-d t_{2g} level with the onsite energy $\sim$ 3.0 eV. This is

the reason that the Cr d levels have three electrons on them. This large stability for the Cr^{+3} configuration emerges from the large Hund's stability associated with a half-filled t_{2g} band. Allowing for an optimization of the structure, we find that the structural distortions aid this ordering at the Cr^{+3} site. Additionally, one finds that the oxygens around one V have distorted resulting in a V^{+5} configuration. The other V atoms are in the +4 configuration and the system becomes insulating after the relaxations.

This analysis offers answers to few of the questions raised earlier, however few questions remain unanswered like why do we have a ferromagnetic ground state, how does the Cr^{3+}-V^{5+} pair formation help in realizing a ferromagnetic state. In order to develop a clear understanding on these issues, we again did the Wannier analysis for the band structure to extract out the tight binding Hamiltonian parameters. We considered the fully optimized structure for our analysis. A comparison of the spin-polarized *ab initio* band structure with the tight binding one in both the spin channels is shown in Fig. 5.4.

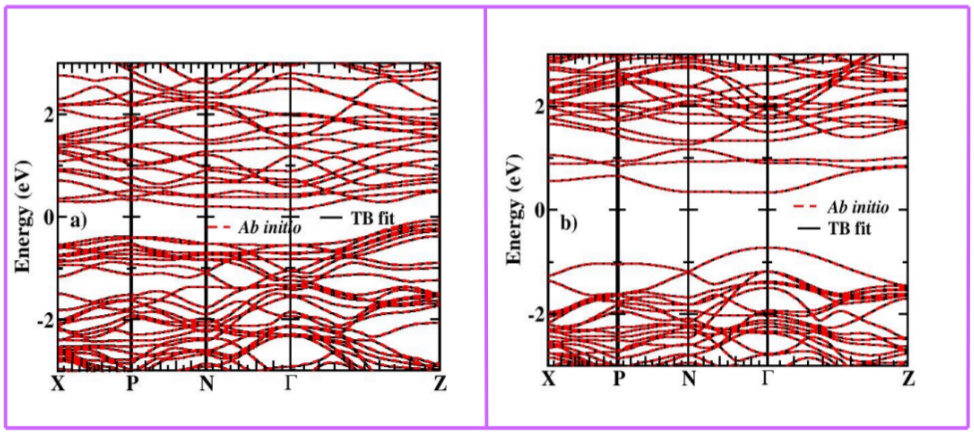

Figure 5.4: Plots from obtained fitting of *ab initio* spin-polarized band structure within a tight binding model considering Cr, V d and O p states in the basis at 12.5 % Cr doped VO_2 after full volume optimization. Radial part of the wavefunctions are considered to be the maximally localized Wannier functions. For ferromagnetic configuration, description obtained in up (left) and down (right) spin channels.

One finds that one has a reasonably good description of the band structure which gives us the confidence to use the Hamiltonian for further analysis.

An estimate of the energy gain obtained from various hopping pathways available in this doped system would enable us to quantify their role in stabilization of such an unusual ground state.

For this purpose, we artificially switch off the Cr^{3+}-V^{5+} interactions via the intermediate oxygen atoms and calculated the band energy. A comparison of the evaluated band energy with the value obtained from without switching off any interactions would provide us with the energy gain via the mentioned hopping pathways. We found that the gain in energy via this hopping channel in the ferromagnetic configuration was $\sim$ 7 eV per hopping pathway. However, when a similar analysis was done after switching off direct interaction between Cr^{3+}-V^{5+} pairs, we found a very small energy gain of 0.065 eV. Based on these two results one can conclude that there is no direct pathway between the Cr^{3+}-V^{5+} pair. The exchange pathway is through the oxygen atoms. We also estimated the energy gain from all Cr-V^{4+} hopping pathways via the oxygen atoms. We found the gain in ferromagnetic configuration to be 3.11 eV per hopping pathway.

The substantial gain from the exchange pathway between Cr^{3+}-V^{5+} sites suggests an important role played by the charge ordering in stabilizing a ferromagnetic insulating state. Similar ideas were discussed by some of us in the context of another ferromagnetic insulator $K_2Cr_8O_{16}$ [20] and the present analysis for the first time is able to quantify the role of various exchange pathways.

Previous *ab initio* study suggested a half metallic ferromagnetic character of Cr doped VO_2 in rutile phase at 25% doping [21, 22]. This study was done considering a 12 atom supercell where replacing one of the V with Cr atom correspond to 25 % doping. In order to investigate the system at this doping concentration, we replace two out of eight V atoms in our 24 atom supercell which correspond to the same doping concentration. We allowed for volume optimization of this structure considering various magnetic configurations. The results comparing the total energy and net magnetic moment evaluated for ferromagnetic as well for various antiferromagnetic configurations at 25 % doping are given in Table 5.2.

	Total energy (eV)	Net MM (μ_B)
FM	0.0	10
AFM1	0.091	0
AFM2	-0.031	6
AFM3	0.56	2
AFM4	0.38	4

Table 5.2: Relative energies of different antiferromagnetic magnetic configurations with respect to ferromagnetic configuration for 25 % doping of Cr in rutile VO_2.

In contrast to the previous study, we found that the ground state in this case was the AFM2 configuration, and was insulating in nature with an energy band gap of $\sim$ 0.69 eV. The AFM2 configuration is similar to 12.5 % with the only difference that the two doped Cr atoms which are in the farthest chain are antiferromagnetic coupled. In the AFM1 configuration, these two Cr atoms are again in the farthest chain but are ferromagnetically coupled and the interatomic coupling is antiferromagnetic. The Cr^{3+}-V^{5+} pairs were also found in this ground state at 25 %. Each Cr has magnetic moment of 2.92 μ_B, slightly enhanced from its previous value while the V^{+4}/V^{+5} has magnetic moments reduced from their previous values in 12.5 % and are found to be $\sim$ 1.01/0.04 μ_B. The lattice vectors obtained for the ground state in this case was found to be a = 6.41 Å, b = 6.53 Å and c = 5.89 Å. However, no experimental date is available at this doping concentration to verify the findings of our calculation. We also did total energy calculations to examine the ground state at 50 % Cr doping and obtained results which are tabulated in Table 5.3.

	Total energy (eV)	Net MM (μ_B)
FM	0.0	12
AFM1	0.109	0
AFM2	0.198	0
AFM3	0.104	6
AFM4	0.171	0

Table 5.3: Relative energies of different antiferromagnetic magnetic configurations with respect to ferromagnetic configuration for 50 % doping of Cr in rutile VO_2.

We found a ferromagnetic insulating ground state at this concentration. In this case also, we found Cr^{3+}-V^{5+} pairs. The individual magnetic moments of different ionic species were Cr^{3+} - 3 μ_B, V^{5+} - 0.36 μ_B. However this is not in agreement with the experimentally proposed antiferromagnetic insulating ground in Ref. [23]. The failure in reporting the experimental ground state coule be due to various factors such as the need to go beyond GGA+U for the exchange correlation functional.

5.4 Conclusion

The ferromagnetic insulating state found in Cr doped VO_2 has been investigated within *ab initio* electronic structure calculations coupled with microscopic modeling within a tight binding model.

We are able to find this ground state within our calculations. Its stability is explained from the emergence of Cr^{3+}-V^{5+} pairs which are found to be strongly stabilized by attractive Coulomb interactions. The presence of unoccupied t_{2g} levels at the V^{5+} site and occupied t_{2g} levels at the Cr^{3+} site leads to a superexchange pathway via the oxygens. This is found to strongly stabilize the ferromagnetic insulating state and its role is quantified for the first time.

Bibliography

[1] M. Marezio, B. Mcwhan, P. D. Dernier, and J. P. Remeika, Phys. Rev. B **5**, 2541 (1972).

[2] J. B. Goodenough and H. Y. P. Hong, Phys. Rev. B **8**, 1323(1973).

[3] J. P. Pouget, H. Launois, J. P. D'Haenens, P. Merenda, and T. M. Rice, Phys. Rev. Lett. **35**, 873 (1975).

[4] K. G. West, J. Lu, L. He, D. Kirkwood, W. Chen, T. P. Adl, M. S. Osofsky, S. B. Qadri, R. Hull, and S. A. Wolf, J. Supercond. Novel Magn. **21**, 87 (2008).

[5] L. F. J. Piper, A. DeMasi, S. W. Cho, A. R. H. Preston, J. Laverock, K. E. Smith, K. G. West, J. W. Lu, and S. A. Wolf, Phys. Rev. B **82**, 235103 (2010).

[6] Z. Yang, C. Ko, and S. Ramanathan, Annu. Rev. Mater. Res. **41**, 337 (2011).

[7] F. J. Morin, Phys. Rev. Lett. **3**, 34 (1959).

[8] M. W. Haverkort, Z. Hu, A. Tanaka, W. Reichelt, S. V. Streltsov, M. A. Korotin, V. I. Anisimov, H. H. Hsieh, H.-J. Lin, C. T. Chen, D. I. Khomskii, and L. H. Tjeng, Phys. Rev. Lett. **95**, 196404 (2005).

[9] T. C. Koethe, Z. Hu, M. W. Haverkort, C. Schüßler-Langeheine, F. Venturini, N. B. Brookes, O. Tjernberg, W. Reichelt, H. H. Hsieh, H.-J. Lin, C. T. Chen, and L. H. Tjeng, Phys. Rev. Lett. **97**, 116402 (2006).

[10] R. J. Soulen, J. M. Byers, M. S. Osofsky, B. Nadgorny, T. Ambrose, S. F. Cheng, P. R. Broussard, C. T. Tanaka, J. Nowak, J. S. Moodera, A. Barry and J. M. D. Coey, Science **282**, 85 (1998).

[11] B. L. Chamberland, Crit. Rev. Solid State Mater. Sci. **7**, 1 (1977).

[12] Y. S. Dedkov, A. S. Vinogradov, M. Fonin, C. König, D. V. Vyalikh, A. B. Preobrajenski, S. A. Krasnikov, E. Y. Kleimenov, M. A. Nesterov, U. Rüdiger, S. L. Molodtsov, and G. Güntherodt, Phys. Rev. B **72**, 060401 (2005).

[13] J. M. D. Coey, A. E. Berkowitz, L. Balcells, F. F. Putris, and A. Barry, Phys. Rev. Lett. **80**, 3815 (1998).

[14] G. Kresse, and J. Furthm*ü*ller, Phys. Rev. B. **54**, 11169 (1996); G. Kresse, and J. Furthm*ü*ller, Comput. Mat. Sci. **6**, 15 (1996).

[15] G. Kresse, and J. Joubert,Phys. Rev. B **59**, 1758 (1999).

[16] J. P. Perdew, Y. Wang Phys. Rev. B. **45**, 13244 (1992).

[17] S.L. Dudarev et.al. Phy. Rev. B. **57**, 1505(1998).

[18] A. A. Mostofi, J. R. Yates, Y.-S. Lee, I. Souza, D. Vanderbilt and N. Marzari, Comput. Phys. Commun. **178**, 685 (2008).

[19] C. Franchini, R. Kovik, M. Marsman, S. S. Murthy, J. He, C. Ederer and G. J. Kresse Phys.: Condens. Matter **24**, 235602 (2012).

[20] Priya Mahadevan, Abhinav Kumar, Debraj Choudhury and D. D. Sarma, Phys. Rev. Lett. **104**, 256401 (2010).

[21] M. E. Williams, W. H. Butler, C. K. Mewes, H. Sims, M. Chshiev and S. K. Sarker, J. Appl. Phys. **105**, 07E510 (2009).

[22] M. E. Williams, H. Sims, D. Mazumdar and W. H. Butler, Phys. Rev. B **86**, 235124 (2012).

[23] Otto Mustonen, Sami Vasala, Ta-Lei Chou, Jin-Ming Chen and Maarit Karppinen, Phys. Rev. B **93**, 014405 (2016).

Chapter 6

Microscopic Origin Of Room Temperature Magnetism In Double Perovskites

6.1 Introduction

Magnetism in materials emerges because of the presence of non-vanishing spin moments which order at different atomic sites present in the material. This ordering of moments may be long-range or short-range, ferro, ferri or antiferromagnetic depending upon the type of magnetic interactions present in the system. Materials containing partially filled d orbitals of transition metals or partially filled f orbitals of rare earth atoms usually exhibit exotic magnetic properties [1,2]. Among the various crystalline forms of magnetic materials, compounds with the perovskite structure has been extensively studied recently [3]. An ideal cubic perovskite compound with chemical formula ABX_3 has a cation 'A' sitting at the body centered position twelve-coordinated with the anion 'X' sitting at the center of the edges of the cube. A cation 'B' sitting at the corners of the cube, hence separated by the anion atoms 'X' which is usually the oxygen atom. The cation 'A' may be a divalent or a trivalent cation and can be occupied by an alkali, alkali earth or rare earth elements. The 'B' site in perovskite crystal is occupied by the transition metal atoms forming a BX_6 octahedra which form a corner shared network in the crystal [4, 5]. Spontaneous

magnetization of materials known as ferromagnetism has always been great area of interest and it was in 1950 when the ferromagnetic behavior around room temperature of manganites ($AMnO_3$), a transition metal oxide with perovskite crystal structure, was studied by Jonker and Van Santen [6]. The ferromagnetic behavior of this compound was explained by the double exchange mechanism proposed by Zener [7]. The mixed valency of Mn atoms (Mn^{+3} and Mn^{+4}) in this compound allows delocalization of one e_g electron via oxygen atoms ultimately leading to the ferromagnetic alignment of spins at the Mn sites. It was followed by many other studies on the transition metal oxides to explore the possibility of ferromagnetism even at temperatures higher than room temperature with the similar operating mechanism [8–10].

The interplay between the spin and charge degree of freedom in transition metal oxides gives rise to interesting properties like magnetoresistance [11]. Dependence of resistivity of the system on an external magnetic field is known as the magnetoresistance of the system. Substantial decrease of electrical resistance with an applied external magnetic field is known as Colossal Magneto Resistance (CMR) [12] and it depends on both the temperature and the applied magnetic field. The significance of this effect is found to more when the system is close to its magnetic transition temperature [12]. Its application based device was first introduced by IBM in 1991 and since then materials with such effects are considered to be potential candidates for magnetic storage devices [13]. In this context, however, the role of manganites is limited by its low temperature and high magnetic field CMR response. Consequently, extensive studies towards finding materials with magnetic ordering temperature above room temperature have been done in the past and a new class of materials called double perovskites have been proposed.

Replacing every alternate B cation with another cation labelled B′ doubles the size of the perovskite unit cell and hence the name double perovskite (DP). The chemical formula for this type of compound can be given as $A_2BB'O_6$ where the two different transition metal atoms order alternately in all three dimensions. It then can also be realized in terms two perovskite sublattices ABO_3 and $AB'O_3$ formed by B and B′ transition metal atoms. The first report about the ferrimagnetic behavior above room temperature in this class of material was reported in Re-based double perovskite by Longo and Ward [14]. In this report, T_c of 316 K, 401 K, and 538 K were reported for Ba_2FeReO_6, Sr_2FeReO_6 and Ca_2FeReO_6 respectively. This was then followed by studies on Mo and W- based double perovskite oxides reported by Patterson in

1963 [15]. Kobayashi *et al.* [16] in 1998 reported a DP oxide Sr_2FeMoO_6 with magnetic ordering temperature (T_c) of 410 K. Interesting low field and above room temperature CMR response in this material was attributed to its half metallic fully spin-polarized electronic structure. Such high magnetic ordering temperature of many of these materials were really surprising because of the fact that in this class of materials, the magnetic lattice sites formed by Fe atoms is diluted with the nonmagnetic Mo/Re atoms and so the distance between closest Fe atoms is now $\sqrt{2}$ times larger than that in the Fe-based perovskite oxide. Hence, one expects weakening of the exchange interactions responsible for magnetism in these materials and consequently a reduced T_c. The antiferromagnetic ground state with small T_N of 37 K observed in the case of Sr_2FeWO_6 supported the fact that the exactly half filled one spin channel of Fe^{+3} ions ($3d^5$) separated by a large distance can only antiferromagnetically interact with a weak superexchange interaction [17]. However, with this assumption, the high T_C of compounds like Sr_2FeReO_6 and Sr_2FeMoO_6 could not be explained.

Various studies with *ab initio* and model Hamiltonian approaches have been done in the past to understand the microscopic origin behind this unusually high magnetic temperatures in the double perovskites. Sarma *et al.* [18] in their study based on band structure calculations, proposed that the interaction between d orbitals of the same symmetry at Fe and Mo sites in Sr_2FeMoO_6 causes an induced exchange splitting at the Mo site which was otherwise nonmagnetic. The resulting spin polarized Mo conduction bands are of hybridized character having contributions from Fe, Mo - d and oxygen p states and the one electron in the Mo $4d$ orbitals results in a net magnetic moment. This was also unusual because of the fact that the Mo-$4d$ orbitals have larger spatial extension. Hence, it is an atom with small Coulomb interaction and small Hund's exchange interaction which are not conducive for an atom to sustain a net magnetic moment. The coupling between Fe and this net Mo moment is antiferromagnetic in nature resulting in an overall ferromagnetic coupling between the Fe moments. A figure explaining this mechanism is shown in Fig. 6.1.

For the sake of clarity, only some of the bonding and antibonding energy levels are shown. As we can see that the interaction between Fe and Mo t_{2g} orbitals of the same spin, pushes the Mo-t_{2g} down spin levels lower in energy while the t_{2g} up spin levels are pushed higher in energy inducing an exchange splitting J_h^{mod}(Mo) at the Mo site. As shown in the figure, the antiferromagnetic

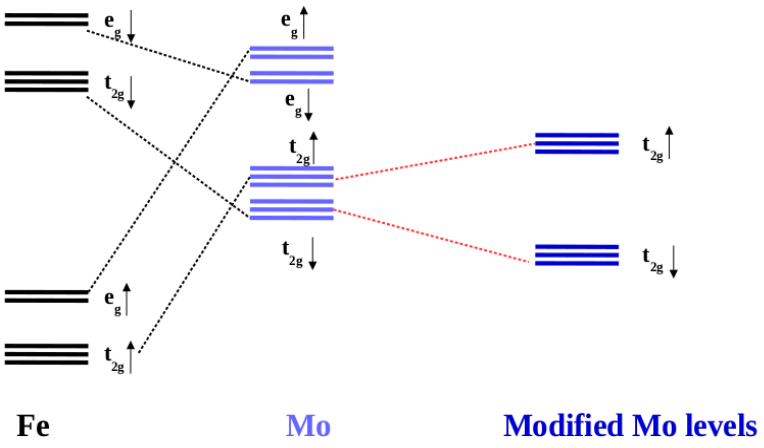

Figure 6.1: Schematic representing the modified energy levels at Mo site because of the Fe-Mo hopping interactions as proposed in Sarma *et al.* Ref. [18].

coupling between the Fe spins and the induced Mo spins results in a ferromagnetic coupling between the Fe atoms explaining the high T_C of this material.

A widely used microscopic model to describe the double perovskite systems is an effective Kondo-like model [19]. Within this model, the localized majority spins at the Fe site are approximated as a single spin with $S = \frac{5}{2}$ interacting antiferromagnetically with the itinerant electron spin by an effective Kondo-like term. In a study by Phillips *et al.* [20], they considered a tight binding Hamiltonian for the kinetic energy of a single electron part and an effective Kondo-like term. The hopping interactions were considered between Fe-Mo, Mo-Mo and Fe-Fe t_{2g} orbitals in the minority spin channel. The Kondo-like term with the localized spin ($\vec{S}$) at the Fe site interacted via strong antiferromagnetic interaction with the conduction electron spin ($\vec{\sigma}$) was given by -$J\sum_{i,\alpha,\beta} \vec{S}_i \cdot c^{\dagger}_{i\alpha}\vec{\sigma}_{\alpha\beta}c_{i\beta}$. In the large J limit, the charge fluctuations (d^5(Fe)$\longleftrightarrow$ d^6(Fe)) into the minority spin channel was allowed within this model as the energy cost for the fluctuations in Fe majority spin channel was very large. Using the dynamical mean field theory (DMFT), the calculated magnetic ordering temperature of Sr_2FeMo/ReO_6 was found to be lower than the experimentally observed value by a factor of ~ 4. In addition to that, this study also failed to obtain the experimentally observed trend of increase in T_c with increase of electron density at the nonmagnetic site. They guessed that the T_c would be enhanced substantially if the character of the conduction electrons is more Fe-like. Another mentioned possible route for

the enhancement of the calculated T_c was by including important hopping interactions of the minority spins over several sites in the model. Many other attempts [21, 22] considering similar kind of Hamiltonian have also failed to explain the high magnetic ordering temperature when there were two electrons on the nonmagnetic atom as in Sr_2FeReO_6.

The study by Brey *et al.* [23], considered a similar t_{2g} only model with additional approximation that large localized spins (5/2) on Fe sites are classical and are described by angle θ_i. The hopping terms in this model only contain Fe-Mo and Mo-Mo hopping and neglected the Fe-Fe hopping interaction as they expected it to be small. Because of the large Kondo-like exchange interaction J, the conduction electrons on the Fe sites follow the classical localized spin (S=5/2). In the limit J $\rightarrow\infty$, the itinerant electron spin would either be parallel or antiparallel to localized Fe spin. Within a mean field study, they deduced an effective Heisenberg model and show that there are competing degenerate ferromagnetic and antiferromagnetic channels which causes the suppression of T_c for large electron density as found in the previous theoretical studies also. They suggested that this degeneracy can be lifted by considering a Hubbard U term on the Mo/Re site which penalizes the double occupancy of nonmagnetic sites, consequently favoring the ferromagnetic channel. Within this study, they qualitatively obtained the experimentally observed enhancement of T_c with an increase of electron density.

In the context of the previous studies, we went on to reexamine the issue of high temperature magnetism in Sr_2FeReO_6 using *ab initio* as well as a model Hamiltonian approach. First, the *ab initio* band structure calculations were performed and electron correlation effects on Fe as well as on Re sites were introduced within the GGA+U technique. Considering a U of 2.5 eV on the Fe site, the ground state is found to be ferromagnetic. The magnetic exchange interaction strengths (J's) between the magnetic (Fe) atoms were calculated using an inverse Fourier transform method. Using classical Monte Carlo (MC) simulation technique employing an extended Heisenberg model, T_c of the system is estimated. In the first case, when their was no U on the Re site, we found that the nearest neighbor exchange interaction J_1 is ferromagnetic while the second neighbor exchange interaction J_2 is antiferromagnetic contrary to what is believed in literature [24]. J_3 and J_4 are negligibly small when compared to J_1, J_2. With these exchange interaction strengths, the estimated T_c within the Monte Carlo simulation study was much lower ($\sim$ 285 K) than the experimental value of 401 K. Taking a clue from Brey *et al.*, we

then considered a U of 1 eV on the Re-d states and again calculated the exchange interaction strengths. We found that the J_1 got enhanced by almost a factor of ~ 2. Most surprisingly, J_2 changes its sign from being antiferromagnetic in the no U case to ferromagnetic in the present case when a U of 1 eV is considered at the Re site. Using a U(Fe) = 2.5 eV and U(Re) = 1.0 eV we find the magnetic ordering temperature to be 395 K which is reasonably close to the experimentally observed value. Within *ab initio* density of state calculations, the ferromagnetic ground state is found to be half-metallic. The Re moments are induced in nature and are antiparallel to Fe moments. With an application of U on the Re site, we found no substantial effect in the density of states for the ferromagnetic configuration which could explain the gain in stability in this case. However, examining the density of states in a competing antiferromagnetic configuration we found that the U(Re) played the role on inducing an exchange splitting of the Re d states. Thus by destabilizing the antiferromagnetic state, one found that one could increase the ferromagnetic stability. In order to test this hypothesis we set up a multiband Hubbard Hamiltonian to describe the system. Introducing an exchange splitting (J_h) on Re was found to enhance the stability of the ferromagnetic state.

6.2 Methodology

Using a plane wave pseudopotential implementation of density functional theory using PAW potentials [28, 29] implemented in VASP, the electronic and magnetic properties of SFRO has been calculated. For the exchange correlation functional, the GGA PW91 [30,31] approximation has been used. The effects of electron-electron correlation on the transitional metal d electrons were considered within the GGA+U scheme using the Dudarev *et al.* formalism [32]. In our calculations, a U of 2.5 eV on the Fe-d states while U of Re-d states varied to 0, 1 and 2 eV. k-mesh of $8 \times 8 \times 8$ and cutoff energy of 500 eV for the plane wave basis have been used. The inter atomic exchange interactions strengths J's were determined using the frozen magnon approach [33–36]. In this approach, total energy corresponding to each spin spiral state was calculated within the noncollinear spin implementation in Viena *Ab Initio* Simulation package (VASP) [37]. Here each spin spiral state vector $\vec{q}$ corresponds to a magnetic configuration as

denoted by the unit spin vector,

$$\vec{s_i} = (\sin\theta\cos(\vec{q}\cdot\vec{R_i}), \sin\theta\sin(\vec{q}\cdot\vec{R_i}), \cos\theta) \tag{6.1}$$

Here $\vec{R_i}$ is the position of the atom whose direction is represented by vector $\vec{s_i}$ and θ is the polar angle made with the z-axis. Assuming the spins at the Fe sites to be classical localized ones, we mapped our results onto an extended Heisenberg model as,

$$H = -\frac{1}{2}\sum_{ij} J_{ij}\vec{s_i}\cdot\vec{s_j} \tag{6.2}$$

In the above equation, J_{ij} are the exchange interaction strengths between the Fe spins at site i and j. The magnitude of spins are absorbed in the J-term. It is clear that in this model, a positive and negative J values imply ferromagnetic and antiferromagnetic exchange interactions respectively. Hence, corresponding to each $\vec{q}$ values, one has the total energy E($\vec{q}$) in terms of the J($\vec{q}$) which is related to the exchange interactions via Fourier transformation as,

$$J(\vec{q}) = \sum_{i\neq 0} J_{0i} e^{i\vec{q}\cdot\vec{R_{0i}}} \tag{6.3}$$

For simplicity, in our calculations, we confined spins to be lying in the xy-plane and hence $\theta = 90°$. After performing the inverse Fourier transform, we obtain the real space exchange parameters as,

$$J_{0i} = \frac{1}{N}\sum_{\vec{q}} J(\vec{q}) e^{-i\vec{q}\cdot\vec{R_{0i}}} \tag{6.4}$$

Thus the calculated spin wave spectra along various various high symmetry directions with varying $\vec{q}$ has been calculated and the results were fitted using a least squared error minimization procedure to estimate the exchange parameters with the best fit. The Boltzmann weight factor $e^{-\beta\Delta E}$ was considered while estimating the exchange parameters to take care of the fact that statistical weight corresponding to large angles between the spins are low in the frozen magnon states. Here $\beta = 1/k_B T$ where T is the ferromagnetic transition temperature of 401 K for SFRO and $\Delta E = E(\vec{q}) - E(0)$. This analysis was done for both the case when their was no U on the Re sites and also with a U(Re) = 1 eV while the U on Fe sites was kept fixed at 2.5 eV.

With the help of these exchange interactions, we calculated the ferromagnetic transition temperature (T_c) using a classical Monte Carlo (MC) [38] method. In this technique, we first set up the face centered lattice of Fe atoms in SFRO and consider a system size of 16 × 16 × 16. We consider localized classical interacting spins of Fe atoms through the various exchange interactions (J's) and the considered Hamiltonian to describe this system was an extended Heisenberg model. During a single MC run, using a random number generator, random orientation ($\vec{e_i}$) of spin at i-th site is considered and the energy of the system is calculated using the Heisenberg model. Then a new random orientation of spin ($\vec{e_i'}$) is created and the system energy was again calculated. If the energy associated with this new random orientation ($\vec{e_i'}$) is lower than that of the ($\vec{e_i}$), then we accept ($\vec{e_i'}$). Else, Metropolis algorithm [39] is employed to decide on whether to accept or reject ($\vec{e_i'}$). This procedure performed over all the lattice sites i is one Monte Carlo step. The magnetization M(T) per spin was calculated only after bringing the system into thermal equilibrium. Total 5 × 10^5 Monte Carlo steps were used in these calculations and results were found to be well converged with respect to the system size as well as the MC steps.

The multiband Hubbard Hamiltonian considered for the microscopic understanding of the system is given as,

$$
\begin{aligned}
H = & \sum_{i,l,\sigma} \epsilon_d^f d_{il\sigma}^\dagger d_{il\sigma} + \sum_{i,l,\sigma} \epsilon_d^m d_{il\sigma}^\dagger d_{il\sigma} + \sum_{i,l,\sigma} \epsilon_p p_{il\sigma}^\dagger p_{il\sigma} + \sum_{i,l,\sigma} \epsilon_s s_{il\sigma}^\dagger s_{il\sigma} \\
& - \sum_{i,j,l_1,l_2,\sigma} \left(t_{i,j,pd_f}^{l_1 l_2} d_{il_1\sigma}^\dagger p_{jl_2\sigma} + \mathbf{H.c.} \right) - \sum_{i,j,l_1,l_2,\sigma} \left(t_{i,j,pd_m}^{l_1 l_2} d_{il_1\sigma}^\dagger p_{jl_2\sigma} + \mathbf{H.c.} \right) \\
& - \sum_{i,j,l_1,l_2,\sigma} \left(t_{i,j,pp}^{l_1 l_2} p_{il_1\sigma}^\dagger p_{jl_2\sigma} + \mathbf{H.c.} \right) - \sum_{i,j,l_1,l_2,\sigma} \left(t_{i,j,sd_f}^{l_1 l_2} d_{il_1\sigma}^\dagger s_{jl_2\sigma} + \mathbf{H.c.} \right) \\
& - \sum_{i,j,l_1,l_2,\sigma} \left(t_{i,j,sd_m}^{l_1 l_2} d_{il_1\sigma}^\dagger s_{jl_2\sigma} + \mathbf{H.c.} \right) \\
& + \sum_{\alpha\beta\gamma\delta,\sigma_1\sigma_2\sigma_3\sigma_4} U_{dd,f}^{\alpha\beta\gamma\delta} d_{\alpha\sigma_1}^\dagger d_{\beta\sigma_2}^\dagger d_{\gamma\sigma_3} d_{\delta\sigma_4} \\
& + \sum_{\alpha\beta\gamma\delta,\sigma_1\sigma_2\sigma_3\sigma_4} U_{dd,m}^{\alpha\beta\gamma\delta} d_{\alpha\sigma_1}^\dagger d_{\beta\sigma_2}^\dagger d_{\gamma\sigma_3} d_{\delta\sigma_4}
\end{aligned}
$$

where $d_{il\sigma}^\dagger$ ($d_{il\sigma}$) creates (annihilates) an electron with spin σ in the lth d orbital on transition metal site in the ith unit cell while $p_{il\sigma}^\dagger$ ($p_{il\sigma}$)/$s_{il\sigma}^\dagger$ ($s_{il\sigma}$) creates (annihilates) an electron with spin

σ in the lth p/s orbital on oxygen atom in the ith unit cell. Here the index f and m represent the Fe and Re sites respectively. The hopping interaction strengths (t) were kept fixed at the values obtained from fitting the nonmagnetic *ab initio* band structure of Sr_2FeReO_6 within a tight binding model having Fe, Re-d and O p states in the basis. These hopping interactions were parametrized in terms of Slater-Koster parameters [40] dpσ, dpπ, dsσ. The onsite energies were however varied, though the same values were taken for both spin channels. The exchange splitting was a part of the Coulomb interaction term considered on both Fe and Re. The Coulomb matrix elements were parameterized in terms of the Slater-Condon integrals [27] F^0, F^2 and F^4 in order to take of its rotationally invariant nature and there values were determined from atomic Hartree-Fock calculations. F^0 was varied and used to determine the multiplet averaged Coulomb interaction U though screening of it due to solid state effects substantially reduce its magnitude. As the Hund's exchange interaction strength is related to them by the relation $J_h = \frac{F^2+F^4}{14}$, a reduction factor was used to these interaction strengths to get the desired exchange splitting observed in the *ab initio* spin polarized calculations. For Fe d orbitals, J_h value 0.8 eV was considered while at the Re site it is varied from a minimum of 0.24 eV to 0.4 eV.

The four fermion Coulomb interaction terms in Eq.(1.5) were decoupled using a mean field method as the Hamiltonian containing these terms is difficult to solve exactly. A mean field decoupling scheme was employed to solve this Hamiltonian which is discussed in Chapter 2 of this thesis in great detail. The expectation values of the order parameters entering the mean field decoupled Hamiltonian were determined self-consistently till an energy convergence of 10^{-5} eV was achieved. Total energy and density of states were calculated using tetrahedron method of integration for a $10 \times 10 \times 10$ k-mesh.

6.3 Results and Discussions

We first discuss the studies and findings obtained with the *ab initio* approach followed by the results obtained with the model Hamiltonian approach.

6.3.1 *Ab initio* Study

An ordered double perovskite structure is the one in which B and B′ are two different transition metal sites arranged alternately forming BO_6 and $B'O_6$ octahedra. The crystal structure of Sr_2FeReO_6 is simple cubic with space group Fm-3m. The experimental and theoretically optimized structural information is given in Table 6.1. As one can find in the simple structure of SFRO, all the Fe-O-Re bond lengths are 180° while all the Fe-O or Re-O bondlengths are identical within the respective octahedra as tabulated in Table 6.1. There was no substantial change in the experimentally observed lattice constants found after structural optimization. However, there is substantial change in Fe-O and Re-O bond lengths after the optimization. We use this optimized structure in our further calculations.

Structural details	Experimental	Theoretical
Space group	Fm-3m	Fm-3m
a = b = c (Å)	7.888	7.890
$\alpha = \beta = \gamma$ (°)	90	90
Positions		
Sr	0.25 0.25 0.25	SAE
Re	0 0 0	SAE
Fe	0.5 0.5 0.5	SAE
O	0.216 0 0	SAE
Bond lengths (Å)		
Re-O	1.70	1.94
Fe-O	2.24	2.01
Bond angles (°)		
Fe-O-Mo	180	180
Cell volume ($Å^3$)	490.8	491.17

Table 6.1: The experimental [50] and optimized/theoretical structural details for Sr_2FeReO_6. (SAE= Same as experimental vealue)

6.3.2 Spin-Wave Spectra, Estimated J's and T_c

To develop an understanding of the high magnetic ordering temperature of this system, the magnon dispersions were calculated along various symmetry directions in the Brillouin zone

of SFRO. The high symmetry points considered in these calculations are Γ(0,0,0), X($\frac{1}{2}$,0,$\frac{1}{2}$), W($\frac{1}{2}$,$\frac{1}{2}$,$\frac{1}{2}$) and L($\frac{1}{2}$,$\frac{1}{4}$,$\frac{3}{4}$). These coordinates are characterized in terms of reciprocal lattice vectors. As discussed earlier, each $\vec{q}$ represents a magnetic configuration of the system. Using the frozen magnon approach, these were calculated for a U of 2.5 eV on the Fe d states. At first, no U was used on the Re d states. The calculated magnon dispersions are shown in Fig 6.2.

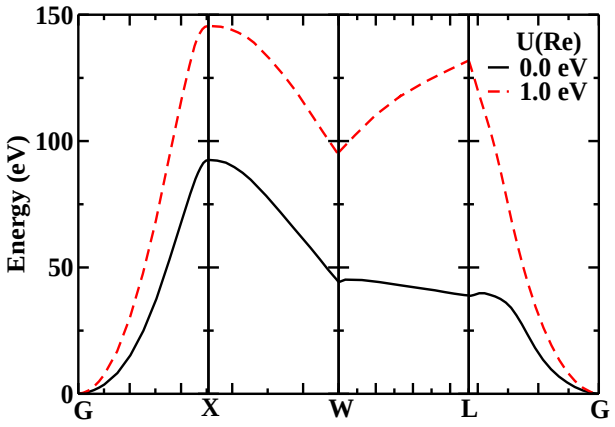

Figure 6.2: The magnon dispersion plot for SFRO as a function with U(Fe) = 2.5 eV and U(Re) = 0 and 1 eV. The G point energy is the ferrimagnetic energy which gets more stabilized with application of U of 1 eV on the Re site.

Clearly, Γ point, which represents the ferromagnetic state has the lowest energy which is in agreement with the experimental findings. The value of magnetic moment at Fe and Re site are 3.9 μ_B and -0.95 μ_B respectively. The induced moment on the Re site is opposite to the Fe moments and since there is no U on Re-d states, it is purely originated by the Fe-Re hopping as described in Ref [18]. This is evident from the density of states calculated for a perfectly antiferromagnetic configuration. It was found that in this case there was no exchange splitting of the Re d states, which one would find if there was a component emerging from an intrinsic exchange splitting.

The interatomic exchange interaction strengths (J's) are then estimated employing an inverse Fourier transformation method as discussed in the methodology section. A plot of different J's as a function of nearest neighbor distance is shown in Fig 6.3.

We found that in this case when there is no U on the Re-d states, J_1 which is the most dominant one was found to be 10.9 meV and is ferromagnetic while J_2 is -5.1 meV and is antiferromagnetic

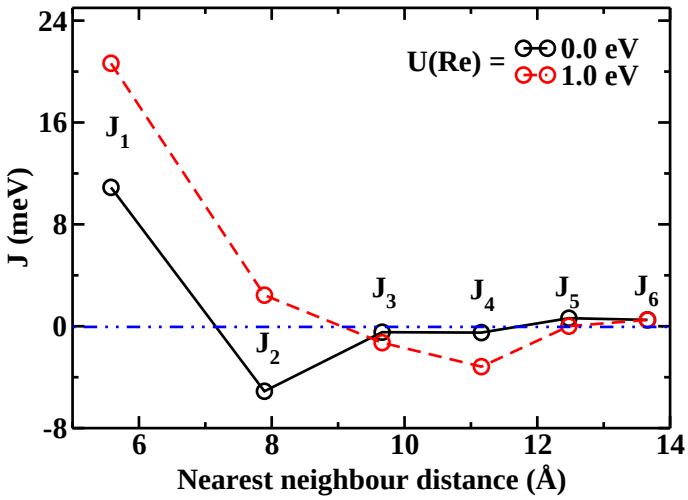

Figure 6.3: Inter atomic exchange interaction parameters, J, of SFRO as a function of the distance between the Fe atoms (in units of Å).

in nature. All other J's are negligibly small. A schematic showing the first four exchange interactions and the pathways they represent is shown in Fig 6.4.

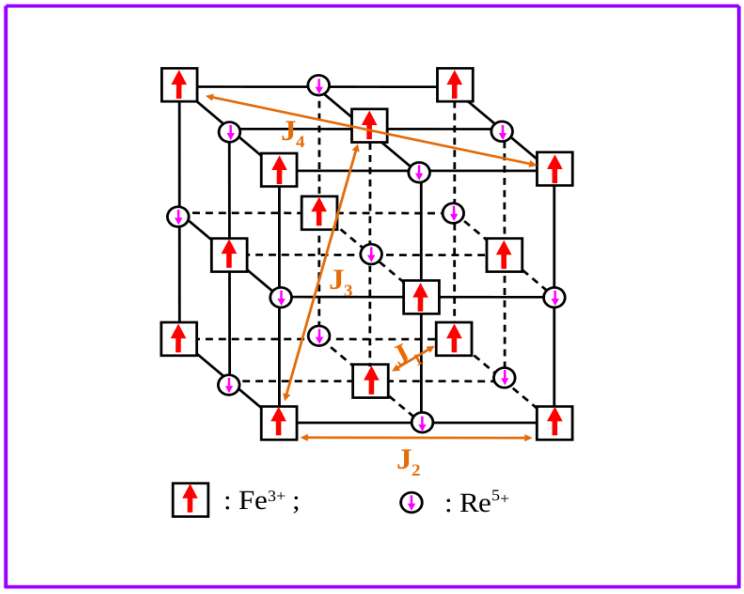

Figure 6.4: A schematic to show the first four inter atomic exchange interaction parameters (J's) in the simple cubic lattice of SFRO.

One should mention here that the separation between the Fe atoms connected via J_1, J_2, J_3 and J_4 is $\sim$ 5.58 Å, 7.89 Å, 9.66 Å and 11.16 Å respectively. Using a Monte-Carlo simulation method, the estimated magnetic transition temperature (T_c) with these values of exchange interactions is 285 K, much less than the experimental value.

As hypothesized by Brey *et al.*, application of U on the nonmagnetic Mo site will penalize double occupancy. It consequently leads to the ferromagnetic state being favored. Taking a clue from this hypothesis, we applied a U of 1 eV on the Re-d states while a U on Fe-d states was kept fixed at the value of 2.5 eV and recalculated the magnon spectra shown in Fig 6.2 (red dashed lines). A plot of estimated values of J's in this case is shown in Fig 6.3. A clear enhancement in the stability of the ferromagnetic configuration can be found in this case when compared to the previous case of no U on Re. It can also be viewed as if the antiferromagnetic states are now destabilized with the application of U on the Re-d states. The effect of U on the Re site is also manifested in the exchange parameters. An analysis of the estimated J's in this case yields mainly two important points. First is the enhancement in the magnitude of the most dominant nearest neighbor ferromagnetic exchange interaction strength J_1. Its value $\sim$ 21 meV is nearly doubled with a U(Re) = 1 eV from its value in the absence of U on Re. Most interestingly, J_2 which was antiferromagnetic in the previous case is now found to be ferromagnetic in the present case. The estimated T_c with this new set of exchange interaction strengths is 395 K which is in reasonable agreement with the experimental value of 401 K. The magnetic moment on the Re site is enhanced to -1.04 μ_B in this case while it is the same for the Fe atoms when there was no U on the Re-d states. A plot of the normalized magnetic moment variation as a function of temperature in both the cases when there is no U on Re and when a U of 1 eV is considered on the Re-d states is shown in Fig 6.5. There is indeed a clear enhancement of in the T_c.

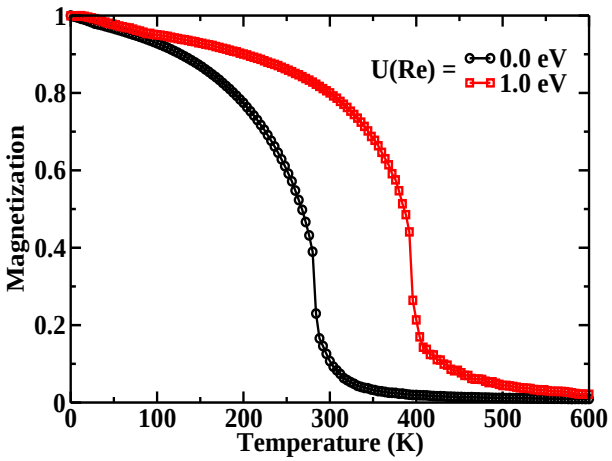

Figure 6.5: Variation of magnetization as a function of temperature calculated for U(Fe) = 2.5 eV and U(Re) = 0 and 1 eV with Monte Carlo simulation for SFRO.

To explain this behavior, we went to examine the Fe and Re atom projected density of states in both the cases with and without a U on Re-d states for the ferromagnetic ground states, a plot of which is shown in left panel of Fig. 6.6. For the sake of better understanding we additionally consider the case when a U of 2 eV is considered on Re-d states. The large exchange splitting at the Fe site and an induced small exchange splitting at Re site is evident from the plot. As we can see in the up spin channel, Fe states are fully occupied verifying the $3d^5$ ionic configuration of Fe while the Re states are unoccupied and are $\sim$ 0.6 eV above the Fermi level. With the application of U on Re, the unoccupied Re-up spin states are pushed up away from the Fermi level. A U of 1 eV on Re pushes the Re d states by $\sim$ 0.25 eV from its position for the case when there was no U. In the down spin channel, there is hardly any significant change in Fe and Re-d density of states with the variation of U on the Re site. They are found to be pinned to their positions in the absence of U. Thus, the small shifts in the Re-up spin density of states above the Fermi energy as function of U on the Re d states alone is therefore insufficient to describe the substantial gain in the stability of the ferromagnetic ground state found by examining the magnon dispersion shown in Fig. 6.2. For example, the gain is $\sim$ 50 meV at the X and W points while it is even more than $\sim$ 85 meV at the L-point over the $U = 0$ values.

In order to get a reasonably convincing picture of the underlying physics and taking some clues from our previous findings, we went on to examine the density of states of the closest competing antiferromagnetic state.

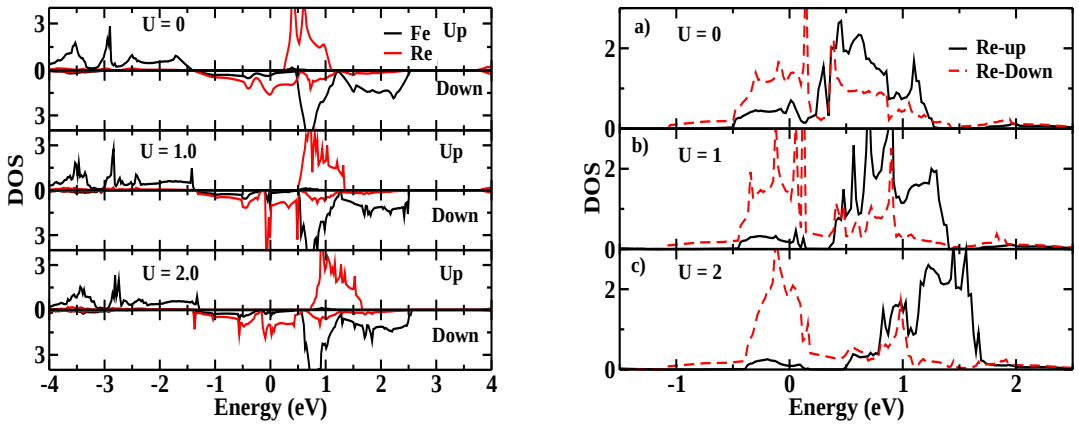

Figure 6.6: Atom projected Fe,Re-d density of states plots from *ab initio* calculations for Sr_2FeReO_6. The plot in the left is obtained after considering ferromagnetic configuration of Fe spins while the plot in the right is from the closest competing antiferromagnetic state. The zero of energy is the Fermi energy.

In the ferromagnetic state, the Fe atoms are antiparallel to the first nearest neighbor Re atoms. We consider alternate antiferromagnetic configurations in which we have flipped the spin of two out of the six Fe nearest neighbors of a Re atom and made them ferromagnetic. As this is a collinear antiferromagnetic configuration with the smallest number of spins around Re flipped, one would expect this to be the closest lying antiferromagnetic excited states.

The atom projected density of states for Fe and Re atoms are then calculated by varying the U on the Re site. The calculated density of states for the Fe-d states has almost similar features as shown for the ferromagnetic configuration in Fig. 6.6. Similar to the ferromagnetic case, these states are unaffected by the application of U on Re atom and hence are not shown here. It is the Re-d density of states shown in the right panel of Fig. 6.6, which have the most dramatic effects in this antiferromagnetic configuration with application of U on it. In the antiferromagnetic state, when their is no U on the Re site, both the spin channels are found to be contributing at the Fermi level as shown in the right panel (a) of Fig. 6.6. The induced exchange splitting at the Re site, which was present in the ferromagnetic case has reduced substantially. This provides pathways for both, the ferromagnetically as well as antiferromagnetically coupled spins. This explains the case of reduced magnetic transition temperature.

The Re-up spin channel gets substantially depleted at the Fermi level with the application of U on Re-d states as shown in the right panel (b) of Fig. 6.6. The majority weight of the Re-up spin states is now much above the Fermi level bringing an effective exchange splitting at the Re site. Because of this the energy gain from delocalization of antiferromagnetically coupled Fe spins is significantly reduced. The exchange splitting at the Re site, further enhances the energy gain for ferromagnetically coupled spins. This is manifested in terms of enhanced J_1 and a ferromagnetic J_2 in this case and consequently a higher T_c. This picture gets even more clear by looking at Re density of states with a U of 2 eV at its d states where the effects are more pronounced. A comparison of the stability of the ferromagnetic states with respect to this antiferromagnetic state as a function of U(Re) is tabulated in Table 6.2.

	AFM-FM (eV)	
U_{Re} (eV)	Sr_2FeReO_6	Sr_2FeMoO_6
0.0	0.085	0.129
1.0	0.138	0.143
2.0	0.175	0.158

Table 6.2: Change in stability of the ferromagnetic state calculated with respect to closest competing antiferromagnetic state as function of U on the Re/Mo-d states for Sr_2FeReO_6 and Sr_2FeMoO_6 double perovskites.

6.3.3 Model Hamiltonian Study

In order to explicitly understand the role of the exchange splitting at the nonmagnetic Re site, we further went on to develop a simple model which can define this system correctly. For this purpose, we start with calculating the *ab initio* atom projected density of states within a non-magnetic calculation for Sr_2FeReO_6 and is given in Fig. 6.7. The Fe d states are found in the energy window from -2 eV to 1 eV. The octahedral field of the six oxygens which are the nearest neighbors of Fe lift the degeneracy of the d orbitals and one has the t_{2g} orbitals contributing in the energy window from -2 to -0.5 eV. The e_g states contribute in the energy window from ~ 0 to 1 eV.

We find a similar degeneracy lifting of the d states on Re, with the t_{2g} states contributing in the energy window from ~ 0 to 0.5 eV.

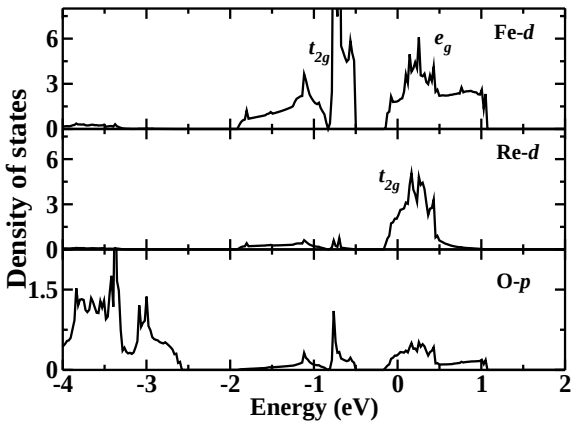

Figure 6.7: The Fe d, Re d and oxygen p projected partial density of states for non-magnetic Sr_2FeReO_6 from *ab initio* calculations. The zero of energy is the Fermi energy.

Examining the O p states, one finds that their primary contribution is below $\sim$ -3 eV and extend to -8 eV below the Fermi level. There is a small admixture of the O p states in the energy window contributed primarily by the Fe and Re d states. This arises from p-d hybridization and one finds that the contributions are larger for the Fe e_g states as well as the Re t_{2g} states which have the larger hopping matrix elements associated with them. Surprisingly we find the energy window over which the Fe t_{2g} states contribute comparable with that in which Fe e_g states contribute. This seems surprising and could emerge from the smaller energy denominator for the delocalization of an electron in the Fe t_{2g} states via the Re t_{2g} states than the Fe e_g states via the levels with the same symmetry on Re.

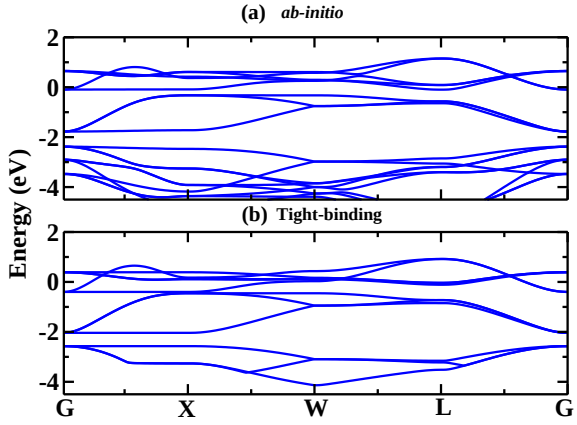

Figure 6.8: The non-magnetic band dispersions from (a) *ab initio* , (b) tight binding calculations with Fe d, Re d and O s, p basis states along various symmetry directions in Brillouin zone of Sr_2FeReO_6. The zero of energy is the Fermi energy.

The *ab initio* band dispersions along various symmetry directions for nonmagnetic Sr_2FeReO_6 are shown in Fig. 6.8 in the energy window -4 to 2 eV. As Fe d, Re d and O p states were found to contribute in this energy window, we included these states in the basis of tight binding model considered. We also included the s states on the oxygen as discussed in the methodology section. The parameters entering the tight binding Hamiltonian should reproduce the band structure from the *ab initio* calculations. A least square error minimization procedure was used. The best fit parameters are given in Table 6.3. The $dp\pi$ interactions between the Fe d and O p states are significantly enhanced compared to a ratio of 0.5 for $dp\sigma/dp\pi$ interactions that one usually expects explaining partially the similar bandwidths that we find for Fe t_{2g} and Fe e_g states.

Onsite energies				Fe-O			Re-O			O-O	
Fe-d		Re-d	O-p	$dp\sigma$	$dp\pi$	$ds\sigma$	$dp\sigma$	$dp\pi$	$ds\sigma$	$pp\sigma$	$pp\pi$
t_{2g}	e_g	t_{2g}									
2.46	3.34	3.90	0.68	1.90	-1.495	-1.44	3.05	-1.28	-0.76	0.75	-0.164

Table 6.3: Onsite energies and various hopping interaction strengths (in eV) parameterized in terms of Slater-Koster parameters obtained by fitting *ab initio* band structure of non-magnetic Sr_2FeReO_6 in a tight binding model with Fe, Re d and O s, p states in the basis.

$ds\sigma$ interactions control the crystal field splitting between the t_{2g} and e_g orbitals and are found to be considerable for the Fe d states also, compared to the Re d states as the Re e_g states were not included in the fitting. Examining the onsite energies, one finds that one has the Fe t_{2g} states, Fe e_g states and then the Re t_{2g} states as expected.

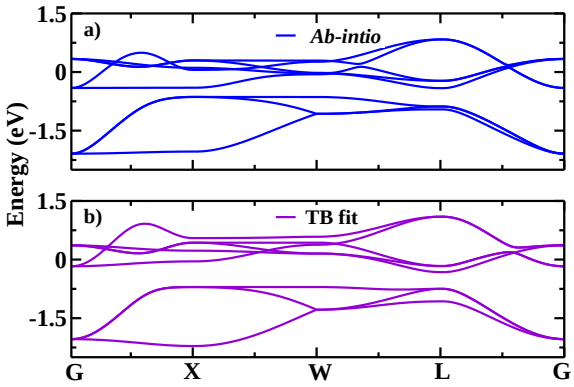

Figure 6.9: The non-magnetic band structure from (a) *ab initio* , (b) tight binding calculations with only Fe and Re d basis states, plotted along various symmetry directions in Brillouin zone of Sr_2FeReO_6. The zero of energy is the Fermi energy.

The charge transfer energy between the O p states and Fe t_{2g} states is small but positive. In order to examine the role of explicitly including the O p states in the basis, especially when the charge transfer energy is so small, a mapping was carried out onto a d-only model. The parameters found to give the best fit of the *ab initio* band structure shown in Fig 6.9(a) are given in Table 6.4. The tight binding band structure calculated for the best fit parameters are given in Fig. 6.9(b).

As is evident, we include explicitly the Fe d and Re d states while constructing the tight binding Hamiltonian with d-d interactions. Interestingly we find that the Re t_{2g} levels lie in between the Fe t_{2g} and Fe e_g levels. This is because in the effective d-only model, we are approximating

the positions of the d levels to their positions after their interaction with oxygen. The matrix elements for Fe e_g and O p interactions are larger, resulting in larger shifts compared to the interaction between Re t_{2g} and O p states. This leads to negative energy difference between the Fe e_g and the Re t_{2g} states.

Onsite energies			Fe-Fe			Fe-Re			Re-Re		
Fe-d		Re-d	$dd\sigma$	$dd\pi$	$dd\delta$	$dd\sigma$	$dd\pi$	$dd\delta$	$dd\sigma$	$dd\pi$	$dd\delta$
t_{2g}	e_g	t_{2g}									
4.45	6.39	5.10	-0.05	0.05	-0.004	-0.866	0.298	0.0	-0.199	0.008	-0.02

Table 6.4: Onsite energies and various hopping interaction strengths (in eV) parameterized in terms of Slater-Koster parameters obtained by fitting *ab initio* band structure of non-magnetic Sr_2FeReO_6 in a tight binding model with only Fe and Re d states in the basis.

In order to verify if the placing of the Re t_{2g} levels below the Fe e_g levels is not an artifact of the fitting procedure, a similar analysis was carried out for a d only mapping using maximally localized wannier functions [43] for the radial parts of the basis functions. A comparison of the *ab initio* band structure and the fitted band structure are given in Fig.6.10. Here we find that the fit is reasonable which gives us confidence in examining the onsite energies. We find that the difference between the Re t_{2g} and the Fe e_g levels is negative, $\sim$ -0.7 eV in agreement with what we had earlier.

In order to determine the appropriate model, a multiband Hubbard model is considered with the same value of U and the electronic structure for a given set of parameters is calculated using a mean field decoupling scheme for the four Fermion terms. The hopping interaction strengths are kept fixed at the values obtained by fitting the nonmagnetic band structure.

We consider the charge fluctuations at the Fe and Re sites as,

$$\Delta_{Fe\leftrightarrow O} = E_f(d^6\bar{L}) - E_i(d^5L^0) = \epsilon_d - \epsilon_p + 5U^{Fe} \tag{6.5}$$

$$\Delta_{Re\leftrightarrow O} = E_f(d^3\bar{L}) - E_i(d^2L^0) = \epsilon_d - \epsilon_p + 2U^{Re} \tag{6.6}$$

Here ϵ_d and ϵ_p are the onsite energies of Fe/Re-d and O-p orbitals respectively. Hence Δ was kept fixed with $U_{Fe/Re}$ by changing the onsite energies in accordance to the above equations. The

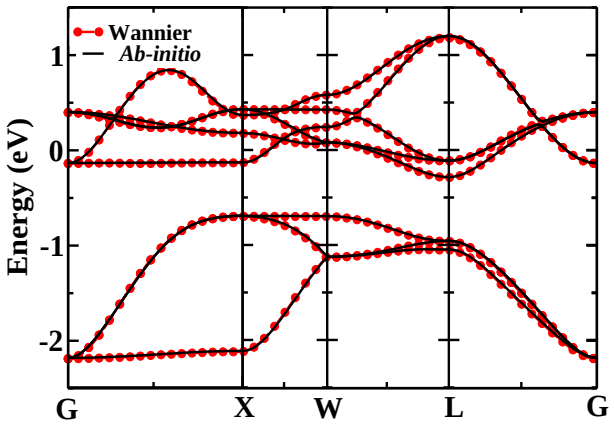

Figure 6.10: The non-magnetic *ab initio* band structure fitted with tight binding bands considering Fe and Re d orbitals in the basis. The radial part of the tight binding basis functions correspond to maximally localized Wannier functions. The zero of energy is the Fermi energy.

J_h are varied till a good description of the *ab initio* density of states is obtained. A comparison is shown in Fig 6.11.

A J_h of 0.8 eV was considered on Fe and this gave a good description of the *ab initio* density of states. Additionally the charge transfer energy between both Fe and Re with oxygen were found to be 0.85 and 3.5 eV, both positive. Additionally a U of 0.26 eV and a small J of 0.24 eV was used on the Re states to get the half-metallic character of the density of states. As discussed previously with the *ab initio* results, a U on the Re-d states introduces an effective exchange splitting on the same, resulting in a gain for the ferromagnetic ground state. We probe this fact independently using the model Hamiltonian that we have developed. We calculate the stability of the ferromagnetic ground state with respect to the previously considered antiferromagnetic state with variation of exchange splitting (J_h) at the Re site.

The calculations were done with a fixed U of 0.4 eV of the Re-d states and keeping all the other parameters the same to their previous values. The obtained results are tabulated in Table 6.5. As we can see that with an increase in J_h from 0.24 eV to 0.35 eV at the Re site, the stability of the ferromagnetic state is indeed enhanced by $\sim$ 40 meV. This supports our previously given explanation for increase in the stability of ferromagnetic state with application of U on the Re site as it causes an effective exchange splitting at the Re site. This suggests a route to enhance the T_c of these double perovskite systems by using magnetic atoms at the B$'$ site.

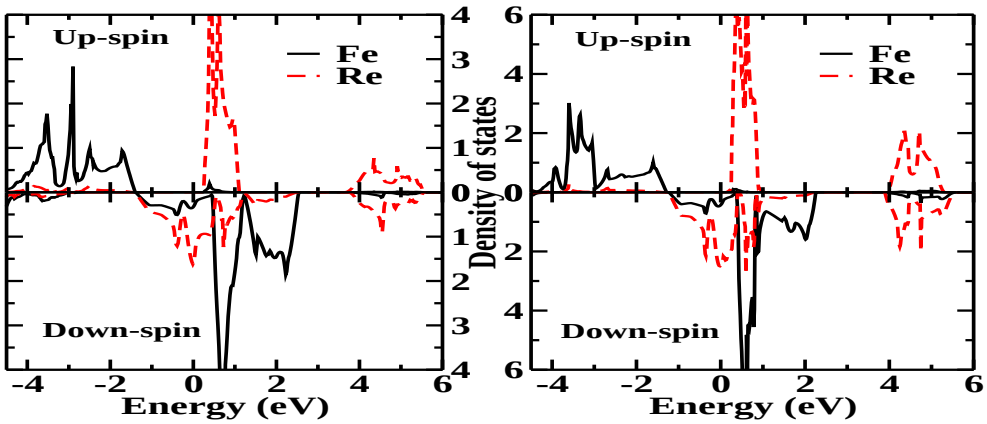

Figure 6.11: Atom projected density of states plots from *ab initio* calculations (left) and model Hamiltonian calculation (right) with Fe and Re d states in the basis. The zero of energy is the Fermi energy.

J_h (eV)	AFM-FM (eV)
0.24	0.134
0.35	0.173
0.50	0.186

Table 6.5: Within a multiband Hubbard model, calculated change in stability of the ferromagnetic state with respect to closest competing antiferromagnetic state as function of exchange splitting at the Re site for Sr_2FeReO_6.

Finally, a comparison with a similar system Sr_2FeMoO_6 (SFMO) has been drawn to explain the role two electrons present in the Re-d orbitals (Re^{5+}) in the case of SFRO. Change in the ferromagnetic stability with respect to the same antiferromagnetic configuration is calculated for SFMO and the results are tabulated in Table 6.2. As one can see that in the case of SFMO, the stability of ferromagnetic state increases when a U of 1 eV is applied at the Mo site, but the gain is much less than that of the SFRO. While in the case of SFRO this gain was $\sim$ 50 meV, here it is only 14 meV. Further increase of U at the Re site from 1 eV to 2 eV causes the stability to decrease in the case SFRO while the stability is nearly constant in the case of SFMO. This weaker effect of U on the Mo site in bringing an effective exchange splitting on it can easily be seen by analyzing at the density of states for Fe, Mo-d orbitals. The features in the density of states shown in Fig.6.12 for the ferromagnetic configuration (left panel) is almost similar to that of the SFRO with the only difference that the weight of Mo-d orbitals in SFMO is less at the Fermi level when compared to Re-d states in SFRO.

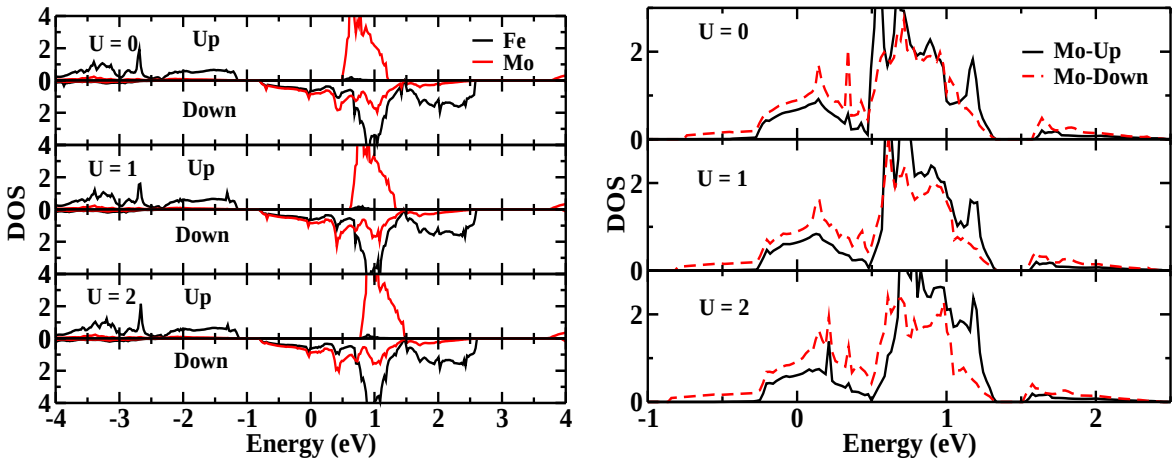

Figure 6.12: Atom projected Fe,Mo-d density of states plots from *ab initio* calculations for Sr_2FeMoO_6. The plot in the left is obtained after considering ferromagnetic configuration of Fe spins while the plot in the right is from the same closest competing antiferromagnetic state. The zero of energy is the Fermi energy.

This can be understood as the Re atom has two electrons in its d orbitals in the ionic configuration of 5+ while Mo has only one electron in its $4d$ orbital. In the antiferromagnetic configuration, U of 1 eV on the Mo-d has almost no effect on the its density of effects while a U of 2 eV brings only a small change at the Fermi level explaining the less gain in stability of the ferromagnetic state with the variation of U.

6.4 Conclusions

In this study, using *ab initio* electronic structure calculations we have explained the role of electron-electron correlations at the nonmagnetic Re site in Sr_2FeReO_6 in the context of its high ferromagnetic ordering temperature. We show that the role of U on Re site is to introduce an effective exchange splitting reducing the gain from the antiferromagnetic pathways, providing higher stability to the ferromagnetic ground state. A simple multiband Hubbard like model is developed to independently verify this finding. Within this model, indeed, we find an increase in the stability of the ferromagnetic ground state with increase of exchange splitting at Re site. Role of two electrons of Re-d orbitals result in substantial gain of the ferromagnetic stability and this is also explained by considering a similar compound Sr_2FeMoO_6 which has single d electron at the Mo site.

Bibliography

[1] J. Jensen and A. R. Mackintosh, Rare earth magnetism, Oxford UK : Clarendon Press, (1991).

[2] F. E. Mabbs and D. J. Machin, Magnetism and Transition Metal Complexes , Dover Publications, (2008).

[3] AS Bhalla , R Guo, R. Roy, Mater Res Innov **4**,3 (2000).

[4] RH. Mitchell, Perovskites: modern and ancient. Thunder Bay: Almaz Press Inc., (2000).

[5] PM. Woodward, Acta Crystallog., Sect B Struct Sci **53**, 32 (1997).

[6] G.H. Jonker and J.H. Van Santen, Physica **16**, 377 (1950); J.H. Van Santen and G.H. Jonker, Physica **16**, 599 (1950).

[7] C. Zener, Phys. Rev. **82**, 403 (1951).

[8] P. W. Anderson and H. Hasegawa, Phys. Rev. **100**, 675, (1955).

[9] A. J. Millis, P. B. Littlewood and B. I. Shraiman, Phys. Rev. Lett. **74**, 5144 (1955).

[10] M. Imada, A. Fujimori and Y. Tokura, Rev. Mod. Phys. **70**, 1039 (1998).

[11] A.B. Pippard: Magnetoresistance in Metals, Cambridge University Press (1989).

[12] Y. Tokura, Colossal Magnetoresistive Oxides, CRC PressINC, (2000).

[13] S. P. P. Parkin, Annu. Rev. Mater. Sci. **25**, 357 (1995).

[14] J. Longo and R. Ward, J. Am. Chem. Soc. **83**, 2816 (1961).

[15] F K Patterson, C W Moeller and R Ward, Inorg. Chem. **2**, 196 (1963).

[16] K.-I. Kobayashi, T. Kimura, H. Sawada, K. Terakura and Y. Tokura, Nature **395**, 677 (1998).

[17] H. Kawanaka, I. Hase, S. Toyoma and Y. Nishihara, J. Phys. Soc. Jpn. **68**, 2890 (1999).

[18] D. D. Sarma, P. Mahadevan, T. Saha-Dasgupta, S. Ray and A. Kumar, Phys. Rev. Lett. **85**, 2549 (2000).

[19] J. Kondo, Prog. Theor, Phys. **32**, 37 (1964).

[20] K. Phillips, A. Chattopadhyay and A. J. Millis, Phys. Rev. B **67**, 125119 (2003).

[21] J. L. Alonso, and L. A. Fernández, and F. Guinea, and F. Lesmes, and V. Martín-Mayor' Phys. Rev. B **67** 214423 (2003).

[22] G. Jackeli, Phys. Rev. B **68**, 092401 (2003).

[23] L. Brey, M. J. Calderon, S. Das Sarma and F. Guinea, Phys. Rev. B **74**, 094429 (2006).

[24] O. Erten, O. N. Meetei, A. Mukherjee, M. Randeria1, N. Trivedi and P. Woodward, Phys. Rev. Lett. **107**, 257201 (2011).

[25] P. Mahadevan, N. Shanthi, and D. D. Sarma, Phys. Rev. B **54**, 11199 (1996).

[26] J. C. Slater, and G. F. Koster, Phys. Rev. **94**, 1498 (1954).

[27] J. C. Slater, Phys. Rev. **34**, 1293 (1929); E. U. Condon, Phys. Rev. **36**, 1121 (1930); see also, J. S. Griffith, The Theory of Transition-Metal Ions, Cambridge University Press, Cambridge, (1961).

[28] P. E. Blöchl, Phys. Rev. B **50**, 17953 (1994).

[29] G. Kresse, D. Joubert, Phys. Rev. B **59**, 1758 (1999).

[30] G. Kresse, J. J. Furthmüller, Phys. Rev. B **54**, 11169 (1996).

[31] J. P. Perdew, K. Burke, Y. Wang, Phys. Rev. B **54**, 16533 (1996).

[32] S. L. Dudarev, G. A. Botton, S. Y. Savrasov, C. J. Humphreys, A. P. Sutton, Phys. Rev. B **57**, 1505 (1998).

[33] L. M. Sandratskii, physica status solidi (b) **136** (1), 167 (1986).

[34] S. V. Halilov, H. Eschrig, A. Y. Perlov, P. M. Oppeneer, Phys. Rev. B **58**, 293 (1998).

[35] O. Grotheer, C. Ederer, M. Fähnle, Phys. Rev. B **63**, 100401 (2001).

[36] Ležaić, Marjana and Mavropoulos, Phivos and Bihlmayer, Gustav and Blügel, Phys. Rev. B **88**, 134403 (2013).

[37] M. Marsman and J. Hafner, Phys. Rev. B **66**, 224409 (2002).

[38] D. Landau and K. Binder, A Guide to Monte Carlo Simulations in Statistical Physics, Cambridge University Press, Cambridge, England, (2000).

[39] N. Metropolis, A. Rosenbluth, M. Rosenbluth, A. Teller and E. Teller, J. Chem. Phys. **21**, 1087 (1953).

[40] J. C. Slater, and G. F. Koster, Phys. Rev. **94**, 1498 (1954).

[41] S. Nimkar, D. D. Sarma, H. R. Krishnamurthy, and S. Ramasesha, Phys. Rev. B **48**, 7355 (1993).

[42] P. Mahadevan, K. Sheshadri, D. D. Sarma, H. R. Krishnamurthy and R. Pandit, Phys. Rev. B **55**, 9203 (1997).

[43] A. A. Mostofi, J. R. Yates, Y.-S. Lee, I. Souza, D. Vanderbilt, N. Marzari, Comp. Phys. Comm., **178** 685 (2008).

Chapter 7

Layer dependent electronic structure changes in transition metal dichalcogenides: The microscopic origin

7.1 Introduction

The layered transition-metal dichalcogenides (TMDs) have been investigated for over fifty years now. However, recent interest in this class of materials has been spurred by possible applications in nanoelectronics, photovoltaics, catalysis to name a few [1–4]. Further advances in the growth of one or more layers [5, 6] has led to the exploration of the properties of these materials as a function of thickness. Analogous to the nanomaterials where one finds a size dependence of the band gap [7–10], one finds thickness dependent changes in the electronic structure of the layered transition metal dichalcogenides. Additionally one finds a thickness dependent band gap which changes character. The bulk band gap (optical) of MoS_2 is found to be an indirect one of 1.3 eV [11] which increases to 1.6 eV in the bilayer limit [12]. The nature of the band gap changes and becomes a direct one of 1.9 eV at the monolayer limit [13]. The fact that the monolayers of transition metal dichalcogenides have a direct band gap (with the exception of WSe_2 [14]) is

evident from the sharp peak that one finds in the photoluminescence spectra [15, 16] . $MoSe_2$ also has an indirect band gap of 1.1 eV [17] in the bulk limit whereas in the monolayer limit it has direct band gap of about 1.66 eV [18]. There could be different types of MX_2 (M = Mo, W, Ti etc., X = S, Se, etc.) sandwiches depending on the coordination of the transition metal atom with the chalcogens as well as the stacking of atoms [19]. In this work we focus our attention on the 2H polymorph of MoX_2 (X=S,Se) where the symmetry about the Mo site is trigonal prismatic, though certain generic features are found to be valid across different types of stacking. The bonding within each monolayer is strongly covalent. However, the coupling between layers is believed to be due to weak van der Waals interaction.

The size dependence of the band gap in semiconductor nanostructures has been extensively studied [20]. The effect arises because the wavefunctions associated with the band edge begin to feel the effects of the boundary, and this happens for nanostructures where atleast one of the dimensions is less than the Bohr excitonic radius. The Bohr radius is a material dependent property and for CdSe for instance is found to be 56 Å [21]. As the system sizes are large, this has necessitated the use of semi-empirical methods to examine the size dependence of the band gap. One such popular method has been the tight- binding model method. The size dependence that one finds in the tight-binding model emerges from two effects. The first is the changed coordination of the atom which could affect the Madelung potential and therefore the onsite energies of the levels on that atom. The second is the change in the bandwidth due to reduced coordination faced by some of the atoms. Usually only the latter effects are considered. In the context of the transition metal dichalcogenides, however, the effects due to former become important as unlike in the nanostructures where a small fraction of the atoms have different coordination, here, a significant fraction have a coordination different from the bulk. A mapping onto a tight binding model allows us to explore for the first time the role of various contributions leading to quantum confinement.

Cappelluti *et al.* [22] fit the *ab-initio* band structure for a monolayer of MoS_2 to a nearest neighbor tight binding model. Using the same parameters within each layer and introducing interactions between the layers, the *ab-initio* band structure for bulk MoS_2 was fit and the relevant parameters extracted. From this model, it was inferred that interlayer interactions were responsible for the direct to indirect band gap transition in these materials. As has been

mentioned earlier, the Madelung potential felt by each atom in a layer changes as one goes from monolayer to bilayer. This effect has not been considered in the tight binding model that they construct. Recently Zhang and Zunger [23] examined various aspects of the thickness dependent changes in the electronic structure and arrived at the conclusion that kinetic energy controlled quantum confinement as well as potential energy controlled band repulsion were responsible for the observed changes. This would in a tight binding framework correspond to a modification of the onsite energies in addition to the inclusion of interlayer hopping interactions being responsible for the thickness dependent changes in the electronic structure. Kang *et al.* [24] attributed the transition to the absence of interlayer interactions at K point, a general feature they attributed to the crystal symmetry of hexagonal materials. They considered the presence of the second layer as a perturbation to the first layer. The strength of this perturbation was found to be dependent on the k-point. However this does not say anything about whether the perturbation is to the onsite energies as a result of the modified Madelung potential that the electrons feel or is due to the additional neighbors as a result of interlayer interactions becoming relevant because of the presence of second layer. In view of the differing viewpoints existing in the literature, there is a need to reexamine this problem. Few layers of the transition metal dichalcogenides are referred to as van der Waal heterostructures. This nomenclature is suggestive of a dominant role played by van der Waal's interactions with all other interactions playing a smaller role.

The direct band gap originates from a transition from the valence band maximum at K to the conduction band minimum at the same point. This was found to show a weak dependence on size. The indirect band gap arises from a transition from the top of the valence band at Γ to the bottom of the conduction band between Γ and K, and exhibits a strong dependence on the number of layers. In order to examine the origin of the observed variations in the band gap with size, Padilha *et al.* [25] chose an internal reference in each case and monitored the size dependence of the band extrema points. They found that while the band extrema at K point hardly showed any size dependence, the band extrema at Γ and T showed significant variations with thickness which determined the band gap. Examining the charge density associated with the band extrema at Γ point, they found that they were contributed by orbitals directed out of plane, hence explaining the changes in the position of the band extrema as each additional layer was added.

In this manuscript we have studied the variation of the band gap in $MoSe_2$ as a function of number of layers. The band structures obtained from *ab-initio* electronic structure calculations are found to reproduce the experimental observation [12] that this system is a direct band gap semiconductor in the monolayer limit, but as we move to the bilayer, the system becomes an indirect band gap one. As mentioned earlier, the evolution in the electronic structure of the transition metal dichalcogenides with thickness has been discussed in terms of quantum confinement effects and interlayer interactions. In order to understand the role of each of these quantities in bringing about the band gap crossover, our approach has been to carry out an *ab-initio* mapping onto a tight binding model. This method uses maximally localized Wannier functions as its basis functions. Geometric confinement effects are expected to renormalize the onsite energies of the orbitals which are directed into the vacuum as against those orbitals which are in-plane, in line with the belief that these orbitals feel the effect of the boundary. Additionally, one knows that as one builds a solid atom by atom, the onsite energies get renormalized because of the potential felt by the electrons due to the neighboring atoms (Madelung effect). As a result there should be a change in the onsite energies as one went from monolayer to bilayer to trilayer. The tight binding mapping carried out for monolayer and bilayer are found to have similar onsite energies. Hence one concluded that there was no renormalization of the energies. The changes in the electronic structure as a function of the number of layers arose from interlayer interactions present when a layer was added to a monolayer. To check this point we used the tight binding Hamiltonian of the bilayer, switched off interlayer interactions and recovered the monolayer band structure, as one would expect. A similar construction of the trilayer band structure within the tight binding model was carried out using the monolayer Hamiltonian for the layers and the interlayer interactions derived from the bilayer Hamiltonian. The electronic structure constructed this way gave perfect match with the *ab-initio* band structure. Hence our results showed *quantitatively that interlayer interactions were responsible* for the changes in the electronic structure that one found as a function of the number of layers, with geometric confinement effects or Madelung potential changes playing a negligible role. Similar conclusions were arrived at for the other transition metal dichalcogenides MX_2 where M=Mo, W and X=S,Se,Te also. While the 2H stacking was considered in each of the cases listed above, alternate stacking arrangements could lead to vary different environments and therefore Madelung potentials being experienced by the

atoms in the other layer. This should result in different onsite energies of the transition metal d and Se/Se/Te p levels which would depend on the type of stacking. This is however not found to be the case. This therefore led us to the rather puzzling conclusion that interlayer interactions dictated the electronic structure changes even in these materials. The usual nomenclature has been to refer to these materials as van der Waal's heterostructures, emerging from the belief that the dominant interaction between the layers is from van der Waal's interactions. In this work we consider the entire class of materials and show that interlayer interactions which have a covalent origin determine the electronic structure changes with thickness.

7.2 Methodology

The electronic structure calculations of monolayer, bilayer as well as trilayer $MoSe_2$ as well as monolayer and bilayer MoS_2 are carried out within a plane wave implementation of density functional theory (DFT) using the VASP [26] code. We have taken the 2H stacking of $MoSe_2$ as it is found to be the most stable structure [27]. While, the lattice constants are kept at the experimental values of a=3.299 Å and c=12.939 Å for $MoSe_2$ [28] and a=3.16 Å and c=12.296 Å for MoS_2 [29], all the atoms are allowed to relax through a total energy minimization that is guided by the calculated atomic forces. A vacuum of 20 Å is used along z direction to minimize the interaction among the periodic images. Projected augmented wave [30, 31] potentials are used to solve the electronic structure self-consistently using a k-points mesh of $12\times12\times1$ with a cutoff energy for the plane wave basis states equal to 280 eV. Perdew-Burke-Ernzerhof (PBE) [32] approximation was used for the exchange-correlation functional. There is a weak van der Waals interaction between the layers which has an effect in the determination of the interlayer distances. A dispersion correction based on Grimme´s DFT-D2 method [33] is used on top of the PBE potentials.

In order to quantify the results, we setup a tight binding model with Mo d and Se p/S p states in the basis. In this model, the maximally localized Wannier functions [34] are used for the radial parts of the basis functions. Technically, the degree of localization and the symmetry of these Wannier functions can be controlled in the projection procedure. All on-site energies and hopping interaction strengths in this case are determined from the interface of VASP to

Wannier90 [35]. Apart from the 2H stacking, we also explored other stacking geometries AA, A′B, AB′ and AB to explore the renormalization of the onsite energies due to differing Madelung potentials. An explanation for the notation for the stacking may be found in Ref. [36].

In order to generalize our findings, we did the similar analysis mentioned earlier for $MoTe_2$, WS_2, WSe_2 and WTe_2. The experimental lattice parameters of a= 3.522, 3.1532, 3.282, Å and c= 13.967, 12.323, 12.96, Å were considered for $MoTe_2$, WS_2, WSe_2 and WTe_2 [37] respectively. The internal positions were optimized in each case for both monolayer and bilayer. The van der Waals interactions implemented using the DFT-D2 method of Grimme were considered for positional optimization in the case of bilayer. The $ab-initio$ band structure was then calculated for each of these cases and the results for the bilayers were then mapped onto a tight binding model with Mo/W d and S,Se and Te p orbitals in the basis. The radial part of the tight binding basis functions corresponded to maximally localized Wannier functions.

7.3 Results and Discussion

The *ab-initio* band dispersions for monolayer $MoSe_2$ along various symmetry directions are plotted in Fig. 7.1. One finds that the valence band maximum (VBM) and the conduction band minimum (CBM) are both located at K point and the system is a direct band gap semiconductor.

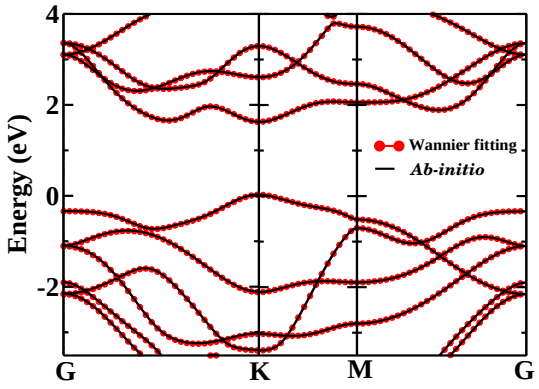

Figure 7.1: The $ab-initio$ (solid line) and tight binding band structure (red circles) for monolayer $MoSe_2$. Zero of the energy is the valence band maximum. This figure is taken from Ref. [38].

This is consistent with experiment which also finds the system to be a direct band gap semiconductor with a gap of 1.66 eV. While the experimental band gap is the optical band gap, in our

calculations we are calculating the single particle gap. The present calculations which use GGA for the exchange correlation functional find a gap of 1.59 eV which is close to the experimental value. The agreement is however fortuitous as one usually has an underestimation of the band gap due to self-interaction effects among various other approximations which enter the use of the generalized gradient approximation in the absence of an exact exchange correlation functional. In order to quantify the changes in the electronic structure, we have mapped the *ab-initio* band structure onto a tight binding model with Mo d and Se p states in the basis. The tight binding band structure shown by red line with circles is superposed on the calculated *ab-initio* band structure in Fig. 7.1. We have a good description of the *ab-initio* band structure in the energy window from -3.5 eV to 4 eV. This gives us confidence in the extracted parameters and allows us to discuss changes in the electronic structure in terms of these parameters.

There are several ways to construct the bilayer of $MoSe_2$. Each monolayer can be visualized as a three atomic layer stacking of Mo and Se atoms where Mo atoms are sandwiched between layers of Se atoms. The Se atoms generate a trigonal prismatic crystal field at the Mo site. The stacking that we have considered has the Mo atom in one layer above that in the layer beneath. However, the Mo-Se motif is rotated by 180° in the upper layer with respect to the layer beneath. This is referred to as the AA′ stacking and has been shown to have the lowest energy among various stacking patterns considered.

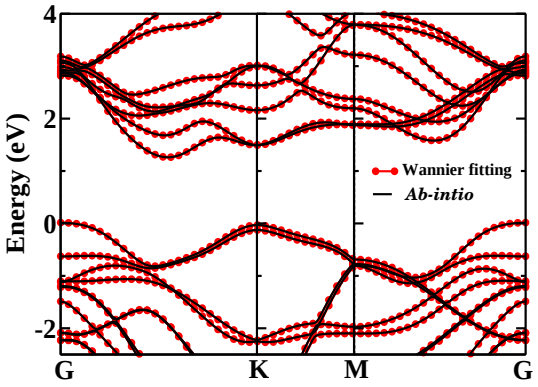

Figure 7.2: The $ab-initio$ (solid line) and tight binding band structure (red circles) for bilayer $MoSe_2$. Zero of the energy is the valence band maximum. This figure is taken from Ref. [38].

Considering a bilayer of $MoSe_2$, we have calculated the band dispersions along various symmetry directions. This is shown in Fig. 7.2. We find that the VBM which was at K point has now shifted to Γ. The CBM is also shifted to T point which lies along the line from Γ to K.

This leads to an indirect band gap of 1.25 eV in contrast to the experimental value of 1.55 eV [12]. The changeover in the VBM positions can easily be understood by examining the character of the states contributing to this point. This is shown in Fig. 7.3 where we plot the charge density for the highest occupied band at Γ in panel (a).

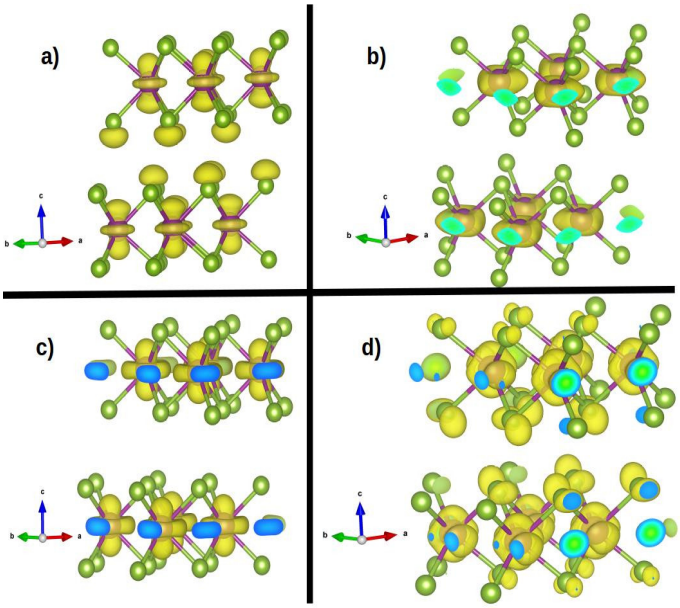

Figure 7.3: The charge density plots for (a) highest occupied band at Γ, (b) valence band maximum at K, (c) lowest unoccupied band at T and (d) conduction band minimum at K for monolayer $MoSe_2$.

These are seen to emerge from the interactions between the d_{z^2} orbitals on Mo and p_z orbitals on Se. As these involve orbitals which are directed out of plane, one finds that these levels in the lower layer interact with the d_{z^2}/p_z orbitals in the layer above. As a result, the highest occupied band at Γ point moves to higher energies relative to that at K point, and consequently the VBM shifts to Γ point when we move from monolayer to bilayer. The highest occupied band at the K point is contributed by interactions between in-plane orbitals as is evident from Fig. 7.3(b). Hence it shows no shift in the bilayer from its position for the monolayer. A similar analysis of the charge density contributing to the lowest unoccupied band at T and K symmetry points is shown in panels (c) and (d) of Fig. 7.3. We find that in-plane orbitals contribute to the lowest

unoccupied band at K point while out-of-plane orbitals contribute to the lowest unoccupied band at T point. Hence, the increased interaction arising from the presence of the second layer moves T point relative to K point, making the former the conduction band minimum. These ideas are consistent with the analysis of Padhila *et al.* [25] who examined the movement of various band extrema as a function of the number of layers.

While these ideas are qualitative, we map the $ab-initio$ band structure to a tight binding model and extract the onsite energies and hopping interaction strengths in order to make a more quantitative statement of the role of various effects which determine the electronic structure changes. The tight binding band structure is superposed on the *ab-initio* band structure calculated for the monolayer in Fig.7.1 and for the bilayer in Fig. 7.2. The quality of the fit in both cases gives us confidence in the extracted parameters (Table 7.1) which we use to discuss changes in the electronic structure in going from the monolayer to the bilayer.

Table 7.1: Onsite energies obtained from tight binding mapping of the $ab-initio$ band structure. A basis consisting of Mo d and Se p states has been considered for monolayer and bilayer $MoSe_2$. The respective Se p_x is taken as reference for the energies given in eV. This table is taken from Ref. [38].

Orbitals	Monolayer $MoSe_2$	Bilayer $MoSe_2$
Se-E_{p_x}	0.00	+0.01
Se-E_{p_y}	0.00	0.0
Se-E_{p_z}	-0.33	-0.38
Mo-$E_{d_{xy}}$	+1.46	+1.51
Mo-$E_{d_{yz}}$	+2.28	+2.31
Mo-$E_{d_{zx}}$	+2.28	+2.31
Mo-$E_{d_{x^2-y^2}}$	+1.46	+1.52
Mo-$E_{d_{z^2}}$	+1.20	+1.27

The onsite energies for Se p as well as Mo d orbitals extracted by the tight binding mapping for monolayer as well as bilayer $MoSe_2$ are given in Table 7.1. The energies are similar within deviations associated with the error bars on the energies. Hence we can conclude that geometric confinement effects or the Madelung potential differences for the atoms in the bilayer as compared to the monolayer do not modify the onsite energies when one goes from monolayer to bilayer. In order to examine what is it that changes leading to the differences in the electronic structure in going from monolayer to bilayer, we have considered the tight binding Hamiltonian for the

bilayer. Interlayer interactions have been switched off in this Hamiltonian and the ensuing band structure has been plotted along various symmetry directions in Fig. 7.4.

The band structure for the monolayer has been superposed for comparison. The two band structures look almost identical suggesting that the only difference between the electronic structure of the monolayer and that for the bilayer emerge from interlayer interactions. The dominant interlayer hopping interaction strengths of bilayer $MoSe_2$ are between the first nearest neighbor Mo-d_z^2 and Se-p_z (4.88 Å) and also between the Se-p orbitals which are first (3.72 Å) as well as second (5.92 Å) neighbors.

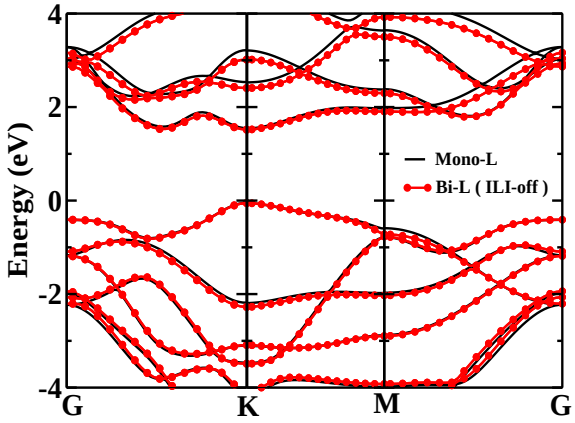

Figure 7.4: The $ab-initio$ band structure (solid line) for monolayer $MoSe_2$ compared with the tight binding band structure (red circles) of bilayer with interlayer interactions switched off. The zero of energy is the valence band maximum.This figure is taken from Ref. [38].

In order to examine this hypothesis further, we constructed a trilayer heterostructure of $MoSe_2$. The *ab-initio* band structure for the trilayer was calculated along various symmetry directions. This is shown in Fig.7.5.

For comparison and to examine the hypothesis made vis-a-vis the origin of the changes in the electronic structure as each layer is added, we set up the tight binding Hamiltonian for the trilayer. This was done by considering the Hamiltonian for the monolayer for each of the layers. The interlayer interactions extracted for the bilayer were then used to couple the layers. The band structure calculated within this model is superposed on the *ab-initio* band structure for the trilayer in Fig. 7.5. The comparison is reasonably good, justifying our hypothesis.

These results clearly show that the electronic structure changes in going from the monolayer to bilayer and beyond are derived from interlayer hopping interactions alone.

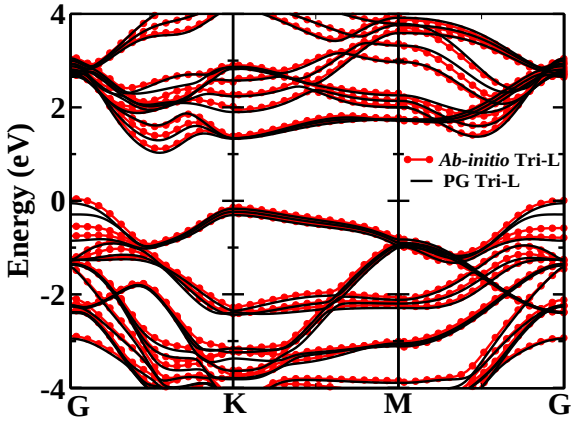

Figure 7.5: $Ab-initio$ (solid line) and tight binding (red circles) band structure for trilayer $MoSe_2$. The tight binding Hamiltonian for the trilayer has been constructed from monolayer for the layers and interlayer interactions taken from the bilayer. Zero of energy is the valence band maximum.

This is a surprising result as the nomenclature used for these systems in van der Waal heterostructures. This would have us believe that the dominant interaction is van der Waal interactions. However our analysis suggests that covalent interactions determine the modification in the electronic structure with thickness. This is not entirely surprising as the nearest neighbor separations between Se atoms of two layers is 3.19 Å. Hence the presence of finite hopping interaction strengths for electrons in the two layers is not entirely surprising. This immediately raises the question of the role played by van der Waal's interactions. This interlayer separation for the bilayer is found to be 3.99 Å when van der Waal's interactions are not included and 3.18 Å when they are. Hence their inclusion merely predicts the interlayer separation. However the electronic structure evolution with every additional layer is dictated by the interlayer interactions.

While we have examined the onsite energies in going from monolayer to bilayer for the 2H stacking, there are other stackings possible. In order to examine whether our conclusions were general enough, we considered bilayers with AA, A′B, AB′ and AB stacking with the nomenclature used as given in Ref. [19]. In each case the *ab-initio* band structure was fit to a tight binding model with Mo d and Se p states in the basis. The extracted onsite energies are given in Table 7.2. These onsite energies for different stacking of layers in $MoSe_2$ bilayer look just like what we

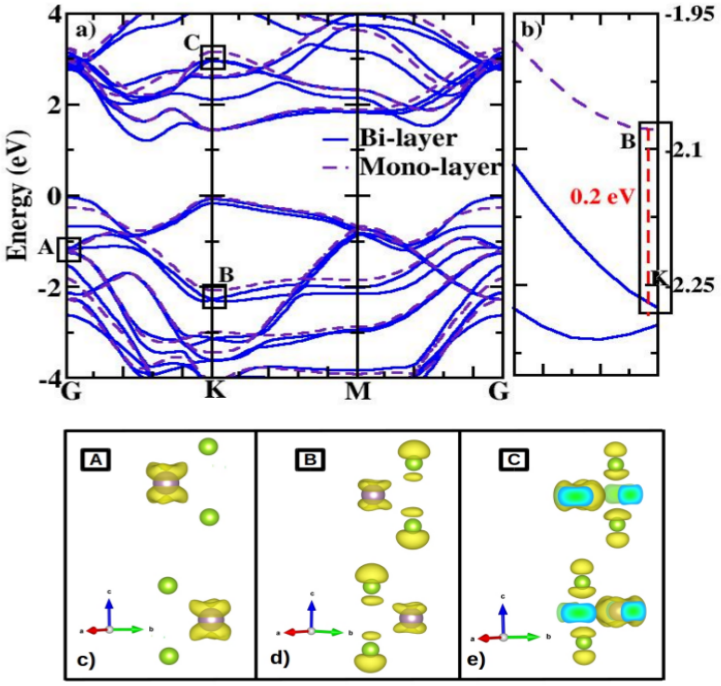

Figure 7.6: (a) The $ab-initio$ band structure for monolayer (dashed lines) and bilayer (solid lines) for $MoSe_2$ along various symmetry directions. The bands have been aligned at the valence band maximum at K point. Three sets of bands have been identified and are labelled A, B and C. The bands at B are zoomed in panel (b). The corresponding charge densities for A, B and C are shown in panels (c)-(e).

Table 7.2: Onsite energies obtained from tight binding mapping of the *ab-initio* band structure for different stackings of layers in $MoSe_2$ bilayer. A basis consisting of Mo d and Se p states has been considered. The respective Se p_x is taken as reference for the energies given in eV.

Orbitals	AA	A′B	AB′	AB
Se-E_{p_x}	0.0	0.0	0.0	0.0
Se-E_{p_y}	0.0	0.0	0.0	0.0
Se-E_{p_z}	-0.35	-0.36	-0.35	-0.35
Mo-$E_{d_{xy}}$	+1.52	+1.53	+1.50	+1.51
Mo-$E_{d_{yz}}$	+2.30	+2.31	2.29	+2.30
Mo-$E_{d_{zx}}$	+2.30	+2.31	2.29	+2.30
Mo-$E_{d_{x^2-y^2}}$	+1.52	+1.53	+1.50	+1.51
Mo-$E_{d_{z^2}}$	+1.28	+1.28	+1.25	+1.26

found in the case of 2H stacking (Table 7.1). One would expect a modification in the onsite energies because of the Madelung potential differences that are associated with the different types of stacking. The fact that they remain almost unchanged suggests that the approximation of

splitting up the bilayer/trilayer Hamiltonian into monolayers coupled by interlayer interactions remains valid.

The evolution of the electronic structure with number of layers that we find here is not specific to $MoSe_2$ alone. We find similar changes when we have examined the electronic structure as a function of the number of layers for MoS_2 also.

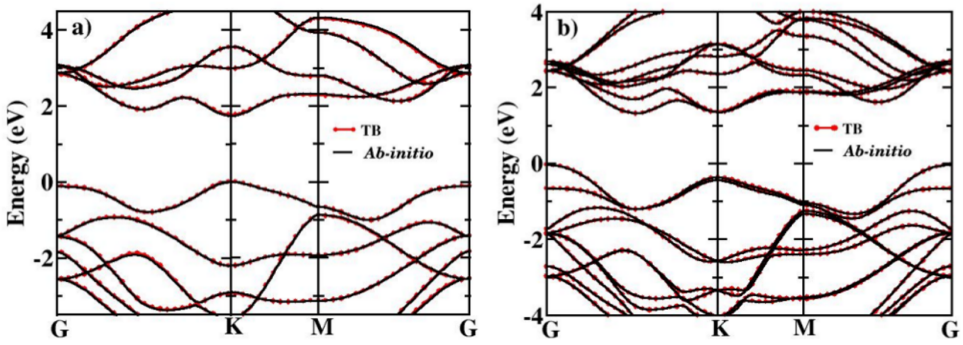

Figure 7.7: *Ab−initio* (solid line) and tight binding band structure (red circles) for (a) monolayer and (b) bilayer MoS_2. Zero of energy corresponds to the valence band maximum. This figure is taken from Ref. [38].

In Fig. 7.7 we have plotted the *ab-initio* band structure for the monolayer in panel (a) and for the bilayer in panel (b). The tight-binding band structure has been superposed in each case and we have a good description of the *ab-initio* band structure. Geometric confinement effects are expected to modify the onsite energies of the orbitals directed out of plane as against those which lie in plane. A comparison of the extracted onsite energies is given in Table 7.3.

Table 7.3: Onsite energies obtained from tight binding mapping of the *ab-initio* band structure. A basis consisting of Mo d and S p states has been considered for monolayer and bilayer MoS_2 . The respective S p_x is taken as reference for the energies given in eV.

Orbitals	Monolayer MoS_2	Bilayer MoS_2
S-E_{p_x}	0.00	0.0
S-E_{p_y}	0.00	0.0
S-E_{p_z}	-0.28	-0.25
Mo-$E_{d_{xy}}$	+1.66	+1.69
Mo-$E_{d_{yz}}$	+2.68	+2.69
Mo-$E_{d_{zx}}$	+2.68	+2.69
Mo-$E_{d_{x^2-y^2}}$	+1.65	+1.68
Mo-$E_{d_{z^2}}$	+1.46	+1.47

Here again, we find that the energies for the monolayer and bilayer are similar. This shows that geometric confinement effects or Madelung potential variations are not responsible for the changes in the electronic structure. When we considered the tight binding Hamiltonian for the bilayer and switched off interlayer interactions, we recovered the monolayer band structure. The comparison between the model Hamiltonian results with interlayer interactions switched off and the *ab-initio* band structure for the monolayer is given in Fig. 7.8.

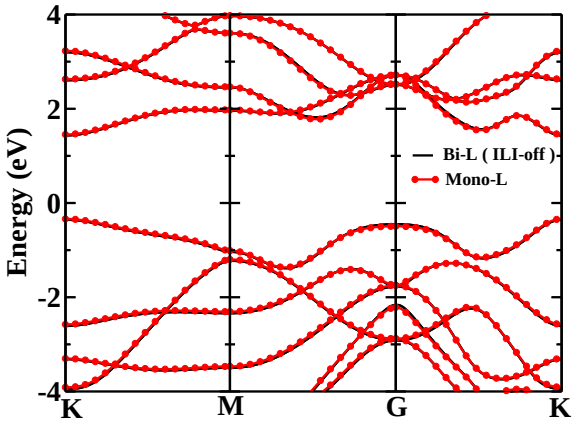

Figure 7.8: The $ab-initio$ band structure (solid line) for monolayer MoS_2 compared with the tight binding band structure (red circles) of bilayer with interlayer interactions switched off. The zero of energy is the valence band maximum. This figure is taken from Ref. [38].

In order to demonstrate that the conclusions obtained from our analysis of $MoSe_2$ and MoS_2 are general, we have considered a monolayer as well as bilayers of $MoTe_2$, WS_2, WSe_2 and WTe_2.

The $ab-initio$ band dispersions calculated for the monolayer of each of these systems along various symmetry directions is shown in Fig.7.9.

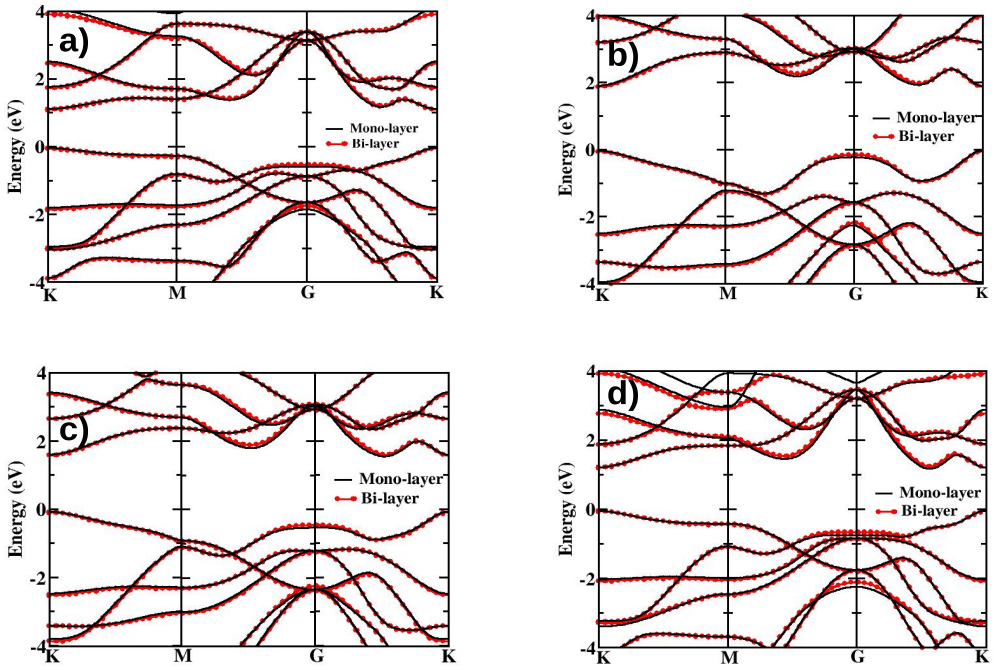

Figure 7.9: (Color online) The $ab-initio$ band structure (solid line) for monolayer compared with the tight binding band structure (red circles) of bilayer with interlayer interactions switched off, for (a) $MoTe_2$, (b) WS_2, (c) WSe_2 and (d) WTe_2. The zero of energy is the valence band maximum.

The $ab-initio$ band structure for the bilayer was mapped onto a tight binding model with maximally localized Wannier functions for the radial part. The ensuing band structure for the bilayers, with interlayer interactions switched off, has been superposed on the monolayer band structure in Fig.7.9. The two are found to be almost identical for each of the systems shown here, indicating that the differences in the electronic structure between monolayer and bilayer arise due to interlayer interactions alone.

7.4 Conclusion

In conclusion, we have examined the evolution in the electronic structure of transition metal dichalcogenides as a function of layers. The changes in the structure that one finds have been discussed in terms of a combination of interlayer hopping interactions, geometric confinement

effects as well as Madelung potential effects. Considering the examples of MoS_2 and $MoSe_2$, a mapping onto a tight binding model with Mo d and Se/S p states in the basis allows us to quantify the role of each of these effects. Even in these layered materials which are referred to as van der Waals heterostructures, we find that interlayer hopping interactions play the primary role in bringing about changes in the electronic structure as a function of thickness. Geometric confinement effects as well as expected Madelung potential variations on the other hand, we find, play no role in the observed changes in electronic structure.

Bibliography

[1] G. Eda and S. A. Maier, ACS Nano **7**, 5660 (2013).

[2] Q. H. Wang, K. Kalantar-Zadeh, A. Kis *et al.*, Nat. Nanotechnol. **7**, 699 (2012).

[3] W. K. Ho, J. C. Yu, J. Lin *et al.*, Langmuir **20**, 5865 (2004).

[4] E. Fortin and W. Sears, J. Phys. Chem. Solids **43**, 881 (1982).

[5] Yongjie Zhan, Zheng Liu, Sina Najmaei, Pulickel M. Ajayan and Jun Lou, Small **8**, 966 (2012).

[6] Ismail Bilgin *et al.*, ACS Nano **9**, 8822 (2015).

[7] R. C. Jin, Y. W. Cao, C. A. Mirkin *et al.*, Science **294**, 1901 (2001).

[8] M. B. Sigman, A. Ghezelbash, T. Hanrath *et al.*, J. Am. Chem. Soc. **125**, 16050 (2003).

[9] S. Ithurria, M. D. Tessier, B. Mahler *et al.*, Nature Mater. **10**, 936 (2011).

[10] Ranjani Viswanatha, Sameer Sapra, B. Satpati, P. V. Satyam, B. N. Dev and D. D. Sarma, J. Mater. Chem. **14**, 661 (2004).

[11] G. L. Frey, S. Elani, M. Homyonfer *et al.*, Phys. Rev. B **57**, 6666 (1998).

[12] S. Tongay, J. Zhou, C. Ataca *et al.*, Nano Lett. **12**, 5576 (2012).

[13] K. F. Mak, C. Lee, J. Hone *et al.*, Phys. Rev. Lett. **105**, 136805 (2010).

[14] Chendong Zhang, Yuxuan Chen, Amber Johnson, Ming-Yang Li, Lain-Jong Li, Patrick C. Mende, Randall M. Feenstra and Chih-Kang Shih, Nano Lett. **15**, 6494 (2015).

[15] W. Jin, P.-C. Yeh, N. Zaki *et al.*, Phys. Rev. Lett. **111**, 106801 (2013).

[16] Andrea Splendiani, Liang Sun, Yuanbo Zhang, Tianshu Li, Jonghwan Kim, Chi-Yung Chim, Giulia Galli and Feng Wang, Nano Lett. **10**, 1271 (2010).

[17] T. Böker, R. Severin, A. Müller *et al.*, Phys. Rev. B **64**, 235305 (2001).

[18] J. S.Ross, S. Wu, H. Yu *et al.*, Nat. Commun., **4**, 1474 (2013).

[19] Jiangang He, Kerstin Hummer and Cesare Franchini, Phys. Rev. B **89**, 075409 (2014).

[20] Ranjani Viswanatha, Sameer Sapra, Tanusri Saha-Dasgupta and D. D. Sarma, Phys. Rev. B **72**, 045333 (2005).

[21] A. I. Ekimov, F. Hache, M. C. Schanne-Klein, D. Ricard, C. Flytzanis, I. A. Kudryavtsev, T. V. Yazeva, A. V. Rodina and Al. L. Efros, J. Opt. Soc. Am. B **10**, 100 (1993).

[22] E. Cappelluti, R. Roldán, J. A. Silva-Guillén, P. Ordejón and F. Guinea, Phys. Rev. B **88**, 075409 (2013).

[23] L. Zhang and A. Zunger, Nano Lett. **15**, 949 (2015).

[24] Joongoo Kang, Lijun Zhang and Su-Huai Wei, J. Phy. Chem. Lett. **7**, 597 (2016).

[25] J. E. Padilha, H. Peelaers, A. Janotti *et al.*, Phys. Rev. B **90**, 205420 (2014).

[26] G. Kresse and J. Furthmüller, Phys. Rev. B **54**, 11169 (1996).

[27] Q. Liu, L. Li, Y. Li *et al.*, J. Phys. Chem. C, **116**, 21556 (2012).

[28] A. A. Al-Hilli and B. L. Evans, J. Cryst. Growth **15**, 93 (1972).

[29] L. Liu, S. B. Kumar, Y. Ouyang *et al.*, IEEE Trans. Electron Devices **58**, 3042 (2011).

[30] G. Kresse and D. Joubert, Phys. Rev. B **59**, 1758 (1999).

[31] P.E. Blöchl, Phys. Rev. B **50**, 17953 (1994).

[32] J. Paier, R. Hirschl, M. Marsman *et al.*, J. Chem. Phys. **122**, 234102 (2005).

[33] S. Grimme, J. Comput. Chem. **27**, 1787 (2006).

[34] A. A. Mostofi, J. R. Yates, Y.-S. Lee *et al.*, Comput. Phys. Commun. **178**, 685 (2008).

[35] C. Franchini, R. Kováčik, M. Marsman *et al.*, J. Phys.: Condens. Matter **24**, 235602 (2012).

[36] Gabriel Constantinescu, Agnieszka Kuc and Thomas Heine, Phys. Rev. Lett. **111**, 036104 (2013).

[37] R. Shepherd and T.A. James, US Patent **3,306,701** (1967).

[38] Ruma Das, *Electronic and structural properties of two dimensional semiconductors and oxides*, Thesis submitted to Calcutta University (2018).

Chapter 8

Summary and Conclusions

The aim of this thesis was to understand some of the unusual yet interesting phenomenon which exist in transition metal compounds. We have focused our study on the spin and charge ordering in transition metal compounds and the microscopic origin behind these interesting properties. For this purpose, we have used a combination of *ab initio* and model Hamiltonian methods as our tools for the analysis. While choosing materials, unusual examples of transition metal compounds have been considered. Starting from exploration of a route to get an antiferromagnetic metal in transition metal oxides (TMOs), we also discussed the reason behind robust insulating ground state found even at much large doping concentrations in many TMOs. Study on an unusual example of ferromagnetic insulator was also done and the microscopic mechanism driving the ground state was explored in detail. The reason behind the above room temperature magnetism shown by double perovskite oxides has been explained and based on our results, a route to enhance the magnetic transition temperature has been proposed for these materials. Apart from the topics, we also studied the changes in the electronic structure of transition metal dichalcogenides with layer thickness and pointed out the primary mechanism behind the change in the electronic structure as a function of layer thickness.

In the first part of chapter 1 in this thesis, we have briefly thrown some light on the basic concepts and phenomena crucial to our interest of understanding the unusual and interesting properties shown by the above mentioned materials. Starting from a brief history of magnetism, concept of magnetism in atoms as well as in solids emerging from various exchange interactions have

been discussed. We then went on to discuss the concept of electron-electron correlations and its importance in the discussion of various properties shown by transition metal compounds. This was done in the framework of a multiband Hubbard model. In the second part, we summarized the case of doped correlated systems mainly in contexts of magnetism and charge ordering. We then went on to discuss magnetism in double perovskite oxides and various attempts present in the literature to explain it. In case of 2D materials, the effect of confinement on the electronic structure was explained in brief.

In chapter 2 of this thesis, we discussed various physical concepts and computational methods based on these concepts. Starting from the Schrödinger equation, different theories along with the variational principle to obtain the ground state solutions have been explained. Density functional theory and a multiband Hubbard model have been extensively used in this thesis for the involved calculations and hence these two methods were discussed in great detail. We also discussed the tight binding formalism and the concept of Wannier functions which we used in our analysis of materials properties.

In chapter 3 of this thesis, we explore the design principle of doping carriers into an antiferromagnetic insulator as a route to obtaining AFM metals. Calculations based on a multiband Hubbard model have been carried out considering parameters relevant for $3d$ and $5d$ transition metal oxides. The stability of the lowest energy phase with respect to the closest energy competing phase was calculated as a function of U on transition metal atom in both the cases at various electron doping percentages. In the case of $5d$ oxide, we find an AFM metallic state to be stabilized at small values of U, while in the large-U regime a charge-ordered insulating phase with a net magnetic moment per unit cell was found to be stable. In contrast, for electron doping of a $3d$ transition metal oxide no AFM metallic phase is stable in any regime of the phase diagram. The relative value of the crystal field splitting with respect to the exchange splitting determines if the doped electron occupies the minority spin t_{2g} level or the majority spin e_g level. When the doped electron is in the minority spin t_{2g} level, we have an antiferromagnetic metallic phase stabilized, while when the doped electron is in the majority spin e_g level, a ferromagnetic metallic phase is stabilized. While one has a FM metallic phase at low values of U , a charge-ordered insulating phase is stabilized at large values of U . The large-U regime of the multiband model has no limit at which one has a FM metallic phase as expected by the Nagoaka

theorem. This is however found in the single-band case. Orbital degeneracy is also found to play an important role in the enhanced stability of the AFM metallic phase.

In chapter 4 of this thesis, we have explained the driving mechanism behind the robust insulating state found even at high carrier doping in the case of some of the transition metal oxides like $LaCrO_3$ and $LaFeO_3$. Considering a multiband Hubbard model, we show that the exchange splitting induced localization of carriers and the polaronic distortions play an almost equal role in driving the system insulating among the $3d$ transition metal oxides. Phase diagrams were obtained with variation of U on the transition metal d states for both $3d$ and $5d$ transition metal oxides. We found that in the region which is relevant for the $3d$ oxide, charge ordered insulating ground states appear naturally at carrier doping concentrations as high as 50 %. We rule out the role of large Hund's interaction in the stabilization of such an unusual ground state and show that this mechanism will be operational in systems with small values of Hund's interaction also, suggesting that there could be examples among the $4d$ and the $5d$ transition metal oxides which could also refuse to go metallic on doping. By varying the charge transfer energy (Δ), we show that the superexchange background of localized spins at the transition metal sites are mainly responsible for the charge ordered insulating ground state. In the case of a $5d$ transition metal, we found that the superexchange is stronger in the electron doped case than the hole doped one. Based on our findings we suggested that hole doping is a more viable route to achieve the AFM metallic phase.

In chapter 5 of this thesis, using the first principle method, we have studied Cr doping in VO_2 at different doping concentrations. In agreement with experiments, we also found an unusual ferromagnetic insulating ground state at 12.5 % Cr doping. Doping Cr at the V site in VO_2 has been seen to stabilize the +3 valency in Cr, the stability of which emerges from the strong stability associated with half-filled t_{2g} orbitals. It is additionally stabilized by the formation of V^{+5} associated with a neighboring V site. We found that the presence of empty d orbitals at the V^{+5} sites and filled t_{2g} orbitals at the Cr^{+3} sites leads to hopping pathways that stabilize a ferromagnetic insulating state. By a mapping onto a tight binding model involving V, Cr d states and O p states in the basis, we were able to show the role of charge ordering in stabilizing the ferromagnetic insulating state in this material.

In chapter 6 of this thesis, using an *ab initio* approach we explained the role of electron-electron correlations at the nonmagnetic Re site in Sr_2FeReO_6 in the context of its high ferromagnetic ordering temperature. We show the role of U on Re site is to introduce an effective exchange splitting reducing the gain from the antiferromagnetic pathways, providing higher stability to the ferromagnetic ground state. A simple multiband Hubbard like model is used to independently verify this finding. Within this model, we find an increase in the stability of the ferromagnetic ground state with increase of exchange splitting at Re site. Role of two electrons of Re-d orbitals results in substantial gain of the ferromagnetic stability in contrast to Sr_2FeMoO_6 which has single d electron at the Mo site.

In chapter 7 of this thesis, we have examined the evolution in the electronic structure of transition metal dichalcogenides as a function of layers. The changes in the structure that one finds have been discussed in terms of a combination of interlayer hopping interactions, geometric confinement effects as well as Madelung potential effects. Considering the examples of MoS_2 and $MoSe_2$, a mapping onto a tight binding model with Mo d and Se/S p states in the basis allows us to quantify the role of each of these effects. Even in these layered materials which are referred to as van der Waals heterostructures, we find that interlayer hopping interactions play the primary role in bringing about changes in the electronic structure as a function of thickness. Geometric confinement effects as well as expected Madelung potential variations on the other hand, we find, play no role in the observed changes in electronic structure.

Appendix A

Monte Carlo Algorithm For Spin Models

8.1 Introduction And A Brief History

The name "Monte Carlo"was suggested by Nicholas Metropolis in reference to the famous casino in Monaco while proposing the use Monte Carlo method in physics in an early publication [1]. Monte Carlo simulations have important applications in solving problems in vast areas of computational science and engineering, with applications ranging from materials science to biology to quantum physics and statistical physics as well as architecture and economics. Monte Carlo methods are algorithms using random numbers (or rather, pseudo-random numbers) to solve computational problems.

In the 1920's, Karl Pearson used the random numbers for solving complex problems in probability theory and statistics which otherwise could not be solved exactly [2]. In the middle of the twentieth century, this technique was used to study neutron multiplication, scattering, propagation and eventual absorption or leakage in or from a medium. Stan Ulam, von Neumann and Enrico Fermi were the first to propose and employ the Monte Carlo method as a numerical technique for solving practical problems. One of the first uses of Monte Carlo simulations is described in the classic article by Nicholas C. Metropolis, Arianna W. Rosenbluth, Marshall N. Rosenbluth, Augusta H. Teller, and Edward Teller who described the algorithm named Metropolis along with its application to the equation of state of fluids [1].

Monte Carlo methods are particularly useful for problems that involve a large number of degrees of freedom. For example, consider a lattice which has N lattice sites and each lattice site can take two spin values, +1 or -1. So this system will have 2N spin configurations. When N takes a large value which is actually the case for a real system, then how we are going to sample our system. Here the Monte Carlo technique comes in. To make a better understanding of this technique, we will discuss it in the next coming sections.

8.2 Importance Sampling

For equilibrium process in statistical mechanics, the average value of any quantity A(x) with discrete degrees of freedom x_i is given as,

$$\langle A(x)\rangle = \frac{\sum_{i=1}^{m} e^{[-H(x_i)/k_BT]} A(x_i)}{\sum_{i=1}^{m} e^{[-H(x_i)/k_BT]}} \tag{8.1}$$

For a simple Ising like model, where the number of states we are dealing with are very large, one simply wants to work with a small subset of these states *i.e.* m$< 2^N$. For a simple one dimensional problem, the above summation can be evaluated over a regular grid. But when dealing with a higher dimensional problem, choice of a regular grid does not make much sense and so one should rather choose the points x_i at random. A uniform distribution of x_i points can be achieved by utilizing pseudo-random numbers using a random number generator. It is called the simple sampling Monte Carlo method.

The problem with simple sampling is that we might ignore the important region of the sample space and at the same time we might add a less important sample region to our system. So a more efficient technique is needed which samples the configuration $\{x_i\}$ in a completely random fashion, but preferably from the important regime of the phase space at temperature T while calculating the average $\langle A(x)\rangle$.

Suppose a process where the sample points x_i are selected with some probability $P(x_i)$, then Eq. 8.1 takes the form,

$$\langle A(x)\rangle = \frac{\sum_{i=1}^{m} e^{[-H(x_i)/k_BT]} A(x_i)/P(x_i)}{\sum_{i=1}^{m} e^{[-H(x_i)/k_BT]}/P(x_i)} \tag{8.2}$$

For a simple choice $P(x_i) \propto e^{[-H(x_i)/k_BT]}$, the above equation reduces to,

$$\langle A(x)\rangle = \frac{1}{m}\sum_{i=1}^{m} A(x_i) \tag{8.3}$$

This method of sampling is called importance sampling [3].

8.3 Metropolis Algorithm

It is an attempt to sample the phase space from the probability distribution P(x_i) by generating micro states belonging to a canonical ensemble.and was proposed by Nicholas Metropolis and his collaborators A. W. Rosenbluth, M. N. Rosenbluth, A. H. Teller and E. Teller [1]. Suppose we want to sample from an arbitrary discrete distribution f(i), where i can take discrete integer values between 1 and N called states and the set including all states is denoted by S = 1,2 ... N. Now the Metropolis sampling procedure can be implemented as follow. Consider x_i ($\in$ S) as the current state, then we select a trial state x_t randomly and with equal probability from amongst the N states of S. If the ratio $p = f(x_t)/f(x_i) \geq 1$, then we accept the the trial state and assign $x_{i+1} = x_t$. If $p < 1$, then generate a random number r, uniformly distributed in the range 0 to 1. If r $\leq p$, then only accept the trial state and set $x_{i+1} = x_t$, otherwise reject the trial state and set $x_{i+1} = x_i$ and proceed. A good initial choice x_0 is the state with the maximum probability.

8.4 Algorithm For The Ising Model

The Ising model Hamiltonian [4] in two dimensions is given by,

$$H = -J \sum_{\langle i,j \rangle} \vec{S_i} \cdot \vec{S_j} \tag{8.4}$$

where J is the exchange interaction between nearest neighbor site can be positive or negative representing ferromagnetic and antiferromagnetic configurations respectively. Spin S can take values +1 or -1. First step of the Monte Carlo algorithm with this model should be the initialization of lattice. It can be done using a two dimensional array in a FORTRAN program [5]. Here while assigning spin to the lattice points, one can start with many different magnetic configurations starting from a full antiferromagnetic checker board like spin arrangement to a ferromagnetic arrangement. One requires the lattice sites N to be even in order to assure the use of periodic boundary conditions. Periodic boundary conditions are the set of boundary conditions used to simulate the properties of an infinitely large system by approximating it to a replica of small system when repeated can generate the original system. For example, if we consider only the first nearest neighbors on a square lattice in the Ising model with total N×N

size system, then the first two rows/cols must start out the same as the last two *i.e.* i-1=N when i=1; i+1=1 when i=N; j-1=N when j=1; j+1=1 when j=N.

After completion of the above steps, we allow our system to evolve in time using Metropolis algorithm till equilibrium is achieved. Once the system is equilibrated, the excess energy added from the non-equilibrated part has to be removed from the system. We consider the Monte Carlo step size (mcs) as the number of configuration or states of our system. Within a single Monte Carlo step, as a part of importance sampling, using the transition probability we always flip only one spin of the lattice and one sweep through lattice will involve one flip of all the spins. So after one MC step we will have a new configuration.

The decision whether to flip a spin or not is taken by considering Metropolis algorithm in the program. Using the Ising Hamiltonian, if the calculated energy difference (ΔE) between the trial (flipped) and old configuration is less than of equal to zero, the trial state is energetically favorable and thus this move must be accepted. Otherwise, a random number $0 \leqslant \mathrm{r} \leqslant 1$ is generated and the new state is accepted only if $\exp(\beta\ \Delta\mathrm{E}) > \mathrm{r}$ where β is $\frac{1}{k_B T}$ at temperature T. After completion of this step, physical properties of the system can now be calculated. Large number of Monte Carlo steps should be considered specially near the transition temperature in order to obtain more accurate results.

8.5 Concept Of Spin Flipping In Heisenberg Model

The Heisenberg Hamiltonian is same as the Ising Hamiltonian except for the fact that now the spins can take all possible directions. An easy way to do this is by using spherical polar coordinates where one can get all random directions in space, varying θ, ϕ from 0 to π and 0 to 2π respectively with the help of random numbers. In this model, the flipping of spins is done in a different manner than Ising model. In this case, a randomly oriented trial spin is generated with the help of random numbers. The energy difference (ΔE) is then calculated by taking scalar product between the sum of the nearest neighbor spins and the original lattice spin as well as the trial spin. After this is done, the same procedure as discussed in the case of Ising model is followed and the physical properties of the system are calculated.

8.6 Calculation Of Physical Quantities

The magnetization for a particular configuration can be calculated as,

$$M = \sum_{i=1}^{N^2} S_i \quad \text{in the case of 2D Ising model and} \tag{8.5}$$

$$M = \sqrt{M_X^2 + M_Y^2 + M_Z^2} \quad \text{where} \quad M_{X/Y/Z} = \sum_{i=1}^{N} S_i^{X/Y/Z}$$

in the case of Heisenberg model (8.6)

This magnetization is then normalized over system size to get the magnetization per site m_i. The ensemble average of magnetization is then evaluated by taking the arithmetic average over many configurations (Monte Carlo steps) which can be written as,

$$\langle m \rangle = \frac{1}{mcs} \sum_{i}^{mcs} m_i \tag{8.7}$$

It should be noted here that the configurations considered in the above equation to calculate the magnetization are the ones obtained after the system was equilibrated. In the case an antiferromagnetic system, magnetization can not be evaluated in the above manner as it will give zero magnetization since there are equal number of opposite spins. In this case, one has to add the absolute value of spins at each site in any of the two sublattices formed by two different spins.

8.7 Finite Size Effects

While the real systems are infinitely large in size, it is computationally impossible to simulate the properties of such a system. With the help of suitable approximations and boundary conditions one can computationally work with finite lattice sizes but the effects of finiteness of the system could drastically affect properties of the system. In many cases, a decrease of the system size causes a smearing of phase transition. The convergence near the transition point becomes poor and this makes it hard to estimate the accurate value of transition temperature. To overcome

this problem, finite size scaling is required to estimate the properties of an infinite system from the results obtained on the finite system.

One published result using a Monte Carlo code written by me can be found in reference [6].

Bibliography

[1] N.C. Metropolis *etal*., J. Chem. Phys. **21**, 1087 (1953).

[2] L. H. C. Tippet, *Random Sampling Numbers*, Cambridge University Press (1927).

[3] D.P. Landau and K. Binder, *A Guide to Monte Carlo Simulations in Statistical Physics*, Cambridge Univ. Press (2000).

[4] Kurt Binder and Dieter Heermann, *Monte Carlo Simulation in Statistical Physics: An Introduction* (2010).

[5] Ernst Ising, *Contribution to the Theory of Ferromagnetism* (1924).

[6] S. Middey, Ashis Kumar Nandy, S. K. Pandey, Priya Mahadevan and D. D. Sarma, Phys. Rev. B **86**, 104406 (2012).